TECHNISCHE UNIVERSITÄT DRESDEN

Turn all the lights off: Separating Second Harmonic Generation signal contributions at lithium niobate domain walls

Master-Arbeit
zur Erlangung des Hochschulgrades
Master of Science
im Master-Studiengang Physik

vorgelegt von

Peter Andrew Hegarty
geboren am 25.08.1994 in Greenock, United Kingdom

Institut für Angewandte Physik (IAP)
TU Dresden
2022

Eingereicht am 11.01.2022

1. Gutachter: Prof. Dr. Lukas M. Eng
2. Gutachter: Prof. Dr. Mirco Imlau

Abstract

Second Harmonic Generation Microscopy (SHGM) has recently emerged as an excellent tool with which to investigate novel materials such as both topological and lower-dimensional systems, especially ferroelectric domain walls. However, when analysing the afore-mentioned domain walls, a number of observed phenomena with respects to the contrast between domain and domain walls can be explained with up to three possible mechanisms, these being Cherenkov-type phase-matching, phase-interference and tensor modification. In this thesis, we will implement and test a number of approaches with which we can separate signal contributions owed to each mechanism, with a particular emphasis on the so-called Cherenkov Second Harmonic Generation (CSHG). We show that multiple mechanisms coexist simultaneously and that (a) the use of an aperture; (b) making geometric changes to the experimental system or (c) exploiting a material's specific dispersive behaviour all prove to be valid methods capable of separating the signal caused by different mechanisms. In the future, this will allow for a separation of tensor-modified, CSHG and phase signal contributions and therefore enable us to make more detailed observations and interpretations regarding the substructure of ferroelectric domain walls analysed using SHGM.

Kurzfassung

Second Harmonic Generation Mikroskopie (SHGM) zeichnete sich zuletzt als herausragendes Werkzeug für die Untersuchung neuartiger Materialen ab. Hierzu zählen sowohl topologische als auch niedrig-dimensionale Systeme, dabei insbesondere ferroelektrische Domänenwände. Jedoch zeigt sich die genaue Interpretation von beobachteten Phänomenen bezüglich des Kontrastes zwischen Domänenwand und umliegender Domäne als schwierig. Demzugrunde liegt die Existenz von drei Mechanismen, anhand derer man die Interpretation führen kann, diese wären Phasenanpassung des Cherenkov-Typs, Phaseninterferenz und Tensormodulierung. In der vorliegenden Arbeit erproben wir mehrere Ansätze mit denen wir die einzelnen Signalbestandteile, die jeweils von einem der Mechanismen stammen, voneinander zu trennen, mit besonderem Augenmerk auf Cherenkov Second Harmonic Generation (CSHG). Wir zeigen, dass mehrere Mechanismen gleichzeitig auftreten können und sich in (a) der Hinzunahme einer Apertur; (b) geometrischen Änderungen des Systems oder (c) Ausnutzung der materialspezifischen Dispersionsverhaltens eine Reihe von nützlichen Methoden herausstellt, um die jeweiligen Signalbeiträge voneinander zu trennen. In Zukunft erlaubt uns dies die Trennung von tensor-moduliertem, CSHG- und Phasensignal und demzufolge genauere Aussagen und Interpretationen bezüglich der Substruktur von ferroelektrischen Domänenwänden, die mittels SHGM untersucht werden.

Contents

1 Introduction **1**

2 Theoretical basics **5**

2.1 The non-linear optical polarisation of media 5

2.2 The non-linear susceptibility tensor $\chi^{(n)}$ 7

2.3 Phase-matching and emission efficiency 9

2.3.1 Collinear and non-collinear phase-matching 11

2.4 Second Harmonic Generation using focused Gaussian beams 11

2.5 Ferroelectric domain walls - why are they visible in SHGM? 13

2.5.1 Changes in the nonlinear susceptibility 16

2.5.2 Defect-assisted phase-matching and Cherenkov SHG (CSHG) 18

2.5.3 Phase interference and superposition 21

3 Selective blocking of Cherenkov Second Harmonic Generation **27**

3.1 Geometric blocking 27

3.2 Dispersion switching via wavelength tuning 30

4 Methods and procedures **33**

4.1 Lithium niobate (LN) 33

4.2 Data generation 35

4.2.1 Set-up - the LightScanningMicroscope980 35

4.2.2 Sample preparation and scanning geometry 35

4.2.3 Read-out process 37

4.3 Data processing 40

4.3.1 Normalisation 40

4.3.2 Fit process 44

5 Geometric blocking **47**

5.1 Emission characteristics 49

5.2 Domain walls at the surface 57

5.3 Blocking via aperture 63

5.3.1 Aperture SHG with a z-polarised fundamental 68

5.3.2 Aperture SHG with an x-polarised fundamental 69

5.3.3 Determining the cone angle 73

6 Dispersion switching **79**

6.0.1 Processes involved in anormal dispersion 79

6.1 Congruent lithium niobate analyzed in the Y(X;_)Y-geometry 80

6.2 Y(Z;_)Y - a false geometry 88

6.3 Congruent lithium niobate - the magic crystal 92

6.3.1 Theoretical calculations 92

6.3.2 Images for MgO:LN 93

6.3.3 Dispersion effects in back reflection 96

7 Contrast analysis and impact of CSHG **101**

7.1 Contrast Analysis 101

7.1.1 Attempting to quantify the strength of CSHG 107

8 Conclusion and outlook **113**

Bibliography **117**

1 Introduction

Over the past years there has been an increased interested in both lower-dimensional and topologic systems as a means to both better understand the fundamental laws of our world as well as further miniaturise electronic devices [1][2][3]. Examples of such lower-dimensional systems include Van-der-Waals (vdW) and other 2-dimensional (2D) materials as well as recently, ferroelectric domain walls (DWs). In particular, DWs represent the interface between domains of different polarisation within a ferroelectric crystal. One method commonly used to investigate DWs is so-called Second Harmonic Generation Microscopy (SHGM), during which the investigated sample is illuminated by a laser beam and said sample generates light at twice the frequency of the incident electromagnetic wave through non-linear interactions.
In recent years, SHGM on ferroelectric domain walls has found a number of interesting applications, supported by the low requirements on sample preparation and the scale of samples that can be investigated using the method. These include 3-dimensional (3D) profiling of domain walls [4][5], as well as real-time observations [6][7]. Furthermore, SHGM finds use in determining both symmetry properties and possible substructures within the crystal and at the domain wall [8][9]. Additionally, SHGM has found use in measuring both the layer number and orientation of vdW and 2D thin-film flakes [10][11]. The former is possible due to the increased signal generation from an even number of layers while polarimetry is performed to locate the direction of maximum signal which coincides with the flakes' crystal axis. In the present work, we shall be focusing on the use of SHGM in the investigation of ferroelectric domain walls.
As mentioned prior, SHGM has found use in determining both symmetry and polar properties of domain walls as reported by Cherifi-Hertel at al. [9], which functions exceptionally well and currently stands as the sole method capable of this characterisation at a larger scale. They found that DWs seemed to possess their own substructure as well as display topologic qualities [12]. Their results were based on the signal strength and polarisation generated at the domain walls compared to the surrounding domain area. The presented explanation of their observations was based on the domain wall representing a local change to the local properties of the ferroelectric crystal caused by a (polar) substructure. However, when attempting to explain the phenomena in SHGM at domain walls, i.e. rotation or change of magnitude in signal, other groups have shown that there are more possible explanations than simply a change to the local properties. As two examples, both Kämpfe et al. [4] and Spychala et al. [13] have

presented separate findings that lead to the availability of three possible mechanisms which define the behaviour of domain walls under SHGM. These mechanisms are:

- 1) Local changes in the non-linear properties: The DWs themselves are assumed to change the local non-linear properties, f.e. via charge accumulation or other substructure. First works include Flörsheimer et al. [14] and current work has been published by Cherifi-Hertel et al. [12].

- 2) Cherenkov Second Harmonic Generation (CSHG): The DWs can function as a source of defect wave-vectors, assisting in the phase-matching process and leading to an incresed signal generation. First works on the topic include Zembrod et al. [15], recent work has been published by Kämpfe et al. [4] and Kirbus et al. [5].

- 3) Phase-interference and superposition: Depending on the domain polarisation, second harmonic waves emitted from different domains may have an intrinsic phase shift to each other which results in interference effects in the far-field. It is important to note that the domain walls themselves are small compared to the lateral size of the microscope focus, thereby becoming unable to be fully resolved. First mentions include Uesu et al. [16], current work has been published by Spychala et al. [13].

The issue then becomes identifying which mechanism(s) dominate or are present in the signal.

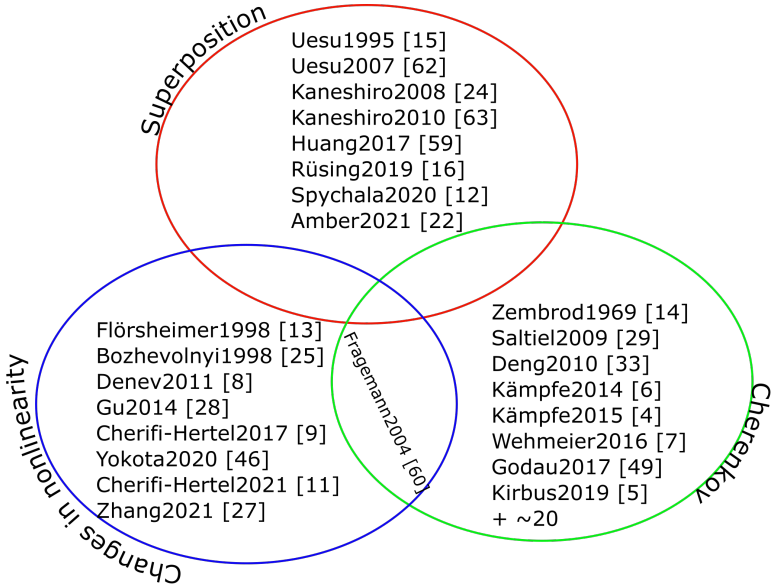

Figure 1.1: Venn-Diagram summarising the results of a literature census on publications presenting SHGM performed on ferroelectric crystals and domain walls. Each research group seemed to have selected one mechanism they find to be the likeliest cause of the observed phenomena, with relatively few groups investigating possible combinations.

Based on a short literature census (example results are presented in Fig. 1.1), we found that there are a number of published works centred around each of the aforementioned mechanisms. However each group used a single chosen mechanism with which to explain their observations in SHGM, initially neglecting to include the possibility of co-existence of more than one process. Recently, there have been a number of papers in which the authors demonstrate that observations one group may ascribe to one mechanism can be equally well explained using a second mechanism [13]. It therefore seems reasonable to assume that all three mechanisms co-exist and play a role in SHGM at the same time. Efforts were made to isolate both local changes to the non-linearity by Cherifi-Hertel et al. [12], as well as phase-effects by Spychala et al. [13]. However, we found few publications attempting to differentiate the CSHG mechanism from the others. As CSHG finds a wide array of uses in especially 3D-imaging of ferroelectric domain structures [5][7], it is increasingly important that similar efforts be made to understand the workings behind the mechanism and how it compares to the others. Therefore, this master thesis will attempt to take first steps towards being able to differentiate CSHG from other signal contributions. To this end, we will orientate ourselves by two guiding questions with associated subquestions:

- *How strong is the Cherenkov mechanism?*: For both changes to the non-linearity as well as phase effects it is possible to simulate and at least approximately predict the relative signal generated at the domain wall compared to the surrounding region. To date, no such predictions have been made for CSHG and we would therefore desire to obtain an initial estimate on the comparative strength based on our performed experiments.

- *Can CSHG contributions be isolated or discarded?*: In the event that a prediction of the strength of CSHG proves unlikely, a further step would be investigating whether the respective signal contributions can be isolated in the detected signal. A secondary approach would be to attempt to remove, or block, the CSHG contributions from the detected signal. We would therefore ask: *How well can we differentiate experimentally between each mechanism's contribution? Is there a specific measurement geometry which makes this easier or more difficult?*

The goal of this work will be to either answer the questions above, or at least take initial steps towards an answer. This will be done by using a commonly investigated material in lithium niobate ($LiNbO_3$, LN) to study whether it is possible to single out or remove CSHG from the detected signal. Furthermore, LN has previously been used in works involving CSHG, such as those by Kämpfe et al. [6], however most often by using crystals in z-cut geometry. To the current extent of our knowledge, the present work would be the first to show the existence of and investigate CSHG in a y-cut geometry. This is noteworthy due to the increased use of x- and y-cut lithium niobate when fabricating thin-film systems. [17][18]

Chapter 2 will begin with an introduction into the non-linear interactions of light and matter, with a strong focus on Second Harmonic Generation (SHG). In chapter 3, a number of physical criteria will be hypothesised upon which it should be possible to isolate the CSHG signal contributions. Chapter 4 will give a brief overview on the experimental set-up and the methods used to generate the evaluated data. Chapters 5 and 6 then present the results of our experiments performed in accordance with the criteria developed in chapter 3, while in chapter 7 a first attempt will be made to quantify certain properties of CSHG as well as draw a comparison to other mechanisms. Finally, chapter 8 will give a short summary and outlook as well as provide a few experimental proposals for further work on the topic.

2 Theoretical basics

2.1 The non-linear optical polarisation of media

On a fundamental level, the behaviour of a system exposed to an electromagnetic field, a light beam for example, is fully described by the Maxwell equations which lay the foundation for the field of electrodynamics. However, often it is practical to have an approximation that considers Maxwell's equations while allowing for a simpler approach to a given problem. For most media, this can be simplified by examining the polarisation of a medium in response to the applied electric field, as is governed by the susceptibility of the medium.
A first approach uses the assumption of a linear reaction of a medium to an incident electric field. The polarisation $\vec{P}$ of a medium is then given by:

$$\vec{P}(\vec{r},t) = \epsilon_0 \chi \vec{E}_{inc}(\vec{r},t). \tag{2.1}$$

Here, ϵ_0, $\chi = \chi^{(1)}$ and $\vec{E}_{inc}(\vec{r},t)$ are the free space permittivity, the material's susceptibility and the incident electric field, respectively. For sufficiently low fields or light intensities, this linear approach to a material's response is valid when used to describe effects such as reflection, transmission and absorption. In the case of birefringent materials, that is materials that possess a different refractive index based on the orientation within the crystal, these descriptions may also include a tensor-like description of the susceptibility.
In essence, this approach is similar to the harmonic oscillator, which represents a system in which the acting force scales linearly with the displacement of the mass from its rest position. As an example, one could look at the displacement of a pendulum consisting of a mass that is hung up by a cable or rope of a given length. For small displacements around the rest position, which is with the mass vertically below the point it is attached to, the restoring force scales linearly with the angular displacement ϕ. However, for stronger displacements, the restoring force can no longer be modelled as linearly scaling with ϕ, leading to an anharmonic oscillator behaviour. This transition from harmonic to anharmonic, or from a linear to non-linear scaling of the restoring force, will generally be observable for higher oscillation amplitudes, and therefore stronger excitations.
With the development of the LASER in the 1960's, it suddenly became possible to investigate the response to considerably higher fields, leading to *non*-linear optic responses to illumination by such a beam. To describe this effect the polarisation is expanded in a series of powers of the

incident electric field $\vec{E}_{inc}$, with $\chi^{(n)}$ as the n-th order susceptibility (-tensor) of the material:

$$\begin{aligned}\vec{P}(\vec{r},t) &= \epsilon_0[\chi^{(1)}\vec{E}(\vec{r},t) + \chi^{(2)}\vec{E}^2(\vec{r},t) + \chi^{(3)}\vec{E}^3(\vec{r},t) + ...] \\ &= \vec{P}_{linear} + \vec{P}_{NLO}\end{aligned} \tag{2.2}$$

The total polarisation of the medium is therefore viewed as the sum of the linear polarisation $\vec{P}_{linear}$ described by Eq. 2.1 and the non-linear polarisation $\vec{P}_{NLO}$ caused by higher powers of the electric field. The, possibly time-dependant, polarisation acts as a source of an electric field, leading to the wave equation for nonlinear optical media with the field and polarisation listed as scalars:

$$\Delta E - \frac{1}{c^2}\frac{\partial^2 E}{\partial t^2} = \frac{1}{\epsilon_0 c}\frac{\partial^2 P_{NLO}}{\partial t^2}. \tag{2.3}$$

As this work mostly concerns second harmonic generation microscopy, which is itself a so-called second-order process (in other words the polarisation scales quadratically with the incoming field), we will limit ourselves to the quadratic susceptibility $\chi^{(2)}$. The nature of the non-linear contribution can be visualised by looking at the second order mixing of two incident light fields. Assuming a plane wave $[E(t) = E_0 \cdot e^{-i\omega t} + c.c]$ for each field with field strengths E_1 and E_2 and frequencies ω_1 and ω_2, respectively, we have:

$$\begin{aligned}P^{(2)} =& \epsilon_0\chi^{(2)}[2E_1E_1^* + 2E_2E_2^* \\ &+ (E_1^2e^{-i2\omega_1 t} + E_2^2e^{-i2\omega_2 t} + 2E_1E_2e^{-i(\omega_1+\omega_2)t} + 2E_1E_2^*e^{-i(\omega_1-\omega_2)t} + c.c.)].\end{aligned} \tag{2.4}$$

Looking at equation 2.4, we can see that there are a total of five different frequencies and 6 separate terms generated from this two-field mixing:

- $\omega = 0$: Visible in the first two terms, these describe the process of *optical rectification (OR)*, the generation of a static electric field within the medium.
- $\omega = 2\omega_1$;
- $\omega = 2\omega_2$: The third and fourth terms show plane wave behaviour at twice the frequency of the single incident waves, called *Second Harmonic Generation (SHG)*.
- $\omega = \omega_1 + \omega_2$: The frequencies combine constructively in a process called *Sum-Frequency-Generation (SFG)* in the fifth term.
- $\omega = \omega_1 - \omega_2$: The sixth term describes a process wherein the two frequencies combine destructively. Analogous to SFG, this process is called *Difference-Frequency-Generation (DFG)*.

As an example of their scientific value, both SFG and DFG are processes commonly used in Optical Parametric Amplifiers (OPAs). These devices are used to generate new frequencies from the beam of an input laser, most commonly in the near-infrared spectral region, as a small portion of the input is split off to generate a second beam with which the original signal can interact and the frequencies of the two can either add or subtract to a new frequency. This allows access to wavelength ranges that are otherwise inaccessible with a single laser, allowing for a broad tunibility of the output laser beam. In these cases, SFG is used to convert the input beam to a higher wavelength regime, towards the UV spectrum, while DFG can allow the user to obtain an output further into the IR or even THz spectrum, which have a lower frequency than that of a commonly used titanium-doped sapphire (Ti:Sa) laser that usually operates around 800 nm.
Looking again at Eq. 2.4, if we set $\omega_1 = \omega_2$, we can see that both the Sum Frequency and Difference Frequency terms become additional terms for Second Harmonic Generation or Optical Rectification, respectively.

2.2 The non-linear susceptibility tensor $\chi^{(n)}$

Returning to eq. 2.2, it is now useful to investigate the properties of a materials optical non-linear response described by $\chi^{(n)}$. In general, the n-th order susceptibility will be a tensor of rank $n + 1$, that is to say a second order non-linear susceptibility tensor $\chi^{(2)}$ is a 3rd-rank tensor of shape (3x3x3) and therefore has up to 27 independent elements. Similarly, a 3rd order non-linear susceptibility tensor is of rank 4 with 81 entries, but not all of which will be independent due to symmetry reasons. In a three-wave mixing process involving the frequencies ω_1, ω_2 and $\omega_3 = \omega_1 + \omega_2$, the resultant polarisation is calculated as :

$$P_i^{(2)}(\omega_3) = \epsilon_0 \sum_{jk} \sum_{(1;2)} \chi_{ijk}^{(2)}(\omega_3; \omega_1, \omega_2) E_j(\omega_1) E_k(\omega_2). \tag{2.5}$$

By further limiting our interest in the above equation to the case of Second Harmonic Generation, we come to:

$$P_i^{(2)}(2\omega_f) = \epsilon_0 \sum_{jk} \chi_{ijk}^{(2)} E_j(\omega_f) E_k(\omega_f), \tag{2.6}$$

with ω_f the frequency of the incident fundamental field. As it stands, this is a simplified form of Eq. 2.5, however, we still lack any further information on the properties of the nonlinear susceptibility tensor $\chi_{ijk}^{(2)}$. We can now use the physical electric field to identify two limitations on the tensor without requiring knowledge of our sample system:

1. As the electric field is described by a vector, the order in which we apply fields in the

calculation will not have an effect on the result. In other words, as $E_j E_k = E_k E_j$ we can freely permute the last two indices of the tensor.

2. Both electric fields and generated polarisations are physically observable quantities, which means that they must themselves be purely real, such that positive and negative frequency contributions are related by complex conjugation.

As a result, we have the following implications:

$$\begin{aligned} \chi^{(2)}_{ijk} &= \chi^{(2)}_{ikj} \\ \chi^{(2)}_{ijk}(-2\omega_f;,-\omega_f) &= \chi^{(2)*}_{ijk}(2\omega_f;\omega_f). \end{aligned} \tag{2.7}$$

When working with the nonlinear susceptibility tensor, it is common to introduce a contracted notation using the tensor:

$$d_{ijk} = \frac{1}{2}\chi^{(2)}_{ijk}, \tag{2.8}$$

such that

$$P_i(2\omega_f) = \epsilon \sum_{jk} 2 d_{ijk} E_j(\omega_f) E_k(\omega_f). \tag{2.9}$$

This d-tensor can be further reduced for use in f.e. SHG, as it is symmetric in its last two indices, which can be taken together to form the matrix $d_{ij'}$ using $jk \to j'$:

$11 \to 1$; $22 \to 2$; $33 \to 3$;
$23, 32 \to 4$; $13, 31 \to 5$; $12, 21 \to 6$.

The use of the $d_{ij'}$ allows us to rewrite the equation for the induced polarisation using the full form of $d_{ij'}$ as:

$$\begin{pmatrix} P_x(2\omega_f) \\ P_y(2\omega_f) \\ P_z(2\omega_f) \end{pmatrix} = \begin{bmatrix} d_{11} & d_{12} & d_{13} & d_{14} & d_{15} & d_{16} \\ d_{21} & d_{22} & d_{23} & d_{24} & d_{25} & d_{26} \\ d_{31} & d_{32} & d_{33} & d_{34} & d_{35} & d_{36} \end{bmatrix} \begin{pmatrix} E_x^2(\omega_f) \\ E_y^2(\omega_f) \\ E_z^2(\omega_f) \\ 2E_y(\omega_f)E_z(\omega_f) \\ 2E_x(\omega_f)E_z(\omega_f) \\ 2E_x(\omega_f)E_y(\omega_f) \end{pmatrix}. \tag{2.10}$$

From here, we can proceed to use allowed symmetry operations dictated by the crystal to be investigated in order to reduce the number of independent entries in $d_{ij'}$. It is important to note, that only non-centrosymmetric crystals exhibit second-order nonlinearities [1] as can

[1] While it is true that centrosymmetric materials such as metals do not possess even-order non-linear susceptibilities, it has been shown that such materials can still exhibit SHG. [19][20] However, the SHG process is confined to the surface of the material as the inversion symmetry is broken at the medium-environment interface. Any other interface also represents such a localised symmetry-breaking and allows for SHG at said interface.

be verified by looking at the polarisation induced by two fields of opposite sign, assuming inversion symmetry:

$$\begin{aligned} P = \epsilon_0 \chi^{(2)} E^2 = \epsilon_0 \chi^{(2)} (-E)^2 = -P \\ \Rightarrow \chi^{(2)} = 0. \end{aligned} \tag{2.11}$$

As an example of such a non-centrosymmetric crystal, we will look at the example of lithium-niobate ($LiNbO_3$, LNO), which will be used as the basis for further investigations in this work. LNO is part of the crystallographic class $3m$ with its corresponding tensor stated as:

$$d_{ij'} = \begin{bmatrix} 0 & 0 & 0 & 0 & d_{31} & -d_{22} \\ -d_{22} & d_{22} & 0 & d_{31} & 0 & 0 \\ d_{31} & d_{31} & d_{33} & 0 & 0 & 0 \end{bmatrix} \tag{2.12}$$

An initial estimate for the magnitude of the tensor elements can be found either in the textbook by Boyd et al. [21] or in work performed by Armstrong et al. [22]. The magnitude of the non-linear susceptibility is then estimated to be comparable to the inverse of the characteristic atomic electric field, which is approximately $1 \times 10^{-11}\,\mathrm{V/m}$. The estimation is therefore that $\chi^{(2)} \approx 1 \times 10^{-12}\,\mathrm{m/V}$.
As can be seen in Eq. 2.12, LNO needs the three independent entries $d_{22} = 3\,\frac{\mathrm{pm}}{\mathrm{V}}$, $d_{31} = 6\,\frac{\mathrm{pm}}{\mathrm{V}}$ and $d_{33} = 36\,\frac{\mathrm{pm}}{\mathrm{V}}$, which can be assumed to be approximately constant across the investigated wavelength range of 850 nm to 1110 nm.

2.3 Phase-matching and emission efficiency

When performing experiments using nonlinear methods, it is of specific interest to have at least a rough estimate for the intensity of the emitted second harmonic wave. A detailed derivation of the following section can be found in both [21] and [22]. Here, only the results of said works will be summarised.

During SHG process, the transfer of energy from the fundamental beam to the second harmonic depends heavily on the wave-vector mismatch

$$\Delta\vec{k} = 2\vec{k_1} - \vec{k_2}. \tag{2.13}$$

For an ideally phase-matched process ($\Delta\vec{k} = 0$), the field of the second harmonic will increase linearly with the propagation distance through the crystal, with the intensity therefore increasing quadratically with distance. As $k(\omega) = 2\pi n(\omega)/\lambda(\omega)$, this would require that the crystal possesses the same refractive index for both the fundamental and second harmonic

wavelength, which is generally not given. Most crystals show so-called normal dispersion, in that the refractive index is an increasing function of frequency.

For a non-phase-matched process, the energy initially converted to the second harmonic wave will start to transfer back into the fundamental wave with increasing propagation distance, causing an oscillation of energy between both waves. Said oscillation in the intensity of the second harmonic can be described by the following, assuming the front crystal surface is located at $z = 0$:

$$I_{2\omega} = \frac{16d^2\omega I_f^2}{n_\omega^2 n_{2\omega}\epsilon_0 c^2} z^2 \left(\frac{sin(1/2z\Delta k)}{1/2z\Delta k}\right)^2. \tag{2.14}$$

Often, one uses the coherent interaction length [23] $L_{coh} = 2/\Delta k$ to model the intensity over propagation distance.

Perfect phase-matching becomes possible in birefringent crystals such as LNO, which allows for an appropriate mismatch Δk dependent on the angle between both the incident beams and the crystal's optical axis, as well as interaction with the correct tensor elements. A therefore common method to improve SH efficiency is angle-tuning, whereby the angle between the incident beam and sample is changed to allow for perfect phase-matching of the desired wavelength.

A second method commonly used in non-linear frequency converters is so-called Quasi-Phase-Matching (QPM). Here the local susceptibility of the medium is periodically reversed with a periodicity unique to the combination of medium and wavelength. What this achieves is that after propagating a distance of L_{coh} into the material, when the phase of both fundamental and second harmonic begin to drift apart, the phase-relation between the two is suddenly reset, leading to an increase in the overall signal, yet still less than for perfect phase matching. The behaviour of a perfectly phase-matched, quasi-phase-matched and phase-mismatched SHG process is shown in Fig. 2.1, taken from Boyd et al.[21].

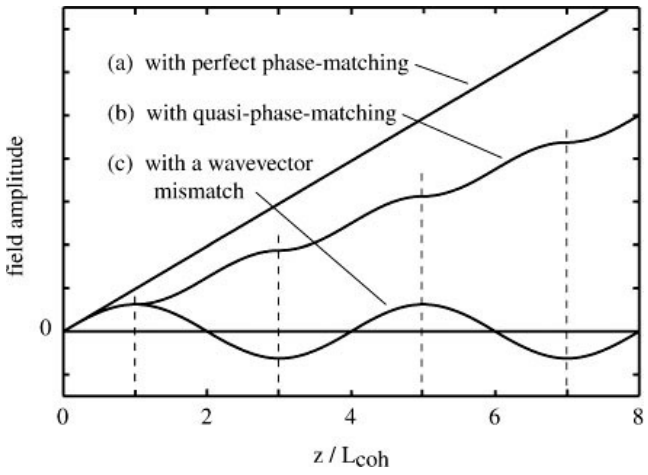

Figure 2.1: Second harmonic field over propagation distance for a (a) phase-matched, (b) quasi-phase-matched, and (c) phase-mismatched processes. Taken from [21]

2.3.1 Collinear and non-collinear phase-matching

Usually, the beams involved in phase-matched SHG are themselves collinear, however, due to the birefringence of some materials and a high degree of focusing, it becomes possible to have non-collinear phase-matching. This is due to the angular spread of wave vectors caused by focusing the incident beam through an objective with larger numerical aperture (NA). The higher the numerical aperture, the wider the k-vector spread Δk of the focused beams. Fig. 2.2 schematically shows the corresponding wave vector diagrams for an assumed case of the maximum angular spread of an objective. Due to their angle with respect to the optical axis, the absolute values of the wave vectors may not fulfil the phase-matching condition, as $2k_1 - k_2 \neq 0$, however $2\vec{k_1} - \vec{k_2} = 0$, which will allow for efficient SHG.

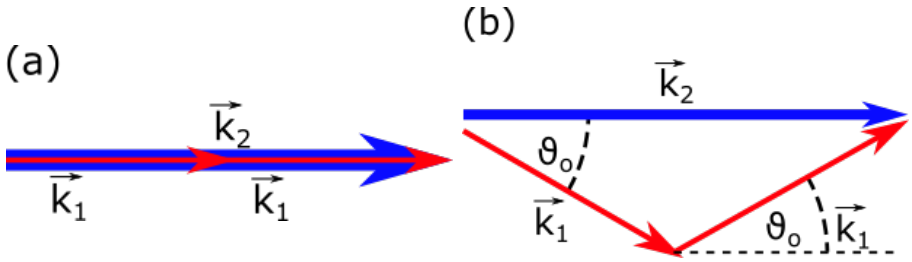

Figure 2.2: Vector diagram showing (a) collinear and (b) non-collinear phase-matching enabled by the angular spread of a beam focused by a high-NA objective. Note that $NA = sin(\theta_O) \cdot n(heren = 1)$.

2.4 Second Harmonic Generation using focused Gaussian beams

Considerations made up until this point have viewed the incident electric field as a plane wave with regards entering perpendicular into the material. During Second Harmonic Generation Microscopy, however, the beam is focused using a microscope objective in order to achieve sufficiently high energy densities for the generation of a measurable higher order signal. We therefore must consider the effect this focusing will have on the generated second harmonic light.

As with the previous section, a detailed derivation of this subject can be found in [21], and additional investigations into the subject in [24].

As shown in [21], the amplitude A_m of the m-th harmonic generated by an incident Gaussian beam can be expressed as:

$$A_m(z) = \frac{im\omega}{2nc}\chi^{(m)}A_f^m J_m(\Delta k, z_0, z) \quad \text{with } J_m(\Delta k, z_0, z) = \int_{z_0}^{z} \frac{e^{i\Delta k z'}dz'}{(1+2iz'/b)^{m-1}}. \tag{2.15}$$

In Eq. 2.15, n is the refractive index of the illuminated medium, c the speed of light in vacuum, A_f the amplitude of the fundamental wave, $J_m(\Delta k m z_0, z)$ the m-th order Bessel function and b the confocal parameter of the incident gaussian beam. The above integral can be evaluated analytically for two seperate cases, wherein either $b >> |z_0|, |z|$, which leads to the plane-wave limit as presented in the previous sections, or the opposite case of a tight focus within the crystal. For the latter situation, $b << |z_0|, |z|, z_0 = -|z_0|$ and $z = |z|$. Evaluation of the integral in 2.15 using contour integration results in:

$$J_m(\Delta k, z_0, z) = \begin{cases} 0, & \Delta k \leq 0, \\ \frac{b}{2}\frac{2\pi}{(m-2)!}(\frac{b\Delta k}{2})^{m-2}e^{-\frac{b\Delta k}{2}}, & \Delta k > 0. \end{cases} \tag{2.16}$$

Similar results have been calculated by [25]. 2.3 shows the behaviour for generation of the second, third and fourth harmonic, i.e. $m = 2, 3, 4$.

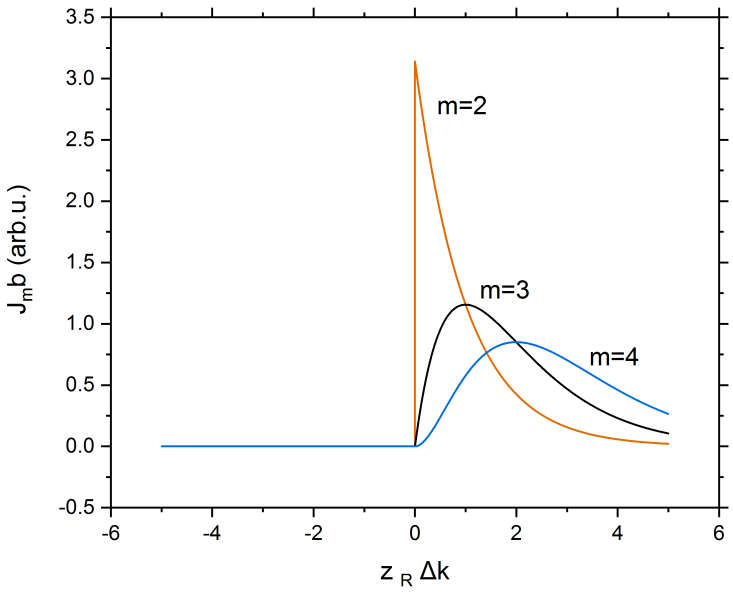

Figure 2.3: Calculated SHG efficiency for a varying wave number mismatch for second, third and fourth harmonic generation in a collinear phase-matching process. Basis for these calculations is Eq. 2.16

We can see that the efficiency of SHG vanishes for a negative wave vector mismatch just as it does for a perfect phase-match. The cause of this disappearance is the so-called Gouy phase shift, also termed as the phase anomaly. It describes the effect wherein a beam of light experiences a phase shift of π when passing through the focus. This hinders the coupling of the non-linear polarisation to the generated second harmonic beam, which can be counteracted by a positive wave vector mismatch. In the absence of said positive mismatch, when focusing

into the crystal bulk, the crystal will deliver no signal due to the destructive interference of the π-phase-shifted beam, allowing only SHG generated at the crystal's surface to be detected.

In order to visualize the effect of the Guoy phase shift, fig. 2.4 shows a line scan we have performed perpendicular to the surface of a KTP crystal with the initial position located outside of the crystal. As the focus closes in on the surface, a noticeable increase in signal is detected up to a maximum, that can be assumed as the surface position, after which the detected signal drops off to a similar level as prior to entering the crystal.

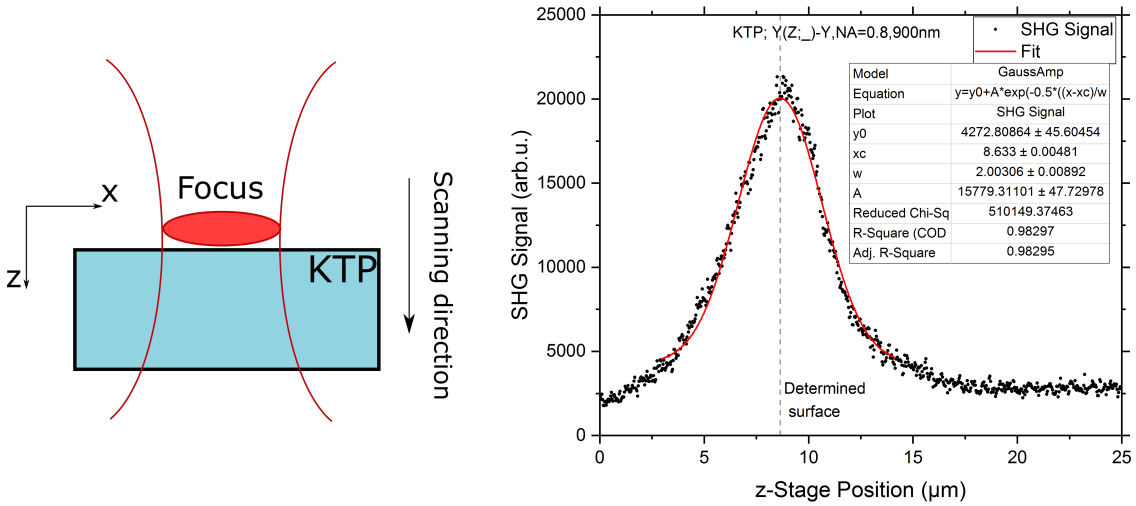

Figure 2.4: Line scan performed perpendicular to the z-face of a KTP crystal. The initial position was set outside the crystal in order to scan through the surface into the bulk material.The effect of the Guoy phase shift is readily visible in the decrease of the SHG intensity beyond the stage position which places the centre of the focus on the crystal surface.

2.5 Ferroelectric domain walls - why are they visible in SHGM?

As mentioned in the introduction to this work, ferroelectrics have long been a source of fascination for the scientific community. Recently, domain walls (DWs) in ferroelectric crystals have shown a number of new physical properties otherwise not seen in ferroelectric crystals, such as conductivity and topology. In order to better investigate these properties, it is important to be able to image and analyze said DWs using a variety of methods. [23][6][5]
When DWs are examined using Second Harmonic Generation Microscopy (SHGM), they become visible in a number of ferroelectric crystals. Their contrast to the surrounding domain can vary, however, not only between crystals but also within a single sample, as is observable

in Fig. 2.5 where the same DW structure was imaged using differently polarised light, leading to either a positive (bright) or negative (dark) contrast.

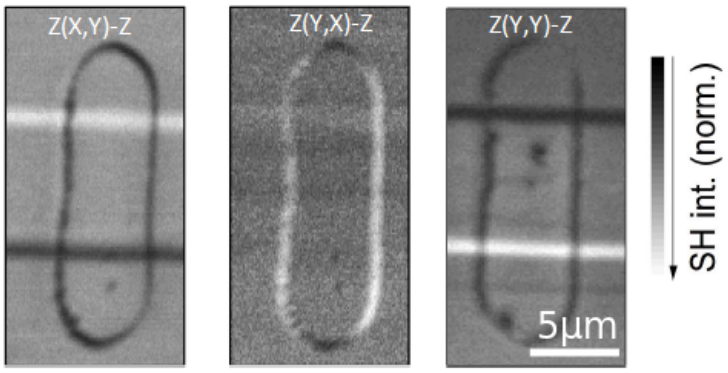

Figure 2.5: DW structure in LN over an embedded waveguide, investigated using a polarizer and analyzer. Depending on their relative orientation, different features of the structure appear either dark or bright in the scan image [Courtesy of Dr. M. Rüsing, private communication].

In order to fully employ SHGM as a tool for investigating ferroelectric domain structures, it therefore becomes necessary to fully understand the mechanisms which cause the detected contrast.
As mentioned in the introduction to this work, there are a total of three possible mechanisms involved in the SHGM process that may affect the detected contrast (see Fig. 2.6). These mechanisms being:

- ***Changes in the nonlinear susceptibility***: Domain walls are assumed to change the nonlinear properties of the crystal in their surrounding region, either by introducing a substructure into the crystal [9] or causing a change to the polarisation or polarisibility through a local static electric field or mechanical strain. The resultant change can be observable as either an increase or decrease of the detected contrast, dependent on the change in $\chi^{(2)}$.

- ***Phase-matching considerations***: In a process termed Cherenkov Second Harmonic Generation (CSHG), the domain wall assists in (non-)collinear phase-matching [6][4], allowing for a more efficient SHG at the wall itself. This causes a stronger positive contrast only.

- ***Phase and superposition effects***: The nonlinear susceptibilities of two oppositely polarised domains are inverted with respect to each other, causing a phase difference of π in generated second harmonic fields. These fields overlap during detection in the far-field which at first can be detected as a negative contrast, however, positive contrasts are also possible, depending on the specific material and experiment.

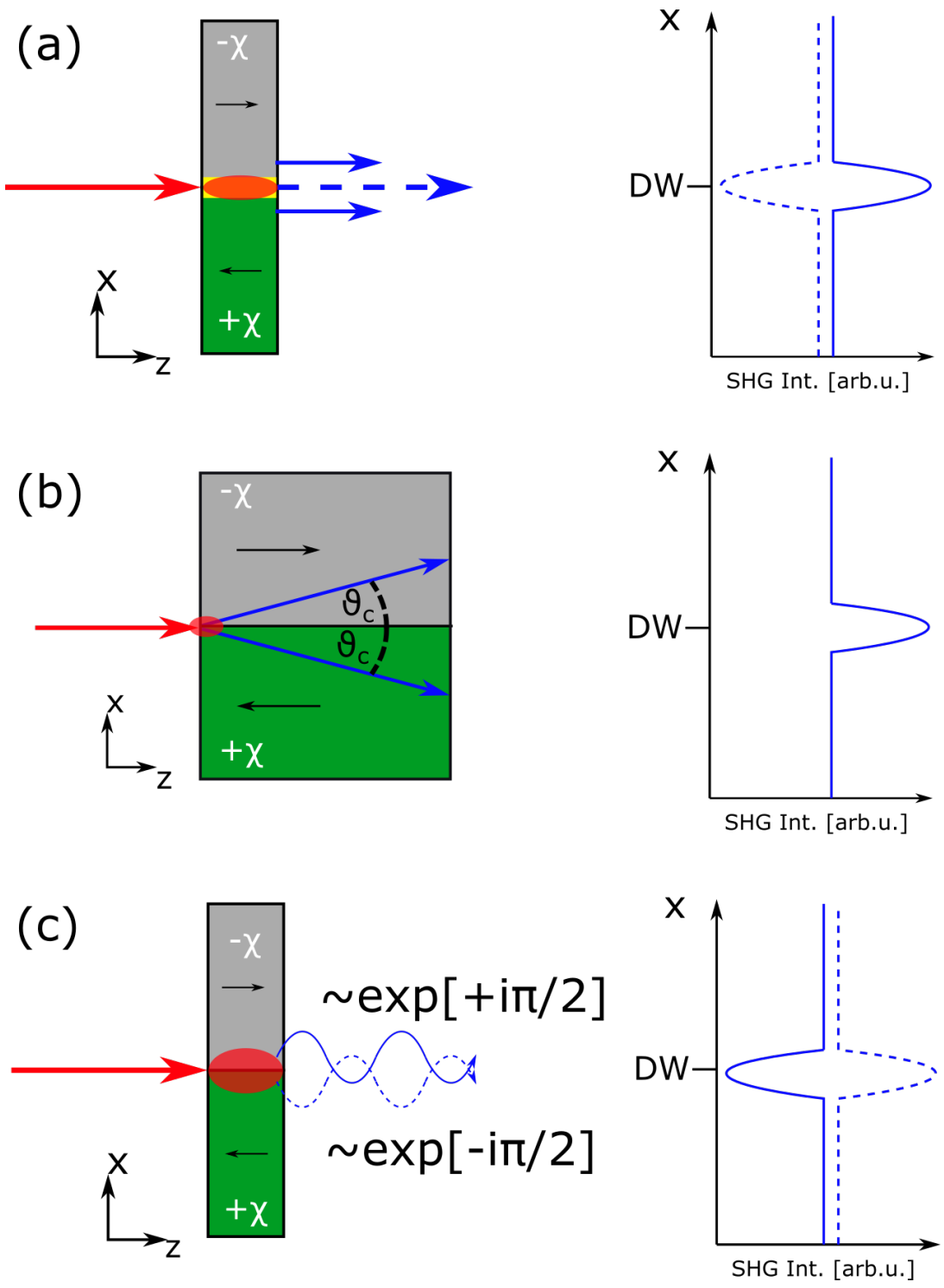

Figure 2.6: Schematic sketches of the three possible underlying mechanisms illustrated for domain walls in z-cut crystal: (a) changes to the non-linear tensor; (b) phase-matching effects; (c) phase interference and superposition effects. The plots sketched out for each mechanism illustrate the measured SHG signal when scanning the focus across the domain wall. Depending on the mechanism used as the basis for explanation, the detected signal at the domain wall can be higher than the surrounding domains for all three mechanisms. However, a drop in signal strength is only observable under certain conditions for changes in the local non-linearity as well as phase effects. For each mechanism, the solid line represents the most common effect on the local SHG signal.

The issue here thus is that all three mechanisms occur at different steps of the SHG process and whenever insufficient effort is made to selectively eliminate one or more of them, it becomes difficult to properly ascribe a measured effect to its root cause. As mentioned in the introduction to this work, most groups have committed themselves to understanding a single one of the above effects and seek to fully understand it. The following chapter will give a brief introduction to the proposed mechanisms along with examples of published works concerning each of them.

2.5.1 Changes in the nonlinear susceptibility

As mentioned in the previous chapter, the non-linear response of a crystal to an incoming electric field depends on its nonlinear susceptibility. If we assume that the presence of a domain wall alters the susceptibility of the surrounding region, it is easy to see that it will have an effect on the generated second harmonic. A number of papers have been published on this topic, including [14], [9], [26].
When assuming that domain walls change the local susceptibility, walls are either ascribed their own, different, susceptibility, or by changing the crystal structure by modification with a domain wall substructure. This can, for example, be thought of as the domain wall being represented as a collection of local defects, which will affect the local polarisation by disturbing the coherent buildup of the second harmonic signal. Later theories concerning the effect of domain walls assumed the presence of localized dc fields caused by mechanical strain in the domain wall region. [26][27]
Recent studies performed performed by S. Cherifi-Hertel et al. [9] have shown through SHG polarimetry on lead zirconate titanate(PZT, $Pb(Zr,Ti)O_3$) and lithium tantalate (LTO, $LiTaO_3$) that ferroelectric domain walls can possess their own substructure which will affect the detected SH signal. Historically, it is assumed that domain walls represent an Ising-type transition between two opposing domains. As such, the internal polarisation will decrease with proximity to the domain wall, vanishing at the wall itself, before changing sign, as schematically shown in Fig. 2.7(b). However, [9] have shown that PZT and LTO display an in-plane polarisation across the domain wall. This polarisation will rotate when passing across the domain wall, remaining either in plane with the surface of the wall (Bloch-type transition) as is depicted in fig 2.7(c) or turning perpendicular to the wall surface (Néel-type) 2.7(d).
The one trait that materials displaying different wall transition types share in common, however, is that the domain walls themselves essentially represent a thin region of material that shows sometimes wildly different symmetry properties when compared to the host medium. As such, the domain wall regions can prove to have a different non-linear tensor, thereby reacting differently to the incident fields, potentially regardless of the degree of focussing as investigated by Zhang et al. [28].

It was found that when performing (simulating) SHG polarimetry (in this case fixing the fundamental polarisation and varying the rotation of an analyzer) a fundamental polarisation perpendicular to a domain wall which is itself parallel to a crystallographic axis, will be largely unaffected by a strong focussing of the incident beam. Instead, for oblique walls that are at an angle to the order parameter axes, the detected SHG signal will be distorted regardless of focusing.

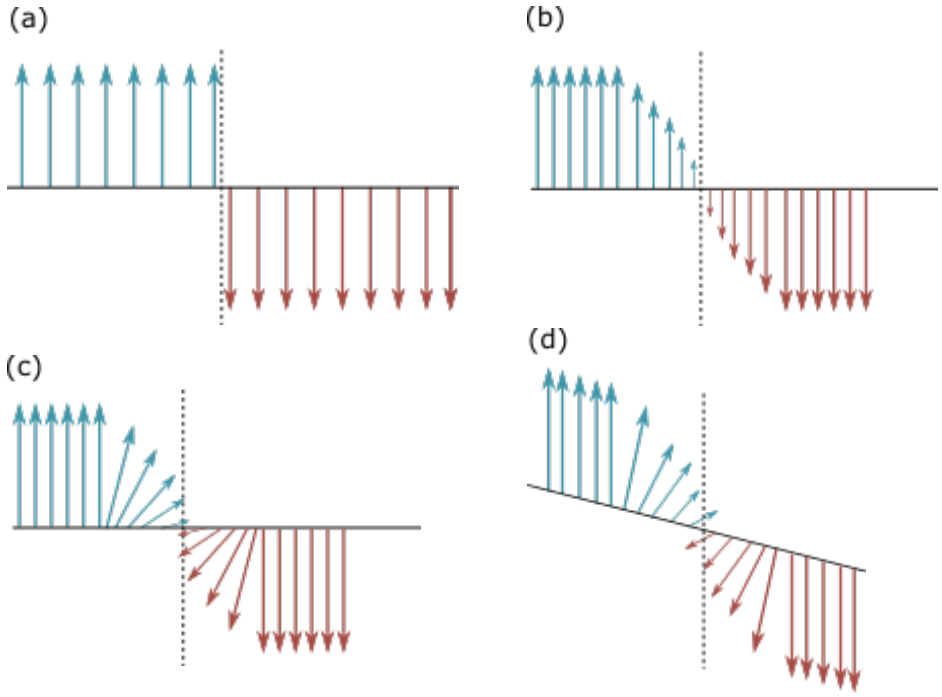

Figure 2.7: Schematic diagrams showing different models for the transition across the domain wall between two opposite domains. (a) shows the transition for an instantaneous switch between inverted polarisations; (b) depicts an Ising-type transition during which the polarisations remain (anti-)parallel and decrease in magnitude towards the domain wall; (c) and (d) show a Néel-type and Bloch-type transition, respectively. Approaching to the domain wall, the polarisation rotates perpendicular (Néel) or parallel (Bloch) to the domain wall surface. Adapted from [29]

Ultimately, the study of the exact domain wall structure and therefore the local symmetry conditions is a large topic of interest in current research. Simply based on a domain wall-caused change of the local non-linear susceptibility it is possible to explain both positive and negative contrasts as illustrated in Fig. 2.6. However, many of the effects and contrasts initially attributed to a change in the local non-linear tensor can similarly be explained by an altered phase-match or the superposition of second harmonics generated at different points within the focus, as the domain walls may not always be parallel to a crystallographic axis with a fundamental polarisation that is perpendicular as shown in the work by Zhang et al. [28]. It is therefore important to be able to differentiate phenomena of the other two mechanisms from changes of the non-linear susceptibility caused by the domain walls.

2.5.2 Defect-assisted phase-matching and Cherenkov SHG (CSHG)

A common method used for bulk-imaging of ferroelectric domain walls is the method of Cherenkov Second Harmonic Generation (CSHG). The name stems from the analogous phenomenon in particle physics, wherein a particle travelling faster than the speed of light in a medium will emit light in a cone. Similarly, during CSHG the second harmonic beam is emitted at an angle to the incident beam with the cone symmetry axis coinciding with the initial propagation direction.
CSHG is often viewed as its own investigation method and commonly used to examine domain walls in bulk samples, due to the fact that, as shown in section 2.4, SHG will usually not occur for bulk material due to the destructive interference of beams originating in front of and behind the objective focus caused by the Guoy phase shift. Instead, during CSHG any domain wall will appear as a bright line and therefore show a positive contrast compared to the surrounding domain, as shown in f.e. [30], [6] for depths of up to a few hundred μm.
The process by which the CSHG beam(s) are generated can be interpreted as a different scheme of (non-)collinear phase-matching. As presented in the previous chapter, the strong focusing of the fundamental beam can induce wave vectors at an angle to the propagation direction, thereby fulfilling the phase-matching condition of $\Delta\vec{k} = 0$.
The traditional non-collinear phase-matching condition, however, can only be fulfilled either through anormal dispersion [such that $n(2\omega) = n(\omega)$], or using a sufficiently birefringent crystal with the appropraite tensor allowing for phase-matching across two of the crystal axes. As shown by Saltiel et al. [30], however, CSHG is only possible in a crystal showing normal dispersion, so $n(2\omega) > n(\omega)$. This requires the assistance of the domain wall in supplying an additional wave-vector or quasi-momentum $\vec{G}$.
Efforts have been made to measure the width of domain walls using Transmission Electron Microscopy [31], or Scanning Probe Microscopy[32][33]. The results of different groups estimate the domain wall thickness as between a few atomic unit cells and up to 10 nm, which in either case is considerably lower than the lateral resolution, or indeed the focal spot size, of SHGM which is approximately 610 nm when employing a numerical aperture of 0.8 for a fundamental beam at 800 nm. As our lateral resolution will be insufficient to detect the domain wall as accurately as the aforementioned method, we can assume the domain wall as an instantaneous transition from a region of $+\chi^{(2)}$ to an otherwise identical region of $-\chi^{(2)}$, as is depicted in fig. 2.8. Such a transition is only possible if there exists a wide distribution of reciprocal vectors, essentially defect vectors, available at the transition point. These defect vectors are visible to non-linear optical measurement due to the change in sign of the local non-linear susceptibility.

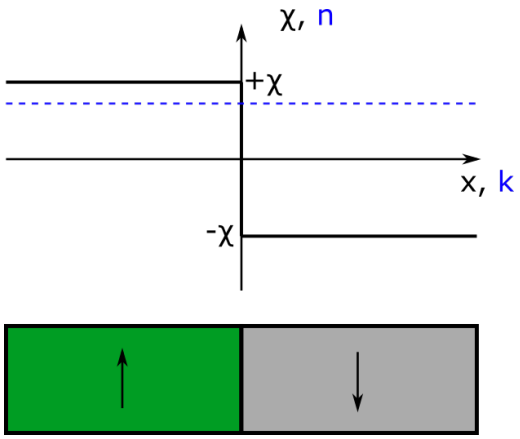

Figure 2.8: Schematic diagram of the non-linear susceptibility χ across a domain wall (black) and the population density n in k-space at the domain wall (blue)

The phase-match condition therefore becomes:

$$2\vec{k_1} - \vec{k_2} + \vec{G} = 0, \tag{2.17}$$

and is visualised in the arrow diagram in 2.9. The defect vectors supplied by a domain wall are not arbitrarily orientated, instead being either perpendicular or parallel to the boundary surface. The phase-matching condition is therefore viewed as not being fully fulfilled; instead one states that the fundamental and second harmonic beams are *longitudinally* phase-matched, neglecting the defect vector $\vec{G}$ from the phase-matching considerations and putting the wave numbers $k_1 = \left|\vec{k_1}\right|$ and $k_2 = \left|\vec{k_2}\right|$ into relation:

$$2k_1 - k_2 \cos\Theta_{CSHG} = 0. \tag{2.18}$$

In order to fulfil the above condition, k_1 and k_2 must fulfil a given relation, as is geometrically visible in fig. 2.9(c) where $2k_1$ and k_2 span the adjacent and hypotenuse of a triangle, respectively. Therefore:

$$\cos\Theta_{CSHG} = \frac{2k_1}{k_2} = \frac{4\pi n(\omega)/\lambda(\omega)}{2\pi n(2\omega)/(\lambda(\omega)/2)} = \frac{n(\omega)}{n(2\omega)} \tag{2.19}$$

Θ_{CSHG} is the opening angle of the CSHG emission cone with regards to the optical axis. It is important to note, that this angle is calculated for a beam still within the crystal itself, as is shown in fig. 2.10 in comparison to the collinear process. At the rear crystal-environment boundary, the emitted second harmonic will be refracted according to Snell's law.
Eq. 2.19 will become important in a later chapter in which criteria will be developed to selectively block the contributions from CSHG. In addition to the non-collinear CSHG signal we will be investigating as part of this work, Kämpfe et al.[6] have shown that it is also possible to observe collinearly emitted CSHG. In this case, the domain walls possess a slight

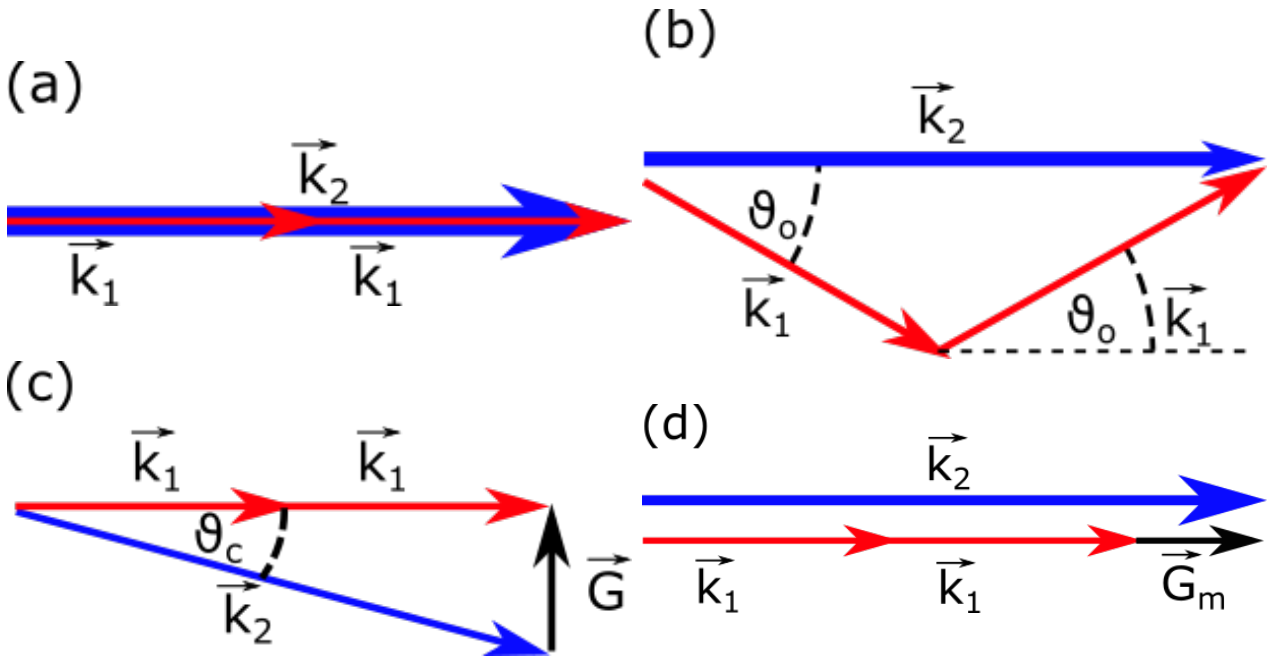

Figure 2.9: Vector diagrams showing the phase-matching geometry and emission angles for (a) collinearly phase-matched SHG, (b) non-collinearly phase-matched SHG. Subfigure (c) shows the geometry for SHG based on cherenkov phase-matching. Subfigure (d) shows the phase-matching condition for collinear CSHG as postulated by Kämpfe et al. [6] for longitudinal CSHG.

inclination and therefore are angled with regards to the optical axis. In the case of a "rough" wall, i.e. the presence of a multitude of sub-structure elements within the wall, the incident and collinear beams pass through the domain wall a number of times and experience an assisting defect vector G_m. In the following chapters, we will assume the domain walls to be a relatively smooth 2-dimensional surface within the crystal and therefore disregard the collinearly emitted CSHG light.

In addition to its use in 3D-imaging of domain structures as performed by Kämpfe et al. [6], Deng et al. proposed using CSHG to determine the width of domain walls in-situ [34]. For a focal spot far larger than the width of the domain wall, CSHG will generate two localized beams with low angular spread, whereas for a focal spot close in dimension to the domain wall itself, the generated CSHG emission is expected to be visible as a circle on a detecting screen. Based on calculations of the angular spread of the CSHG emission dependent on the ratio between the domain wall width and focal spot size, it could therefore allow for a rough estimate to be made.

Effects similar to CSHG have also been observed in Raman spectroscopy, f.e. by Rüsing et al. [35]. It was observed that the domain wall can serve as a planar defect with an associated quasimomentum perpendicular to the plane. Like the "wave vector" assumed in CSHG, this quasimomentum can help to fulfill momentum conservation conditions in certain processes, leading to phonons propagating at an oblique angle to the optical axis.

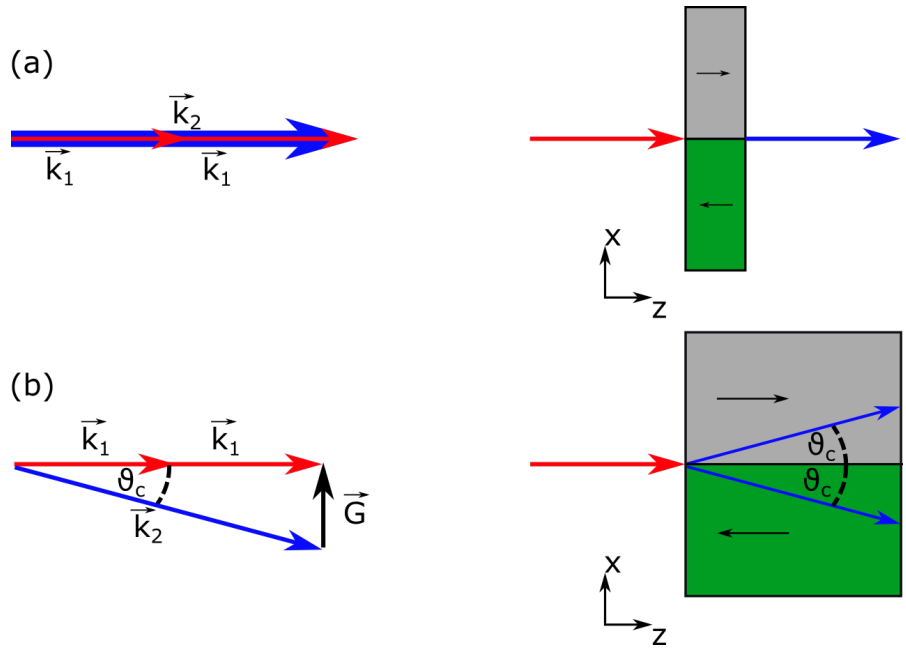

Figure 2.10: Vector diagrams comparing the phase-matching geometry and second harmonic emission direction at a domain wall for (a) collinear phase-matching, and, (b) Cherenkov-type non-collinear phase-matching. The emission angle calculated using Eq. 2.19 is only valid for inside the crystal.

2.5.3 Phase interference and superposition

The final model used to explain the presence of either positive or negative domain wall contrast is the interference of second harmonic beams generated in inverted and non-inverted domains. As the name states, during the poling or inversion process, regions of the crystal have their intrinsic polarisation and their non-linear susceptibility flipped, splitting the crystal into $+\chi^{(2)}$ and $-\chi^{(2)}$ regions. When imaging a single domain using SHG, this will have no noticeable effect. However, this changes when two opposite domains are to be imaged. If we assume the $+\chi$ region to generate a second harmonic signal at an initial phase of $\phi = 0$, then in comparison the second harmonic signal stemming from the $-\chi$ region will have an initial phase of $\phi = \pi$. As for a single domain, so long the focal spot is fully located within either domain, we will detect a certain second harmonic signal. As the focus is scanned over a domain wall which is comparatively thin compared to the focal spot, we excite second harmonic light from both domains, causing the contributions from either side of the wall to overlap in the far-field. However the signal from the $+\chi$ region retains its initial phase of $\phi = 0$ while the phase of the $-\chi$ signal is shifted by π. As such, both contributions will interfere destructively, leading to the domain wall appearing as a dark line in the surrounding domains. Fig. 2.11 serves to visualise the process.

The overlap of contributions from different parts of the focal spot is similar to the destructive interference inside a bulk crystal caused by the Guoy phase shift described in section 2.4.

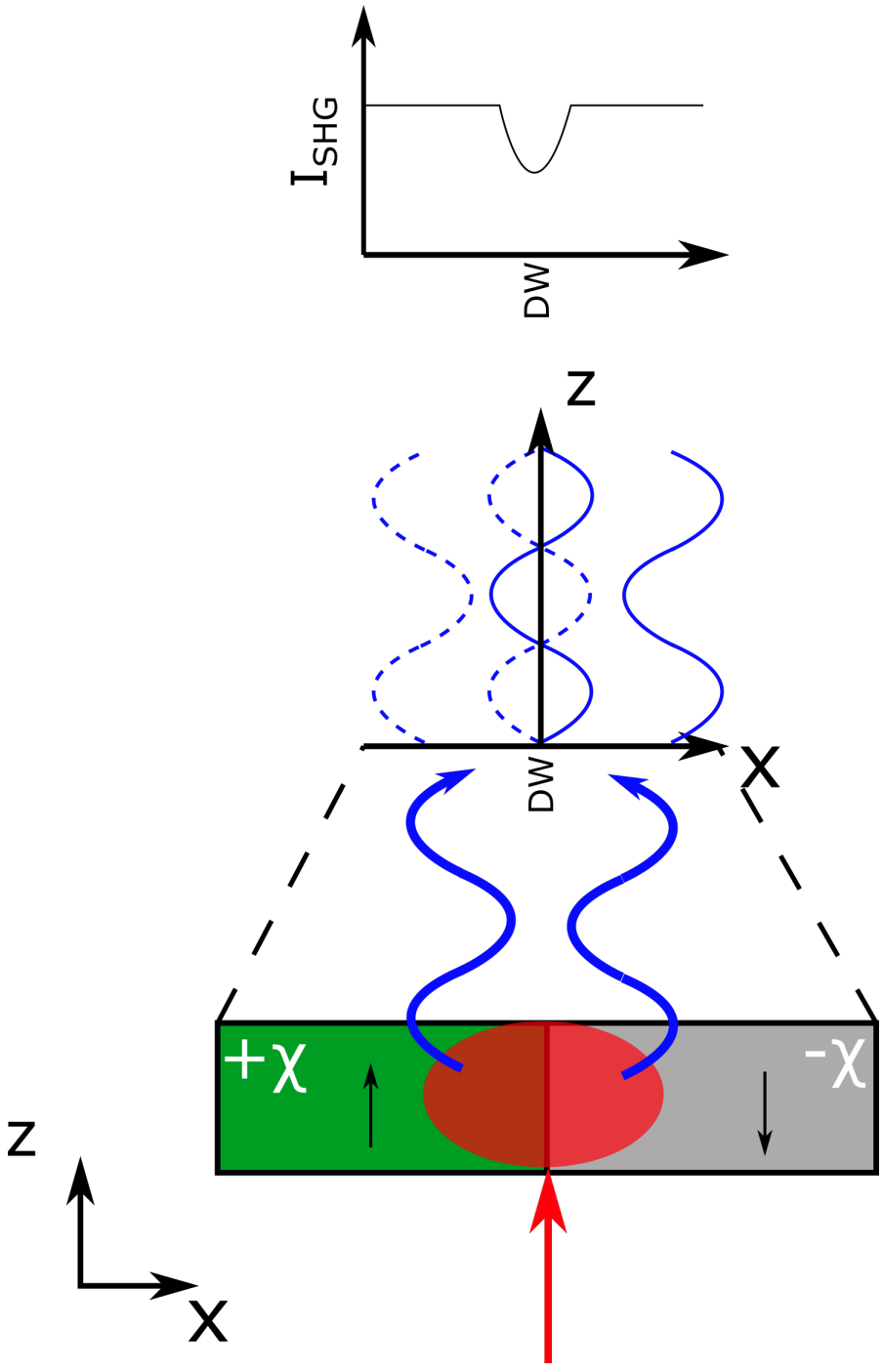

Figure 2.11: Schematic diagram of the contrast mechanism resulting from the superposition of SHG contributions from the domain wall between inverted domains. When focusing fully onto either domain, a second harmonic wave is generated with an initial phase depending on the sign of the local susceptibility, which will be detected as a signal contribution. As the focus crosses the domain wall, however, we gather contributions from both domains which will destructively interfere in the detected far-field, leading to a negative contrast at the domain wall position.

When performing SHGM, it is common practice to use a large numerical aperture in order to obtain the highest resolution and increased energy densities in the focal spot. As shown by Spychala et al. [13], however, the tighter focusing desired for SHGM induces additional components in the electric field of the focus. These components will be either along the propagation direction or perpendicular to the incident linear polarisation i.e. the focal field of a tightly focussed x-polarised beam incident along the z-axis will show components polarised in both z- and y-direction. An example is shown in fig. 2.12, where the focal field of said x-polarised beam is simulated for an objective with a numerical aperture of 0.9.

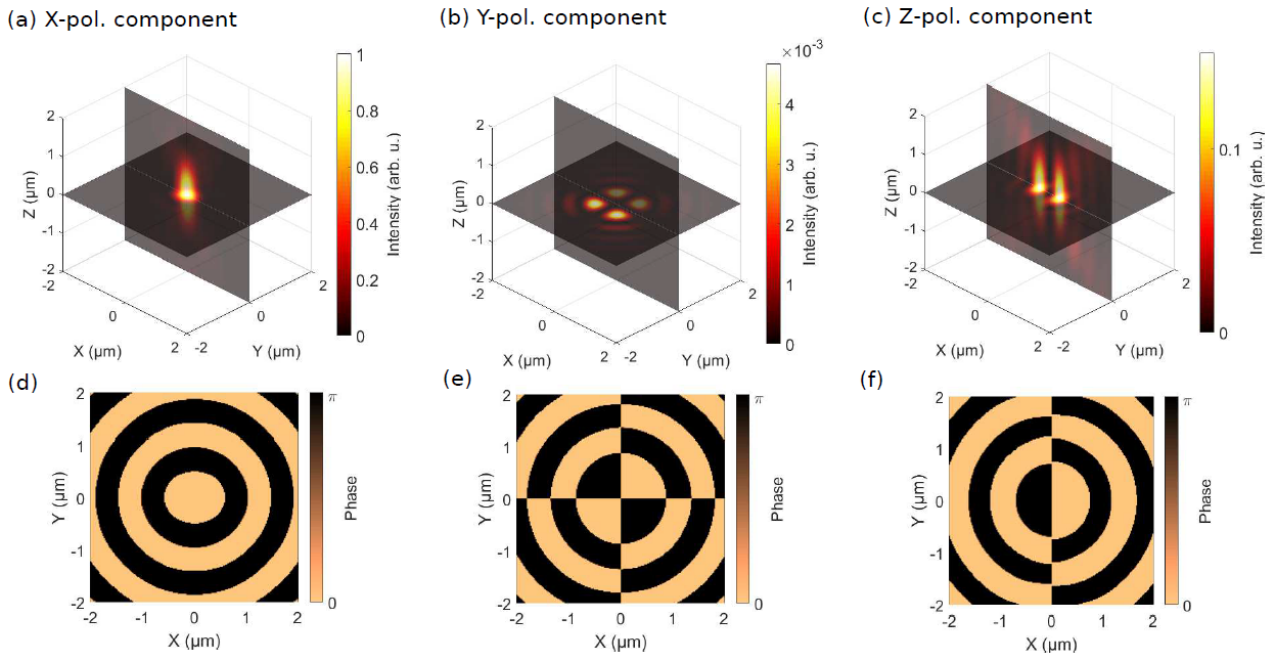

Figure 2.12: Focal field components of an x-polarised incident beam in air, simulated for a numerical aperture of 0.9. The high NA causes generation of y- and z-polarised field components showing a four-fold and two-fold split pattern in both phase and amplitude, respectively [courtesy of Dr. M. Rüsing, personal communication].

The induced field components become larger with increasing numerical aperture and cause a number of effects outside of the simple interaction of the initial polarisation with the non-linear susceptibility of the crystal. If we take the non-linear susceptibility of LN as an example,

$$d_{ij'}^{LNO} = \begin{bmatrix} 0 & 0 & 0 & 0 & d_{31} & -d_{22} \\ -d_{22} & d_{22} & 0 & d_{31} & 0 & 0 \\ d_{31} & d_{31} & d_{33} & 0 & 0 & 0 \end{bmatrix}, \tag{2.20}$$

an incoming x-polarised field along the z-axis will only generate y- or z-polarised light through interaction with either d_{21} or d_{31}, but nothing polarised in the x-axis. Both simulations and

experiments performed by Spychala et al. [24], however, have shown that this exact set-up shows a positive contrast when detection is limited to x-polarised light. This would only be possible through the interaction of a mix of E_xE_z with d_{15} of LNO, which shows that the effect of strong focusing can not be neglected when evaluating results of an SHGM measurement. An example of the effect this has is simulated in Fig. 2.13.

Here the exact situation as described in the previous paragraph is presented. An incoming linearly x-polarised beam propagates along the z-axis and the resulting second harmonic signal is collected in the back-emitted direction by the focusing objective lens. The two cases shown are the generation of x-polarised SH (a) through the mixing of E_zE_x and d_{15}, and y-polarised SH (b) via direct coupling of E_x^2 to d_{21}. The involved focal fields are as shown in Fig. 2.12, and what we see is that through the two-fold split of the induced E_z field, where the two lobes of the focal field are shifted in phase by π, the phase difference caused by the opposite sign of the non-linear susceptibility is corrected, leading to constructive interference and therefore a positive contrast. In comparison, Fig. 2.13(b) shows the direct coupling of the rotationally symmetric x-polarised focal field, which will still experience the phase shift caused by the change in sign, the signal from each domain wall will interfere destructively with the other and cause the measured negative contrast.

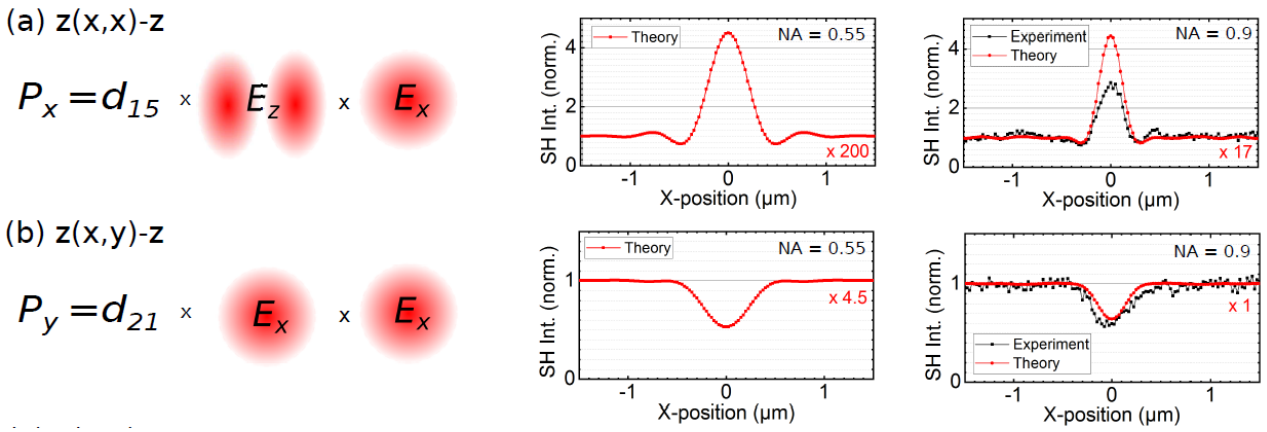

Figure 2.13: The dominating process for generation of (a)x-polarised and (b)y-polarised second harmonic light in a Z(X,(X or Y))-Z geometry in LNO. The left side of the image specifies the coupling between the relevant tensor element and the focal field components, while the right shows simulated and measured line scans for a scan across the domain wall and the resulting contrast to the surrounding domain region. [courtesy of Dr. M. Rüsing, private communication].

As we can see, there are a number of mechanisms at work during SHGM, with changes to the non-linear susceptibility being wholly dependent on the material properties and symmetries, while CSHG and (phase-)superposition effects can be the result of the technique. Ideally, we would like to fully investigate the non-linearity of the domain walls, giving us further insight

into the material. This however requires that we better understand the other two mechanisms in order to differentiate their contributions to the total measured signal. Spychala et al. have previously laid the groundwork towards understanding the effect of phase superposition and focusing [13], but little work so far has been done in order to separate out the contributions stemming from CSHG. It is for this reason that the present work will concern itself with possible methods to block or exclude the CSHG contributions, hopefully later allowing for a quantitative understanding of the effect.

3 Selective blocking of Cherenkov Second Harmonic Generation

As mentioned in the previous chapter, in order to better utilize SHGM as an investigation technique into the properties of ferroelectric domain walls and domain wall structures, it is of great importance that we be able to differentiate which contributions to the signal are caused by the domain wall and crystal itself. As there currently and to our knowledge is no way to isolate the effects of changes in the non-linear susceptibility, the logical first steps are therefore to closely examine the contributions made by both CSHG and phase superposition. Spychala et al. [13] have made impressive headway into understanding the effect of phase superposition and strong focusing on the generated signal, however, the general understanding of CSHG has yet to see a similar level of investigation. In the following chapter, we will therefore develop two criteria that should allow for a selective differentiation of CSHG contributions from the detected SH signal in lithium-niobate, hopefully allowing us to gain an initial estimate on the strength of the influence of CSHG.

3.1 Geometric blocking

As discussed in the prior section on Cherenkov Second Harmonic Generation (CSHG), the angle into which the SH is emitted depends solely on the refractive indices of the crystal under inspection both at the fundamental and SH wavelength. In order to visualise the behaviour dependent on wavelength, both the ordinary and extraordinary refractive indices were calculated for congruent lithium-niobate cLN based on the Sellmeyer equations given in "Properties of lithium niobate", compiled by Wong et al.[36]. The results are presented in Fig. 3.1(a).

As is immediately visible, the emission angle for CSHG based on the incidence of an ordinary (x- or y-polarised) fundamental beam and emission of an extraordinary (z-polarised) second harmonic (i.e. from an ordinary (o) to extraordinary (e) polarisation: o $\rightarrow$ e) is always lower than for the other two processes, these being both or ordinary incidence and emission (o $\rightarrow$ o) or extraordinary incidence and emission (e $\rightarrow$ e), respectively. It is interesting to note that a discernable emission angle does not exist for the full wavelength range in the o $\rightarrow$ e process. Instead, the angle rapidly goes to 0 for wavelengths approaching 1078 nm due to the quotient in Eq. 2.19 being larger than 1 and therefore outside of the argument range for the arccosine

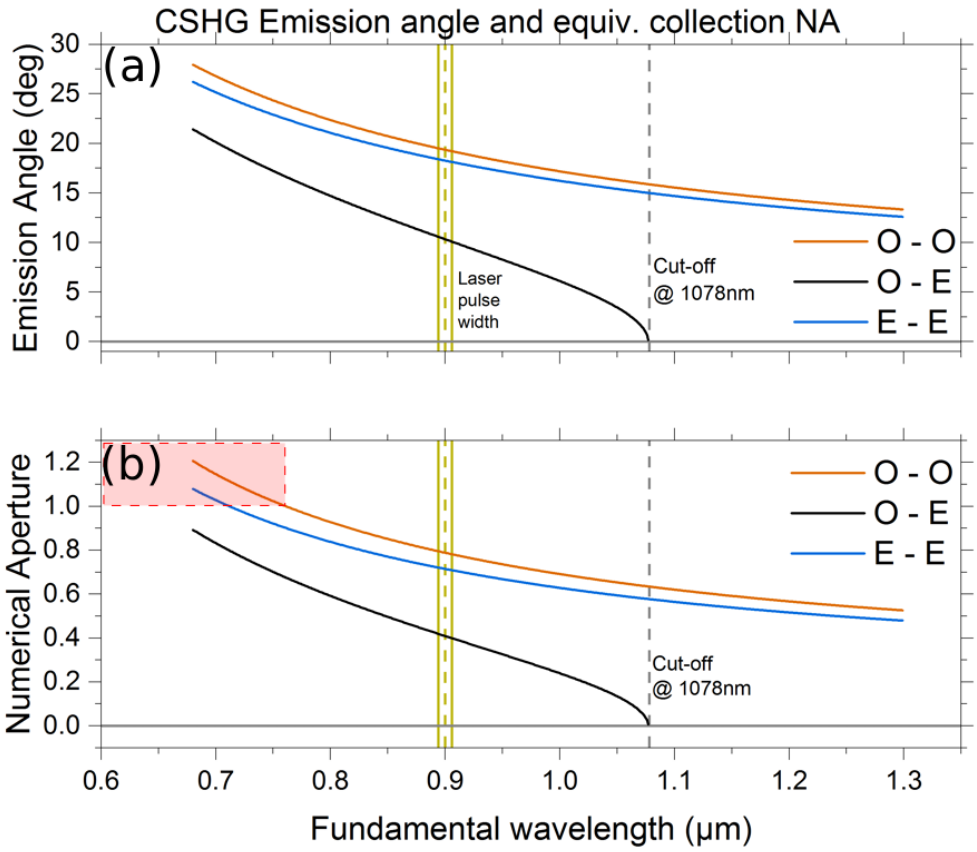

Figure 3.1: CSHG emission angle within the crystal and minimum objective NA in order to collect the CSHG light refracted out of a LN crystal into air. Plotted over the available spectral range of 680 nm – 1300 nm for each possible polarisation axis combination. Calculated using Eq. 2.19 and refractive indices calculated based on the Sellmeyer equations given in [36]. The red-shaded region in (b) marks parameter spaces that would cause total internal reflection (TIR) at the crystal-air interface.

function, i.e. flat interfaces.

The calculated angles, however, only give us the propagation angle with respect to the optical axis while still within the crystal itself. As there is currently no objective lens that can be embedded into the crystal while still allowing the sample to be scanned, it is therefore obvious that the SH beam must at least pass the crystal-air boundary at which it will be refracted. This refraction can be calculated using the refractive indices used for Fig. 3.1(a) and Snell's sine law, assuming $n_{air} \approx 1$, so that the refracted propagation angle outside of the crystal, θ_r can be calculated as:

$$\theta_r = \arcsin\left[n_{LN}\sin(\theta_{CSHG})\right] = \arcsin\left\{n_{LN}\sin\left[\arccos\left(n_\omega/n_{2\omega}\right)\right]\right\}. \tag{3.1}$$

The numerical aperture of an objective is given as $NA = n\sin(\alpha_o)$, where α_o is the opening or acceptance angle of the objective. An objective with a given NA is therefore capable of either

emitting or collecting light beams with an angular spread up to the acceptance angle. The objective is therefore incapable of collecting any beam whose propagation angle with respect to the optical axis is larger than the acceptance angle α_o.
As the refractive indices of a material will change with wavelength, we expect the emission angle of the Cherenkov cone similarly to depend on incident wavelength. Based on these internal emission angles, we can also calculate the propagation angle outside of the crystal after refraction. We can therefore calculate a "threshhold" numerical aperture NA_{lim} below which the CSHG signal can no longer be detected. Applying Snell's law and assuming a refractive index of 1 for air, we obtain this threshold as $NA_{lim} = n_{LNO} \sin(\theta_{CSHG})$. These calculations for the available wavelength range are plotted in Fig. 3.1(b). Additionally, the same calculations can be made assuming the use of an immersion objective lens and a medium such as oil. However, as the only available collection objectives for this work here were dry objectives, we only present the results for a dry objective.
As expected from Fig. 3.1 (a), we once again see that processes that originate and emit on the same crystal axis have a considerably higher threshold NA for detection of CSH emission. In the far ranges of the available wavelength range, close to 1300 nm, detection requires a NA of at least 0.5. For wavelengths below approximately 760 nm, the emitted radiation is incapable of being detected for any NA due to being confined within the crystal by total internal reflection (TIR). This is due to the refractive index of lithium niobate being an increasing function of frequency and a larger refractive index causes TIR for shallower angles.
Instead, the (o $\rightarrow$ e)-process could allow for either detection or blocking of the CSHG signal as the threshold NA changes to a higher degree across a smaller wavelength range compared to both other processes. For example, the threshold NA for a fundamental wavelength of 900 nm is calculated as 0.41, meaning that for any NA smaller than the threshold, 0.25 as an example, the signal caused by Cherenkov phase-matching will be ignored. This transition, however, will not be instantaneous as the above calculations were performed assuming a monochrome incidental beam. Instead, the real measurement is performed using a pulsed laser to generate a sufficiently high energy density in the focal spot, which includes a number of wavelengths as is shown as the yellow delimited region in Fig.3.1. One would therefore expect a transitional region in which parts of the incident pulse can still produce a detectable Cherenkov cone.
With the set-up utilised in this work, it becomes possible to vary both the fundamental wavelength of the incident beam (from 680 nm to 1300 nm) as well as the effective numerical aperture of the collection objective (from 0.09 to 0.55). We should therefore be able to verify the predictions made in fig. 3.1 in that:

1. It becomes possible to block the CSHG cone below a certain collection numerical aperture as visualised in Fig.3.2,

2. The threshold NA will decrease with increasing wavelength due to the smaller angle at which the cone is emitted (as visible in Fig. 3.1), and can be described by Eq.2.19.

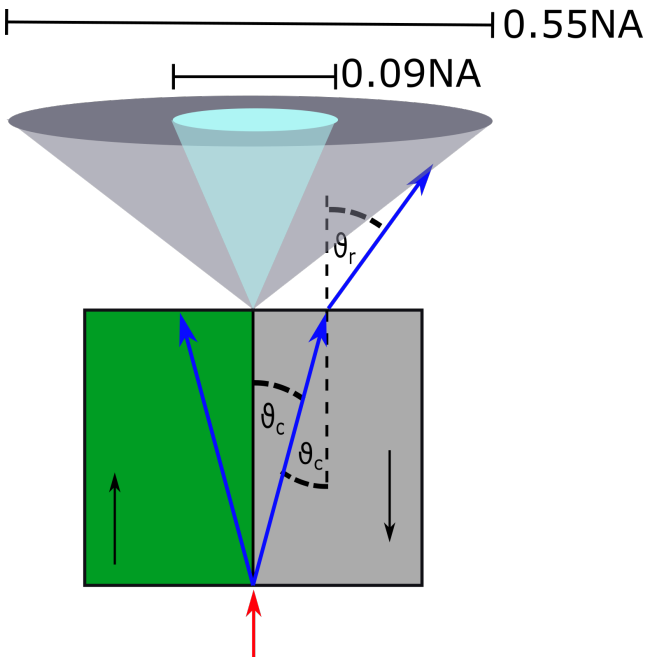

Figure 3.2: Sketch of the experimental proposal to selectively block CSHG by choosing a lower NA and therefore only collecting signals that propagate at a lower angle than the propagation angle of the Cherenkov cone. In the present case the effective NA can be varied from 0.09 to 0.55.

3.2 Dispersion switching via wavelength tuning

We now have a supposed method with which we can selectively block CSHG in the detection path. The cone itself is still generated, however, our system has simply become incapable of measuring it. Essentially, we have therefore removed the contributions to the signal that propagate at an oblique angle to the optical axis, leaving behind possibly only the signal directly correlated to the non-linear susceptibility of the domain wall $\chi^{(2)}_{DW}$. The question now would be whether it is possible to avoid the process of CSHG altogether by some combination of experimental parameters?

We have already seen in the calculations made in the previous section, that the properties of CSHG in LN can change considerably with wavelength. It therefore seems reasonable to expect that it would be possible to effectively block the generation of the second harmonic through Cherenkov phase-matching if a suitable situation can be achieved through clever choice of wavelength.

A number of works have found that CSHG is only possible for a crystal showing normal dispersion, in other words $n_\omega < n_{2\omega}$. In the case of anormal dispersion which represents the opposite case to the inequality, the emission of Cherenkov SH should therefore be forbidden.

As we have already made preparations to calculate the refractive indices for congruent lithium niobate in the previous section, we can use the same Sellmeyer equations to find whether LN

is capable of anormal dispersion. The results of these calculations are presented in Fig. 3.3, where we plotted the difference between the refractive index for the fundamental beam and the index of the second harmonic based on which direction they are polarised in. For anomalous dispersion, the resulting difference must be larger than 0.

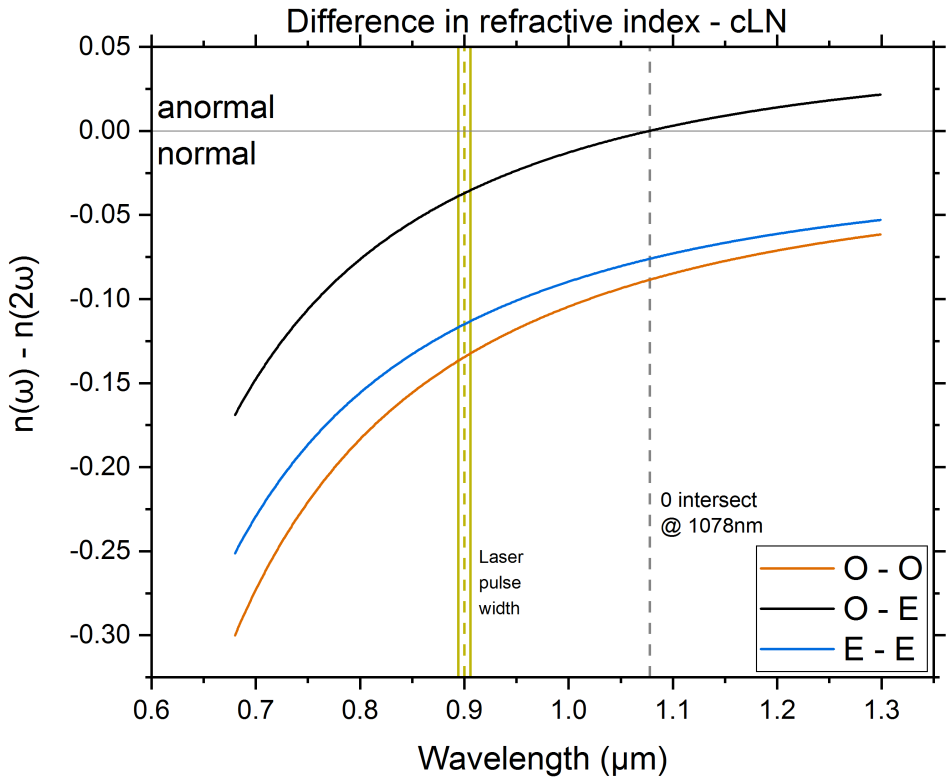

Figure 3.3: Difference between the refractive indices of the fundamental and second harmonic beam in congruent lithium niobate. Three possible combinations of fundamental and second harmonic polarisation are evaluated to discern whether anormal dispersion is possible. Ordinary incidence and ordinary emission in black, extraordinary incidence and extraordinary emission in green, and ordinary incidence and extraordinary emission in red. As mentioned in the prior section, the used laser pulse consists of a broader wavelength range. The dashed yellow marking denotes a central wavelength of 900 nm, while for a Gaussian 100 fs pulse centred around this wavelength the spectral FWHM is 11.9 nm, illustrated by the solid yellow lines.

As we can see, both processes which involve incidence and emission on the same axis will show normal dispersion throughout the entire wavelength range. As for the geometric blocking considerations in the previous section, it is once again the (o $\rightarrow$ e)-process which could show promise in "turning off" CSHG. The fact that the "Switch" from normal to anormal dispersion occurs at the same wavelength that the detection of CSHG in the previous section cuts out, should come as no surprise. The presence of said dispersion implies that $n_\omega > n_{2\omega}$, which would also cause the quotient in Eq. 2.19 to exceed 1 which is outside the allowed argument

space for the arccosine. As with the attempts to geometrically block the detection of CSHG, we expect the change in dispersion to take place over a transitional range due to the spectral width of the fundamental pulse.
In addition to the proposed switching off of CSHG, we would also expect another visible change in the scanning images. If we recall and apply the definition of the wave number to the above situation as used in Eq. 2.19, we receive:

$$0 < n_\omega - n_{2\omega} = \frac{k_1\lambda}{2\pi} - \frac{k_2\lambda/2}{2\pi} = k_1 - \frac{k_2}{2} = \Delta k/2 < \Delta k. \tag{3.2}$$

We therefore now also have a positive wave number mismatch that will increase further with higher wavelengths. As shown by Kaneshiro et al. [25] and mentioned in section 2.4, this positive mismatch will compensate for the Guoy phase shift, stopping the destructive interference that would usually occur. As such, we would expect a noticeable SH contribution originating from the bulk of the domains rather than only from the domain wall as happens for CSHG.
The proposal would therefore be to perform a number of scans at varying wavelengths below, around, and above the predicted transition point for congruent lithium niobate and to measure both the contributions from the domain walls as well as the surrounding domains. We would expect that:

1. Above the threshold wavelength, and far away from it in order to avoid generation caused by the spectral fringes of the laser pulse, the CSHG contribution stemming from the domain walls will disappear. The change from normal to anormal dispersion will in future be referred to as the "Dispersion Switch", or just "Switch".

2. There is a noticeable increase in SH signal generated in the bulk domain region, and the sum of both these effects should cause the domain walls to appear with a negative contrast with respect to the surrounding domains. This is a result of the compensation of the Guoy phase-shift by the positive wave vector mismatch due to anormal dispersion. The signal contributions from in front of and behind the focus will therefore interfere constructively.

4 Methods and procedures

The following chapter will give a brief explanation of the investigated samples and the scanning set-up employed. Additionally, a short overview of the data generation and analysis procedures will be given.

4.1 Lithium niobate (LN)

Before outlining the procedures used in the present work, a short introduction to the investigated material, lithium niobate, will be given.
Lithium niobate, chemical compostion $LiNbO_3$, is a dielectric salt only available through chemical synthesis. Its most common applications include optical waveguides and modulators, as well as f.e. piezoelectric sensors [37]. This is due to the fact that the structure itself crystalizes in a trigonal system belonging to the $3m$ point group and lacking inversion symmetry, also possessing excellent ferroelectric, piezoelectric, and pyroelectric properties.
The crystal lattice is shown in Fig. 4.1 for an unpoled and domain inverted lattice. The lattice itself consist of hexagonally-packed layers of oxygen, forming octahedra in which the Li and Nb atoms arrange themself in a sequence of "Nb, empty, Li, Nb, empty, Li", repeating with each unit cell. Within their respective octahedrons, the Li and Nb atoms are not entirely symmetric to each other, which results in an intrinsic dipole along the rotation symmetry axis (the z-axis). During domain inversion, the lithium atoms are displaced into the neighbouring vacancy, thereby changing the direction of the dipole. [33]
LN crystals are grown by ways of the Czochralski technique, in which a seed rod is dipped into a melt of lithium oxide Li_2O and niobium oxide Nb_2O_5 and slowly withdrawn. A homogeneous crystal forms at the tip of the rod which can then be cut into smaller pieces of desired orientation. Most often, the LN crystals gained by this method are so-called congruent lithium niobate (cLN) which possesses a slight lithium deficit and is therefore closer to a composition of $Li_{0.95}Nb_{1.01}O_3$. This is due to the fact that it is far easier to grow larger-scale homogeneous crystals from congruent LN as this material crystallizes and cools before it can separate into different phases, which is why the growth of stochiometric LN (sLN, *actual* $LiNbO_3$) requires the development of other methods for fabrication. [33][38] Additionally, LN can be doped with magnesium oxide MgO (leading to MgO:LN), usually in a concentration of up to 5 weight-%, which increases the optical damage threshold, allowing for use at higher intensity beams.

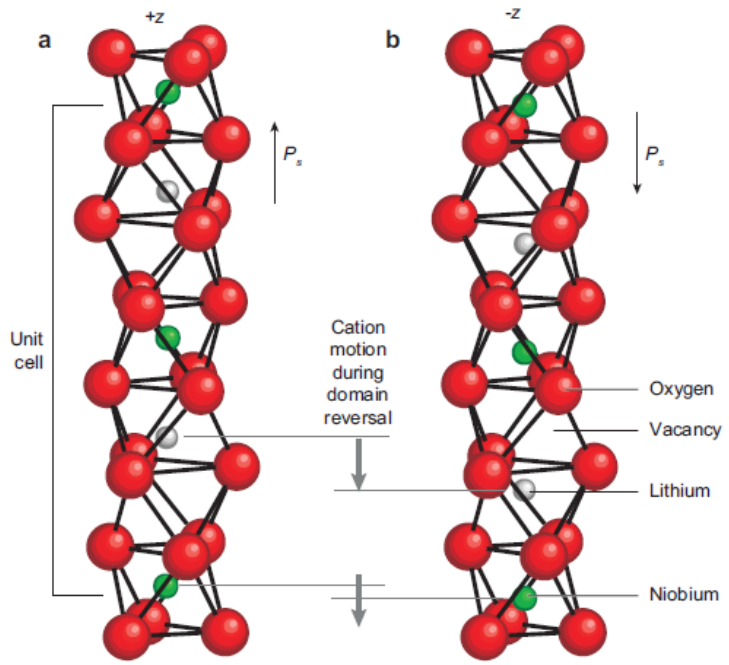

Figure 4.1: Crystal structure of lithium niobate with its hexagonal unit cell. The rotational symmetry axis is the z-axis which runs vertically in the above sketch. During domain inversion, lithium atoms are displaced to the neighbouring unit cells hence flipping the direction of the spontaneous polarisation P_s. Taken from [33].

The studies in the following chapters will primarily be centred on congruent lithium niobate.

4.2 Data generation

4.2.1 Set-up - the LightScanningMicroscope980

The microscopy environment used in this work is a Zeiss Light Scanning Microscope 980 (LSM980), access to which is generously provided by the LightMicroscopeFacility of the CMCB, TU Dresden.
The LSM980 itself uses a Ti:Sa laser module capable of multiphoton excitation between 680 nm and 1300 nm with a pulse duration of approximately 100 fs at an average beam power of 1.90 W - 2.15 W, depending on wavelength. The beam is led to the sample and scanned in the horizontal plane using galvanometric mirrors, while scanning in the axial direction was performed by a piezoelectric element in the scanning table (z-scan). Coarse positioning is possible through use of a larger piezoelectric scanner with a scanning range far exceeding the sample dimensions.
The fundamental beam is focused onto the sample through an air objective (20/0.8NA) with the generated SH light capable of being recorded both in a back-reflection geometry through the same objective, or in a forward geometry through collection by an adjustable condensor lens (0.09-0.55 NA). Spectral filtering in the back-reflected mode is performed using a Semrock F75-680 filter while the forward direction uses a Thorlabs BG39 blue glass filter. The collected SH signal is detected via PMT detectors in both branches. A sketch of the system is presented in Fig. 4.2 below.

4.2.2 Sample preparation and scanning geometry

The investigated samples originated from an industrial supplier, Deltroic Crystal Industries Inc. The sample selection included periodically-poled lithium niobate (PPLN) z-cut samples with the crystal z-axis perpendicular to the surface, of congruent (cLN), stoechiometric (sLN), and (5%)magnesium-oxide-doped LN (Mg:LN). Smaller sections were cut from each crystal to obtain rectangular samples of a $1x1x3$ mm (Y x Z x X) size.The PPLN periodicities for the poling pattern are listed in table 4.1.

The samples were then placed on a glass cover slide to lay them across the holding mecha-

Sample Nr.	Material	Periodicity	Thickness
Sample 1	cLN	30.1 μm	1 mm
Sample 2	sLN	31.4 μm	1 mm
Sample 3	MgO:LN	31.5 μm	0.5 mm

Table 4.1: List of the samples used in the present work. Each crystal was periodically poled with the given periodicity then diced and polished before measurements.

nism of the LSM980, either with their z-face or y-face aligned perpendicular to the incoming fundamental beam. Due to the small thickness of the glass slides of approx. 0.17 mm and the

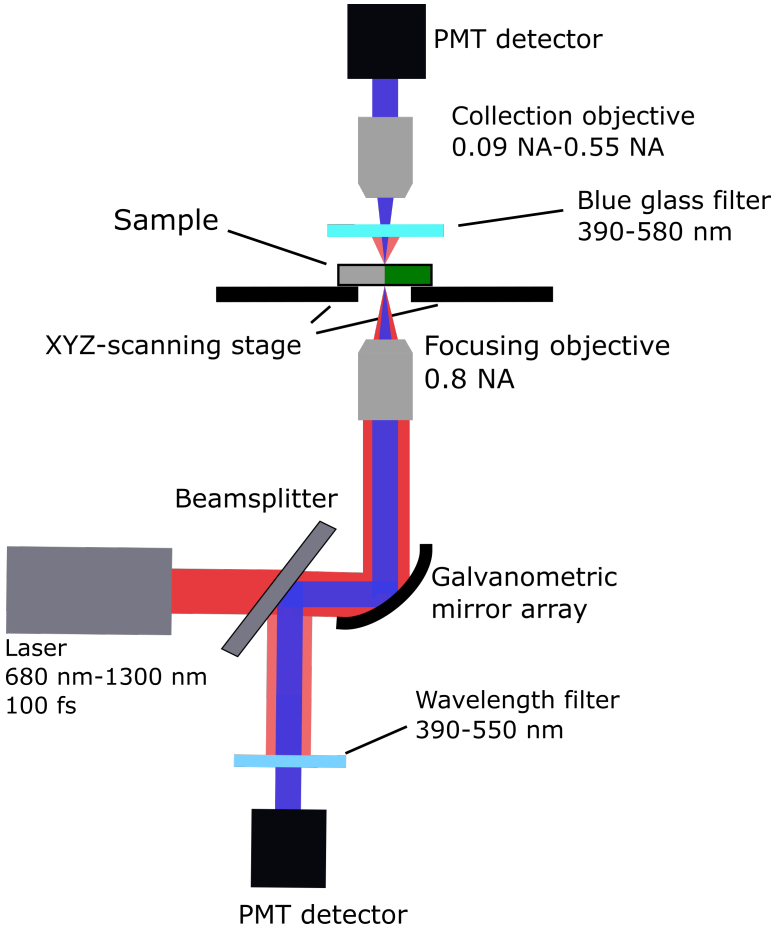

Figure 4.2: Schematic sketch of the LSM980 system set-up used to perform second harmonic generation microscopy on the LN samples. The fundamental fs laser beam can be tuned from 680 nm to 1300 nm and retains a linear polarisation while the incident polarisation is changed via rotation of the sample. The beam is scanned along the surface by galvanometric mirrors and is focused through an objective lens with a NA of 0.8. The generated SH light can then be collected either in forward or backward direction and is separated from reflected portions of the fundamental beam using a blue glass filter (forward direction) and a dichroic wavelength filter (backward direction).

cover slide correction of the focusing objective, the impact of said slide on the generated signal can be neglected.

We then performed line scans on each sample, with the lateral scanning direction chosen perpendicular to the domain walls, while the polarisation was changed by physically rotating the sample by 90 degrees. After each performed line scan, the sample was shifted axially (along the z-axis) in 50 nm steps to later compile the 2D-surface image. A schematic overview for the scanning geometry for incidence onto either the z- or y-face is presented in Fig. 4.3. Scanning images are saved as a stack of line scans with an associated axial position that will be used in the following section.

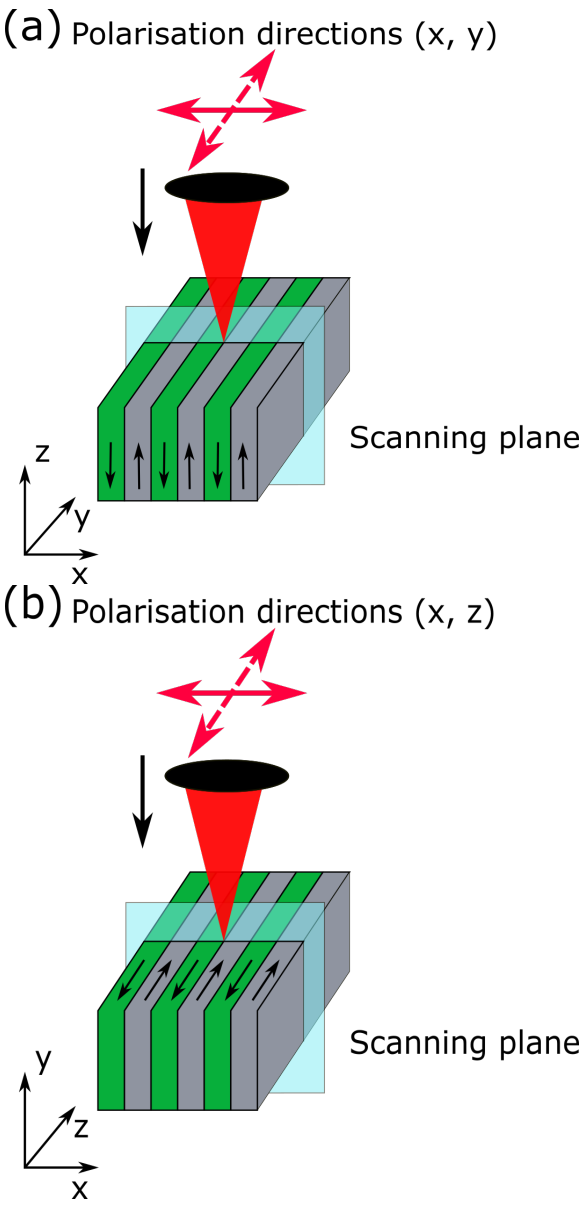

Figure 4.3: Schematic sketch of the scanning geometry performed on (a) the z-face and (b) the y-face. The depicted sample is representative of samples 1 through 3, as they were produced in the same fashion. The laser polarisation can be changed between parallel to the x- and y-axis (z-cut) or x- and z-axis (y-cut) by physical rotation of the sample. Sequential line scans were taken for increasing depths, starting outside the crystal surface and moving into the crystal in increments of 50 nm.

4.2.3 Read-out process

The .czi files that make up the scanning images for each parameter configuration are loaded into ImageJ, where each single one-dimensional line can be plotted on its own. However, as this makes a larger-scale comparison along the depth of a sample tedious, it is far more useful to generate an orthogonally projected image from the gathered line scans. This process is depicted schematically in Fig. 4.4. The collected line scans are read while the metadata of the

.czi file is taken to generate a framework with the total dimensions of the scanning image, both laterally and axially. Each line scan is then converted to a single pixle-wide strip of grayscale and inserted into the framework at the corresponding axial position. The result is a 2D-slice of the sample perpendicular to the domain walls, showing the signal behaviour at various depths at a glance.

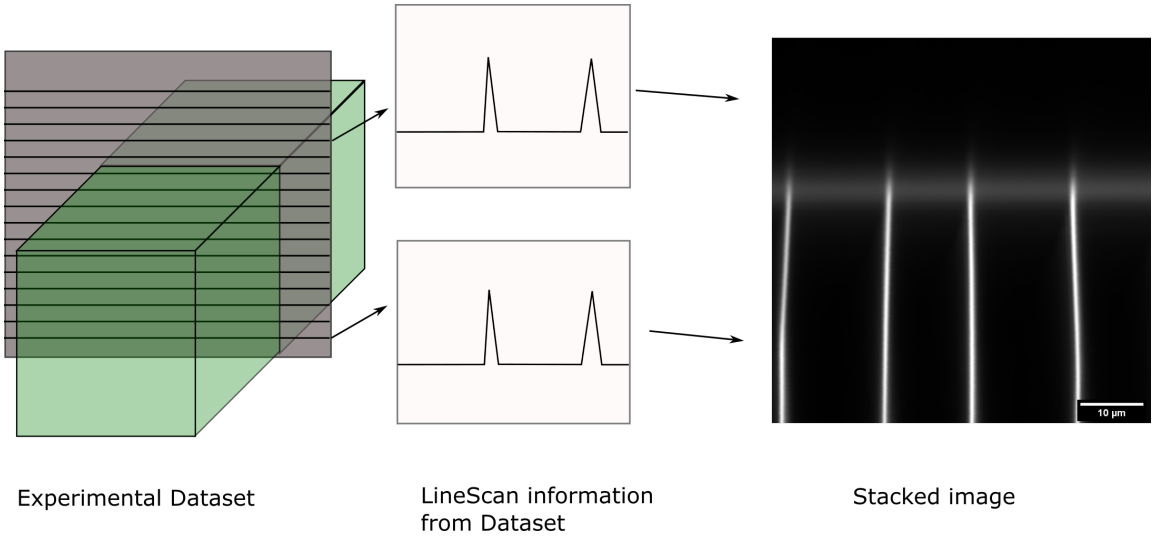

Figure 4.4: Schematic flow-diagram of the process by which the 2D image of the scanning plane in Fig. 4.3 is generated. The collected 1D line scans are converted into a grayscale strip and stacked vertically to create the 2D slice image.

These orthogonal projection images are the basis later used to extract the horizontal profile at the correct depth for each sample and parameter configuration. The process, and the line profiles required to perform it, is shown sequentially in Fig. 4.5, and consists of a number of individual steps.

The initial step is to first locate the depth or vertical position at which the surface is located. To do this, the image profile is read along the vertical axis (profile (1.) in Fig. 4.5). As shown in Fig. 2.4, this will be the position of maximum signal when scanning vertically into the domain region. The domain walls are to be avoided as they appear far brighter than the surrounding domain, thereby making an exact location of the surface difficult. Once the surface is located, it is then used to determine the exact absolute position in the image that corresponds to a desired optical depth.

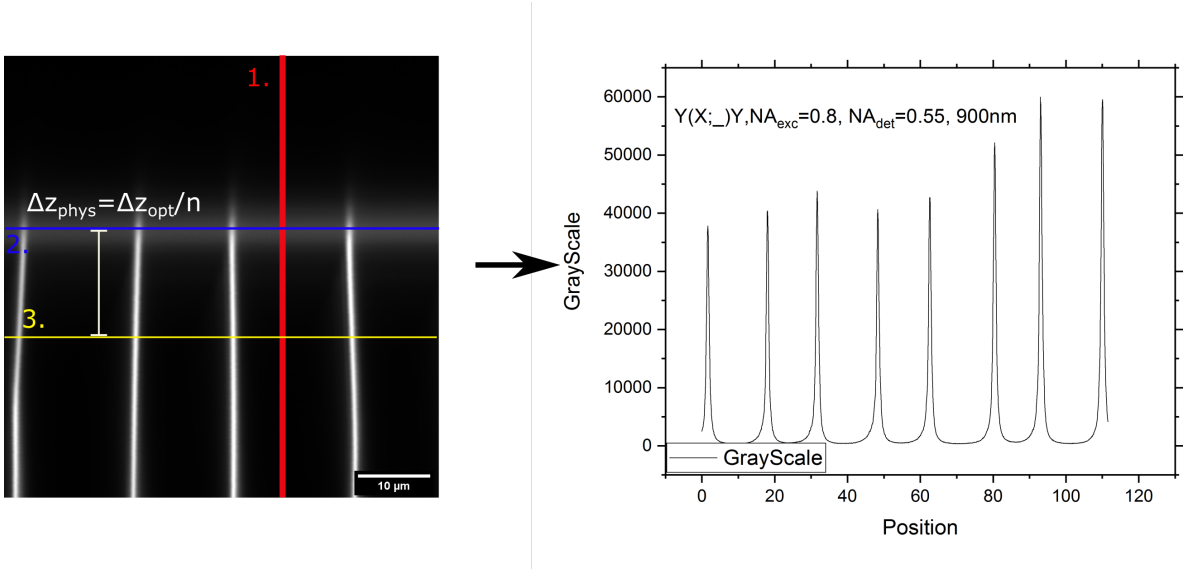

Figure 4.5: Step-by-step process by which the correct horizontal profiles are read out from the orthogonal projection. The steps are indicated by coloured lines and a corresponding number in the left cross-section image. 1.) Laying of a vertical profile through the entire image, avoiding the domain walls. 2.) Location of the sample surface as the position of the maximum signal of the vertical profile. 3.) Reading of the horizontal profile in the correct position below the surface as calculated by $\Delta z_{phys} = \frac{\Delta z_{opt}}{n}$

In the case of an overexposure (and therefore the formation of an extended plateau showing the maximum signal) the plateau is assumed to be symmetric around the surface and the median position within is taken as the surface position. As will be shown in later images, for some configurations, the maximum signal along the vertical axis does not lie at the surface. As such, the surface will be estimated from similar images and then hard-coded into the further evaluation scripts.

The optical path length of a beam is proportional to the refractive index in the medium it is propagating in, meaning that while physically two sets of two points may be the same distance apart in different media, a light beam will experience an altered path length. Examples for these effects are discussed in work done by Hell et al. [39]. The problem this causes for the images that have been compiled is that the axial or vertical position is given by the "mechanical" position of the positioning stage. As such, while it is immediately possible to start at the located surface and read the profile at the line 50 μm below it, this will not correspond to an optical depth of 50 μm, instead being closer to approximately 100 μm. A basic way to at least partially correct for this effect is to calculate the necessary physical depth by dividing the desired optical depth by the medium's refractive index as annotated in fig. 4.5:

$$\Delta z_{phys} = \frac{\Delta z_{opt}}{n} \tag{4.1}$$

This corrected vertical position is subsequently used to acquire the correct line profile, which is saved as a .csv-file.

4.3 Data processing

4.3.1 Normalisation

We now have both overview images of the measured 2D slices as well as signal profiles across the domain walls in a number of desired depths and with a number of different system parameters. Ideally, one would like to simply compare the absolute values of the signals and work from there, however due to the absence of a polarisation analyser in the detection path of the LSM980 and the fact that the efficiency of the SHG depends intimately on the addressed tensor elements, this procedure is no longer feasible. Additionally, both the supplied average laser power and the detector sensitivity depend on the wavelength, adding an additional complication. It therefore seems reasonable to normalise the signals to a set value in order to compare the trends within a set parameter configuration of orientation, wavelength, depth, focusing, and collection NAs.
In order to make the evaluation and normalisation process simpler for each extracted profile, it was decided to use the signal level of the domain regions for each individual profile as the basis for normalisation. This also allows for an easier calculation of the contrast between domain wall signatures and domain regions in later parts of this work.
In order to accept the normalisation to every depth's own domain signal, it is important to verify that any changes in the profiles with changing depth only affect the relative amplitude of features. Figs. 4.6 through 4.8 show the profile across the domain walls for depths from 0 μm to 100 μm below the surface for the same spot in the congruent LN crystal. For completeness sake, we depict here the set of profiles for a linearly x-polarised beam incident on the y-face of the crystal with a wavelength of 1050 nm in Figs. 4.6 and 4.7, and 1090 nm , within the transition range predicted in section 3.2, in Fig. 4.8.

Figs. 4.6 and 4.7 show that outside of the transition region, we can feel confident in normalising each profile to its own bulk signal level, as the only change noticeable is in the amplitude of the positive signatures. Things change for the comparison performed at 1090 nm shown in Fig. 4.8, however, as the domain wall signature does not appear as a clear positive peak, but rather as a superposition of both a negative and positive contribution. Even then, far enough away from the surface, we can see that the profile shape remains effectively constant, with a depth of around 50 μm appearing as a solid candidate on which to base our investigations of the behaviour in the bulk material.
Additionally, the average bulk signal detected in the domain region is normalised to the respective signal contribution at 50 μm and plotted for a collection numerical aperture of 0.55

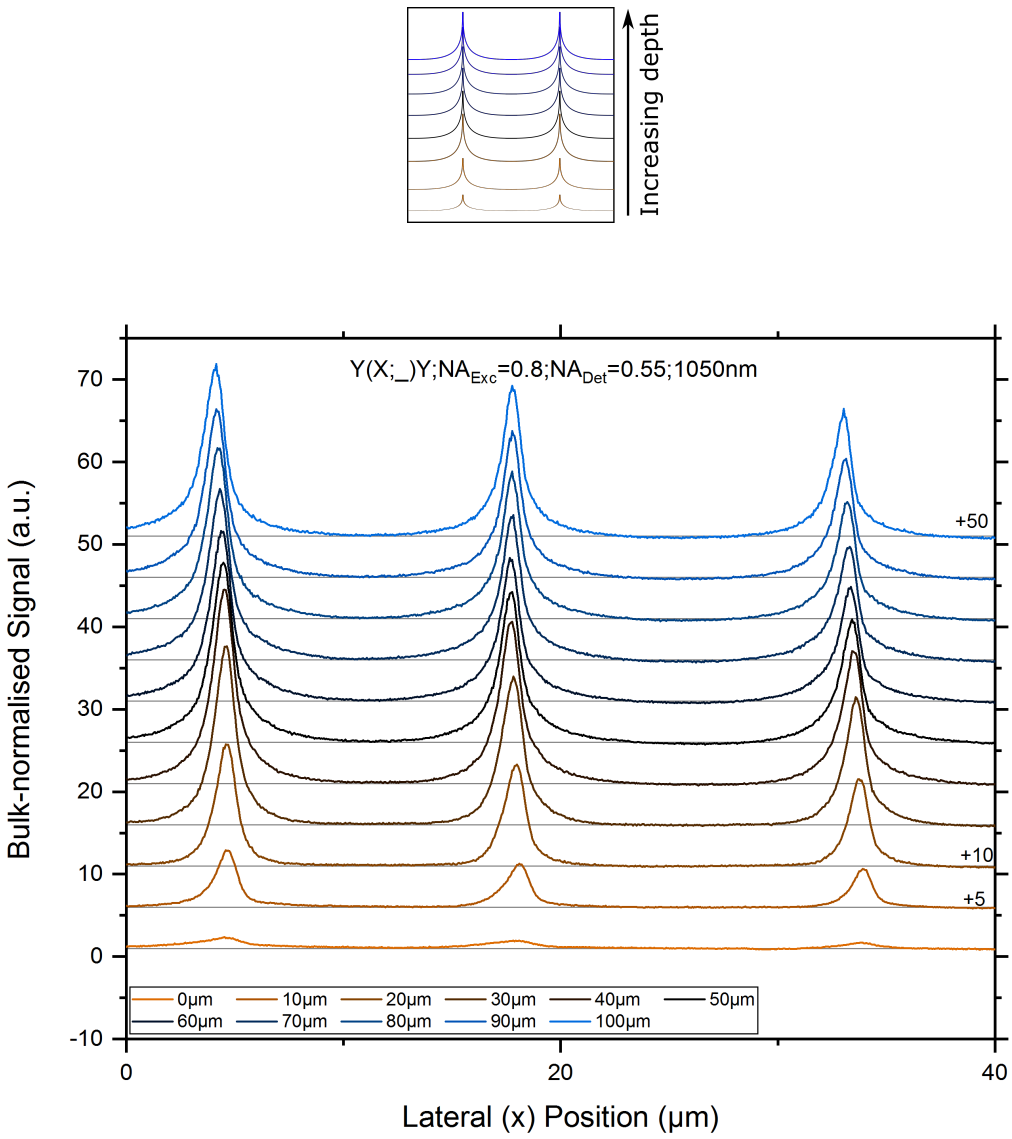

Figure 4.6: Profiles across domain walls for increasing depths below the surface in a Y(X;_)Y geometry of sample 1 at 1050 nm collected with a 0.55 NA condenser lens. Profiles are offset to each other in increments of 5 arb.u. in order to allow for an easier comparison of the profile shapes. Outside of changes to the relative signature peak height, no change is discernable for a change in depth.

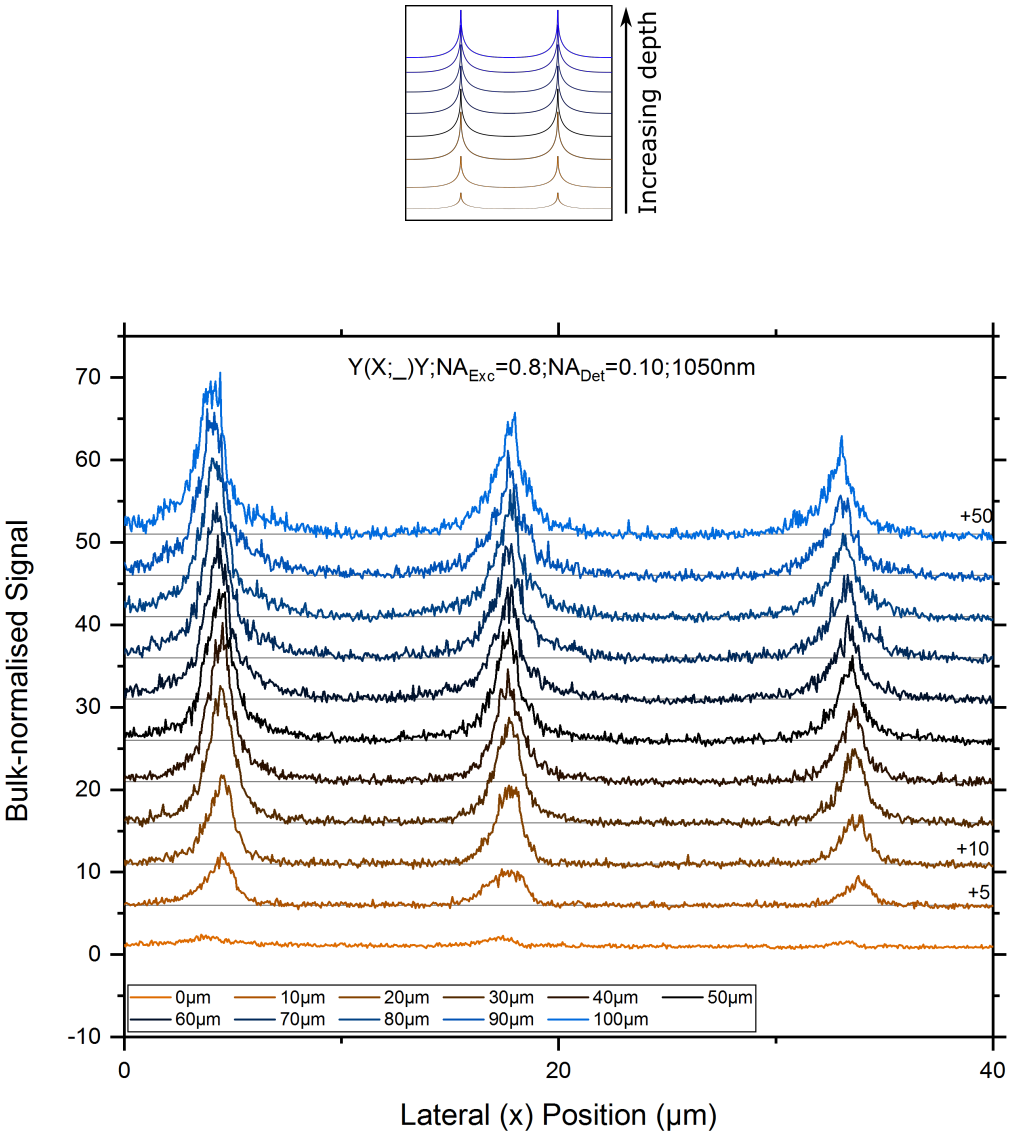

Figure 4.7: Profiles across domain walls for increasing depths below the surface in a Y(X;_)Y geometry of sample 1 at 1050 nm collected with a 0.1 NA condenser lens. Profiles are offset to each other in increments of 5 arb.u. in order to allow for an easier comparison of the profile shapes. Outside of changes to the relative signature peak height, no change is discernable for a change in depth.

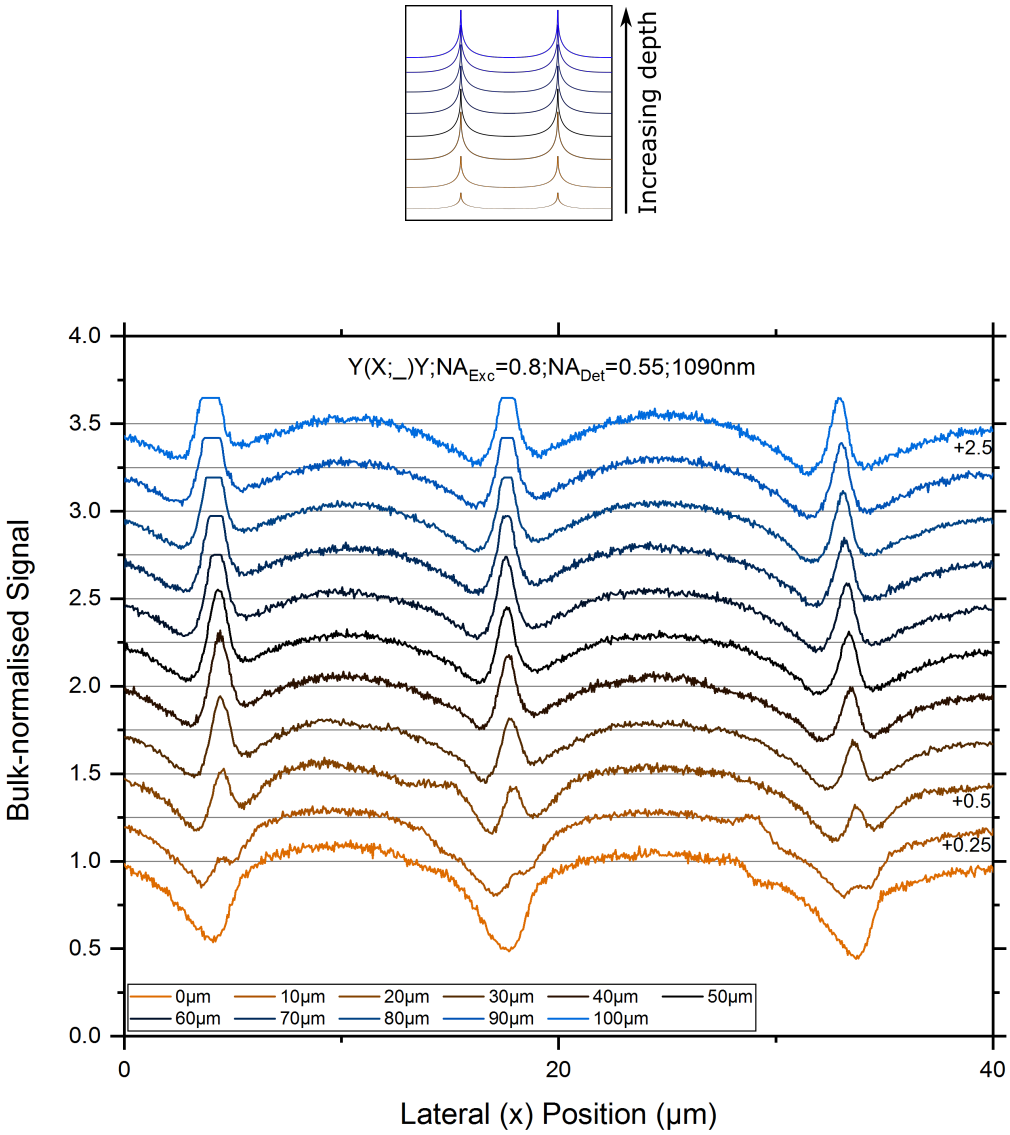

Figure 4.8: Profiles across domain walls for increasing depths below the surface in a Y(X;_)Y geometry of sample 1 at 1090 nm collected with a 0.55 NA condenser lens. Profiles are offset to each other in increments of .25 arb.u. . Unlike the profiles at 1050 nm, the transition region shows a differing behaviour wherein the domain wall signatures are no longer a purely positive contrast to the surrounding domain, but a superposition of both a negative and positive signature. Due to surface effects caused by operation within the transition region, shallower depths display a negative signature.

for 1050 nm and 1090 nm in Fig. 4.9, corresponding to Fig. 4.6 and Fig. 4.6, respectively. As shown in Fig. 2.4, the bulk signal drops rapidly with increasing depth in the crystal for the 1050 nm case, while within the transition region predicted in section 3.2, the bulk material shows an increasing contribution to the detected signal, as will be further explained in later chapters. As the increase in signal is monotonous and does not seem to fluctuate wildly, we do not expect to see any remarkable changes for increasing depths and can retain 50 μm as the reference depth for bulk behaviour.
Additional comparison images are supplied in the Appendix.

4.3.2 Fit process

A difficulty in attempting to compare the domain wall signature amplitude is caused by a slight overexposure of the detector around the domain wall signatures within the transition region, especially for larger depths within the crystal. The overexposure itself is caused by a noticeable increase of the domain wall signal intensity due to perfect phase-matching that can be achieved close to our presumed transition point between normal and anormal dispersion. The increase itself is owed to the massively increased coherent interaction length within the crystal itself close to the transition point, as the coherence length scales inversely with the difference between the fundamental and second harmonic wavelengths (compare with [24],[23]). Closer investigation of the effect is not part of this work and can instead become a point of interest in future projects.
As we would like to use the fit parameters from the non-linear fits in a later chapter, it is important to be able to estimate the accuracy of our fits, especially when the extreme end of a peak is missing due to overexposure, for example.
In order to gain a notion for said accuracy, a number of fully visible peaks from both different geometries and wavelengths were fitted using the full data range and subsequently fitted again while cutting out any value above a threshold value of X% of the peak value. As the accuracy is clearly expected to suffer if more than half of the peak is missing from the data set, more effort was put into looking at the behaviour above 50% of the peak remaining. The deviation from the unchanged peak was calculated and averaged over all investigated peaks to obtain a believable estimation.
Fig. 4.10 shows the results for the peak width in (a) and peak amplitude in (b). As expected, the accuracy decreases with further loss of information on the peak, although initially linear for the first 10 s of % loss. We can generally assume that as long as we can see the base 70% of the peak we are still within a relative deviation of approximately 35% of the actual value. For all recorded profiles, the amount of the peak that is cut off by the overexposure plateau can be roughly estimated by comparison with other peaks, as no profile showed an overexposure for all peaks contained within a profile. In general, the peaks that are cut off are usually cut off somewhere around the 80% mark, corresponding to a deviation of 20% of

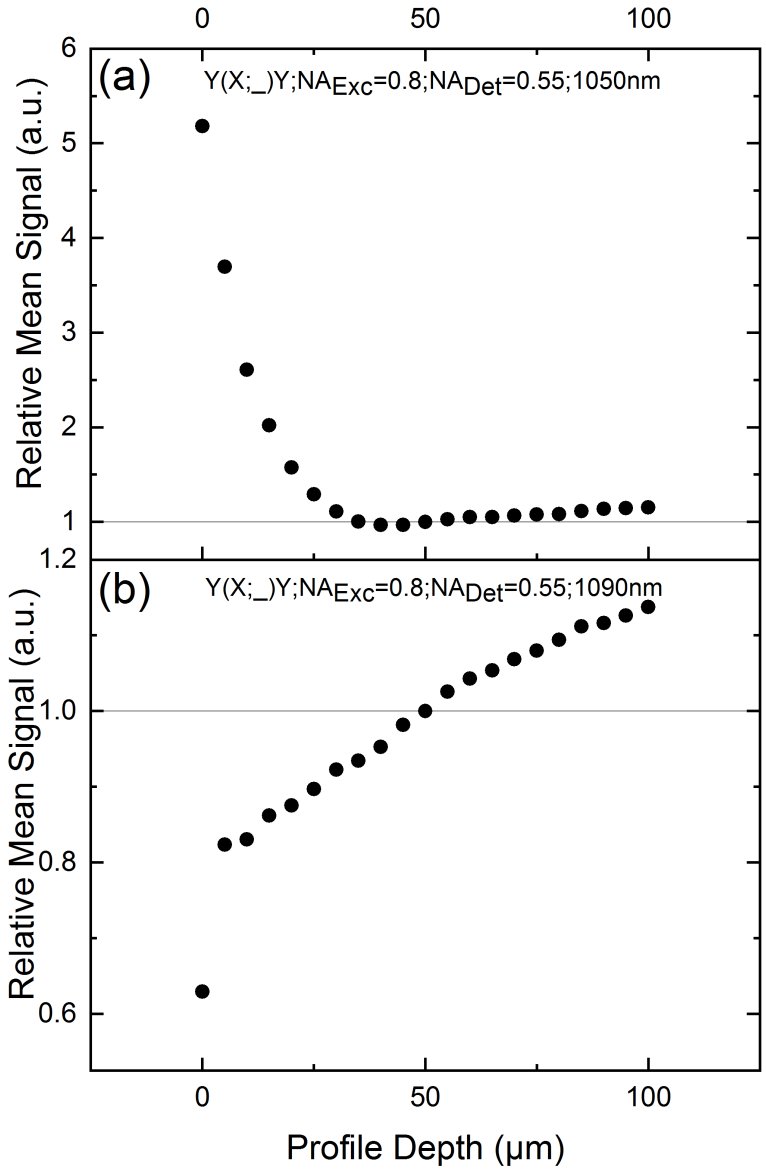

Figure 4.9: Mean domain signal over depth for a Y(X;_)Y-geometry and a fundamental wavelength of (a) 1050 nm and (b) 1090 nm, normalised to the bulk signal at 50 μm. As already shown in f.e. Fig. 2.4, the bulk signal rapidly drops off within a few µm for most cases, however above the transition point, we can clearly see the increasing contribution of the domain region.

the true values, which translates to a relative error of the fit of 25%, which will be used in the further evaluation.

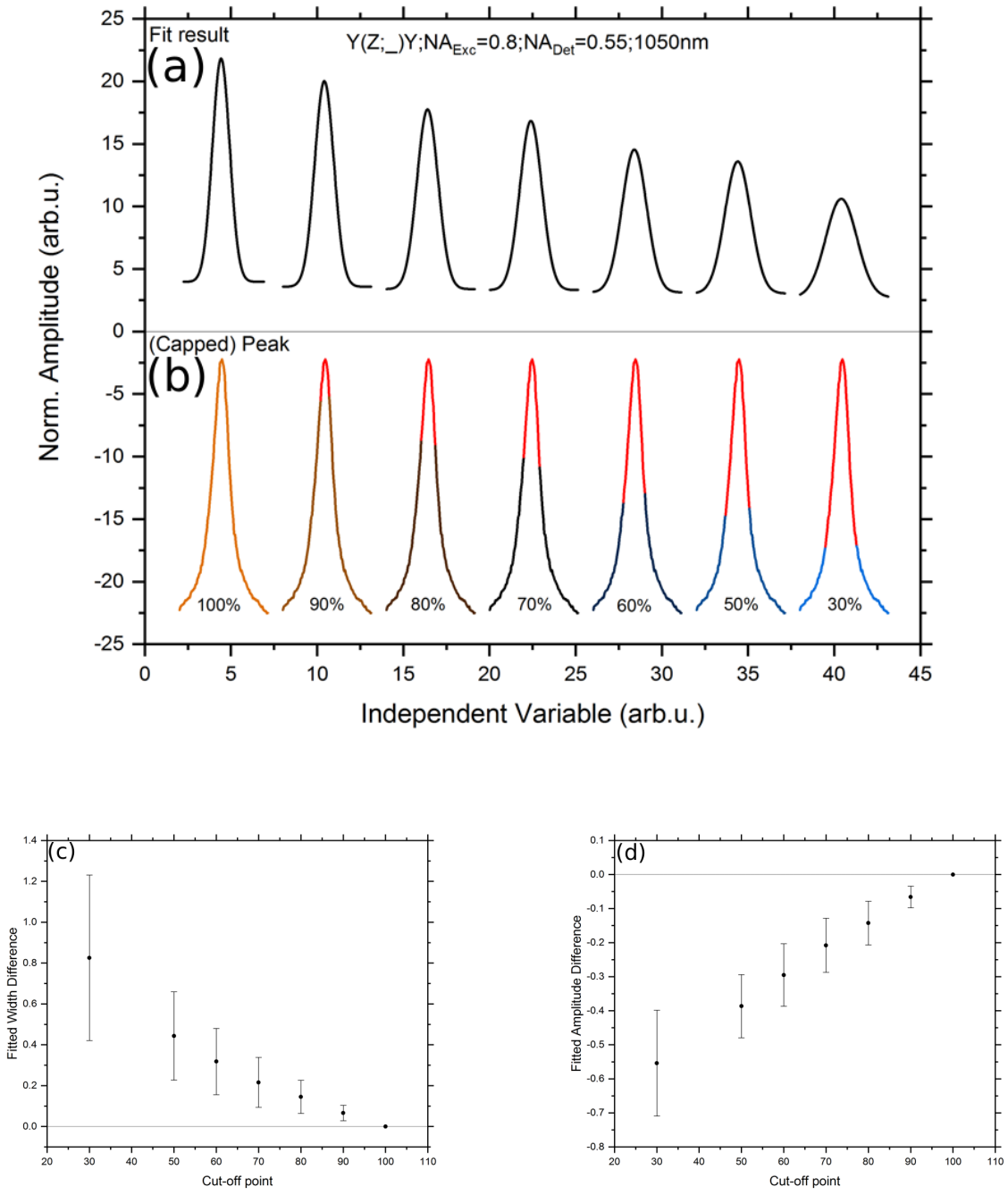

Figure 4.10: Average deviation from the actual peak parameters based on the percentage of the peak that is visible. The thresholds are calculated as the respective percentage of the peak extremum. In general we see that the width will be overestimated an increasing amount upon further loss of information while the fitted amplitude deviation increases at roughly the same rate despite the amplitude then being estimated lower than the actual value. (a): The fitted curves based on the data illustrated in (b). For (b) the curves are plotted with an increasing segment of the data points above a threshold excluded from the fitting process. These excluded data points are represented by the red section of each curve. (c): The FWHM for each fitted curve in (a), labelled $w(p\%)$, is calculated and put into reference with the FWHM of the full data set (100% curve in (b), labelled $w(100\%)$,) via $D(p) = (w(p\%) - w(100\%))/w(100\%)$. (d): The amplitude of each fit in (a) is calculated and related to the amplitude of the full data set using an analogous equation to the one used for (c).

5 Geometric blocking

The following chapter will present the results of the experiments conducted to test whether the signal contributions owed to CSHG can be blocked using geometric means. The basis for this is presented in section 3.1, as the sample is scanned for a few different wavelengths while also varying the numerical aperture of the collection objective lens. Said contributions from CSHG are emitted obliquely to the optical axis and are then further refracted at the sample surface facing the collection lens. As the NA determines the angular acceptance range of a given lens, we expect a low enough NA lens to be unable to collect the CSHG light travelling at too large an angle. Fig. 5.1 shows the same section of a y-cut cLN crystal illuminated by an x-polarised beam at a wavelength of 900 nm with a collection numerical aperture of 0.55 (a) and 0.10 (b). These numerical apertures represent the limits possible with the LSM980 system used in this work.

Both images show an XY cross-section of the crystal starting 20 μm outside of the crystal and scanning through the surface into the bulk material. We can easily see the difference between the two images in that the domain walls show up as bright lines for a collection NA of 0.55, while the 0.10 NA image shows quite a change. Within the bulk of the crystal, the domain walls are bright lines on the dark background of the domain. Outside of the bulk material, however, we see the domain walls as a dark contrast on the surrounding domain signature.
In order to better investigate the impact that a lowering of the numerical aperture has, we will first compare trends in the signatures of both the surface and the domain wall within the bulk depending on NA. As each region shows the same behaviour seemingly regardless of the collection NA, we would expect to see the same trend in each.

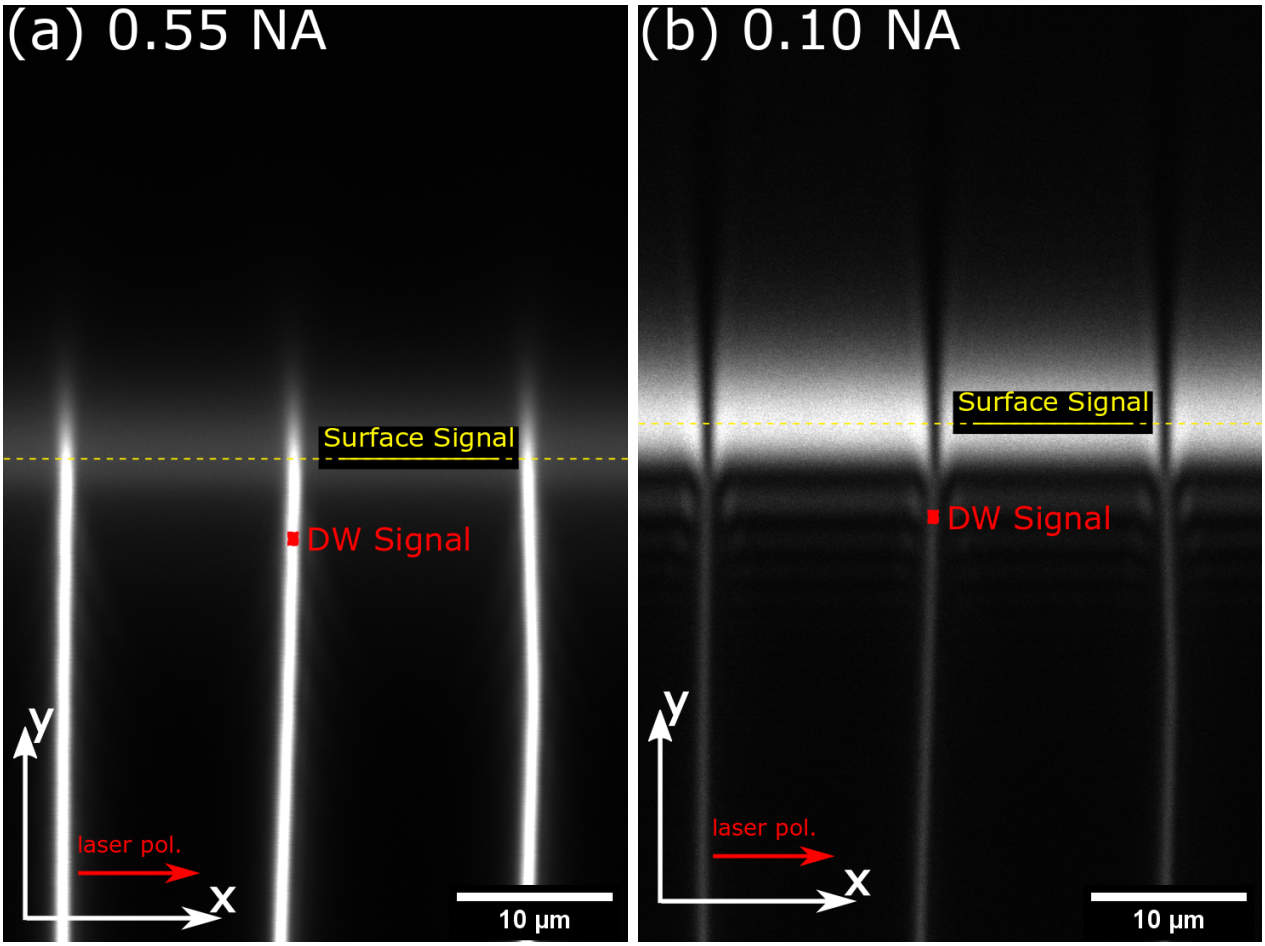

Figure 5.1: XY cross-section of a y-cut cLN crystal illuminated by an x-polarised beam incident along the crystal y-axis for a collection NA of 0.55 (a) and 0.10 (b). For the larger NA in (a) the domain walls appear as bright lines within the crystal as well as around the surface, which is visible as the lighter are towards the top of the image. The 0.10 NA image, (b), on the other hand shows a negative contrast for the domain walls outside of the crystal bulk, but still a positive contrast within. The contrast of each image was adjusted in order to improve visibility, it does not represent a usable tool for comparison.

5.1 Emission characteristics

Before investigating the behaviour of the sample, we shall first have a look at the effect that we would expect a change in NA to have on the detected signal. As explained prior, the numerical aperture of an objective lens specifies the angular range that said lens is capable of collecting, larger NAs therefore logically collect more light. We would like to know, however, how this changes with larger or smaller apertures.
Let us assume an ideal point-emitter in vacuum with isotropic radiation. In this case we will focus on the angular dependence as that is the parameter we can change through our choice of NA. We will further limit our investigation to a single hemisphere in the forward direction, as an objective lens in a transmissive geometry cannot detect backscattered light.
An objective lens will collect all light emitted at angles at or smaller than its acceptance angle $NA = n \cdot sin(\theta) \Rightarrow \theta = asin(\frac{NA}{n})$, as such we can integrate over the intensity emitted into the cone with said angle θ and divide the result by the total intensity emitted into the hemisphere. For an ideal point emitter the collection ratio R_C is then:

$$R_C = -[cos(\theta) - 1]. \tag{5.1}$$

However, the light generated during SHG is the result of radiation from the polarisation induced by the interaction of the incoming laser beam with the non-linear tensor of the material. This polarisation for congruent lithium niobate can be calculated as:

$$\begin{aligned}\begin{pmatrix} P_x \\ P_y \\ P_z \end{pmatrix} &= \begin{bmatrix} 0 & 0 & 0 & 0 & d_{15} & d_{16} \\ d_{21} & d_{22} & 0 & d_{24} & 0 & 0 \\ d_{31} & d_{32} & d_{33} & 0 & 0 & 0 \end{bmatrix} \begin{pmatrix} E_x^2(\omega_f) \\ E_y^2(\omega_f) \\ E_z^2(\omega_f) \\ 2E_y(\omega_f)E_z(\omega_f) \\ 2E_x(\omega_f)E_z(\omega_f) \\ 2E_x(\omega_f)E_y(\omega_f) \end{pmatrix} \\ &= \begin{pmatrix} 2d_{15}E_xE_z + 2d_{16}E_xE_y \\ d_{21}E_x^2 + d_{22}E_y^2 + 2d_{24}E_yE_z \\ d_{31}E_x^2 + d_{32}E_y^2 + d_{33}E_z^2 \end{pmatrix}\end{aligned} \tag{5.2}$$

In the investigated case an x-polarised incidental beam was used to generate the polarisation. As will be explained in more detail in the chapter concerning dispersion switching, and has similarly been shown by Amber et al. [23], the dominant resulting polarisation (and therefore dipole) will be orientated parallel to the crystallographic z-axis.
For a dipole parallel to the crystallographic z-axis, the radiation pattern is proportional to $(1 - \cos^2\theta_z)$, where θ_z is the angle with regards to the z-axis. Similar to the case of the point

emitter, we can calculate which portion of the light emitted into the forward hemisphere within a cone of opening angle θ. As our objective is positioned along the y-axis with respect to the dipole, we are therefore interested in the light emitted into an angle θ_y around the y-axis. This means that the previous $(1 - \cos^2\theta_z)$ behaviour becomes $\cos^2\theta_y$. The situation is sketched out in Fig. 5.2.

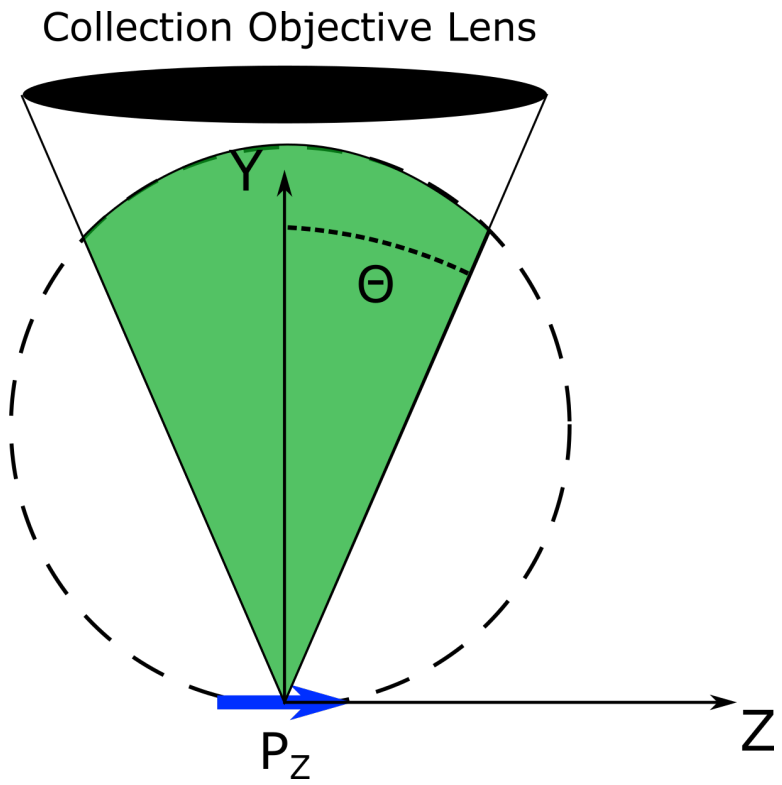

Figure 5.2: Dipole radiation of a dipole oriented parallel to the z-axis is collected by a collection objective with an acceptance angle of θ_Y located along the y-axis. The collected fraction of the emitted radiation is shaded in green.

As the angular distribution is symmetrical with regards to the y-axis, we are able to limit the integration boundaries to 0 and $\pi/2$ and must only double the result of the integration. However, as both the numerator and denominator contain the factor of 2, we can neglect it. The ratio of collected light to total emitted light thus can be calculated as:

$$R_C = \frac{\int_0^{\theta_y} \cos^2\theta_y d\theta_y}{\int_0^{\pi/2} \cos^2\theta_y d\theta_y}. \tag{5.3}$$

The ratios for both a point emitter as well as dipole radiation in vacuum are presented in Fig. 5.3 dependent on the collection angle.
The above figure represents the ideal case in which the radiation occurs in vacuum. However, in the present experiment, the polarisation is generated within the lithium niobate crystal and

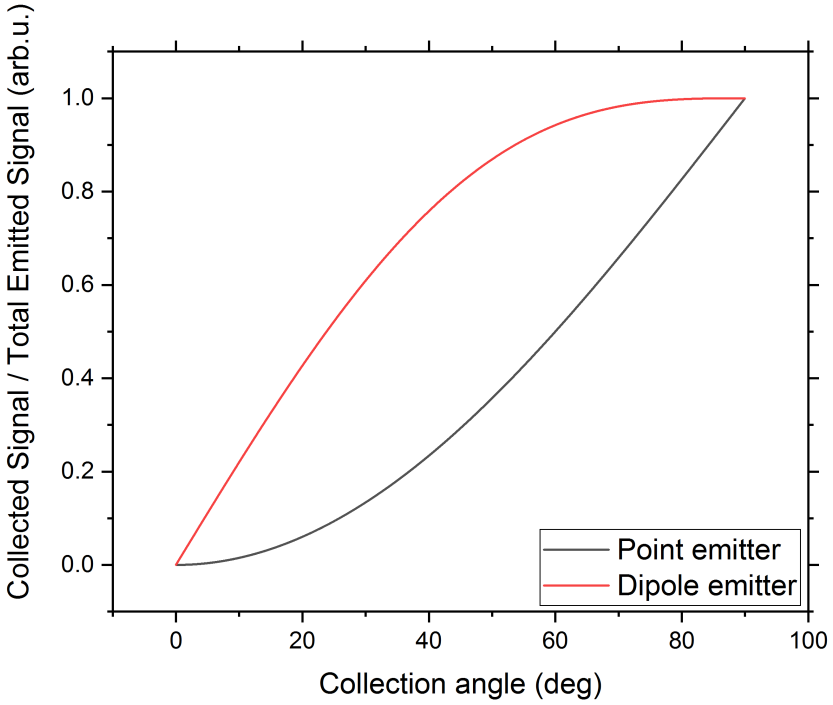

Figure 5.3: Ratios of collected light to total emitted light for point emitter (black) and dipole (red), each in vacuum, for a given collection angle $\theta = \arcsin(NA)$ in air.

must then be refracted outside of the crystal according to Snell's law $n_{LN} \sin \alpha_{crystal} = \sin \alpha_{air}$, n_{LN} the extraordinary refractive index of lithium niobate at the second harmonic frequency, here 450 nm. Additionally, there will be reflection at the boundary between the medium and air with the reflection being given by the Fresnel equations.
As we have a maximum collection NA of 0.55, we also have a maximum angle of emission within the crystal which we are still capable of collecting, which can be calculated from Snell's law for a 900 nm fundamental to:

$$\sin \alpha_{max} = 0.55/2.2809 \rightarrow \alpha_{max} = 13.95° \tag{5.4}$$

It therefore makes sense to use the signal collected up to an angle of 13.95° as the normalisation factor for future plots. Fig. 5.4 shows the collected signal from a dipole within an LN crystal with and without consideration of the Fresnel equations. For lower angles, the reflection coefficients do not change much with a change in angle. Our maximum collection angle is only 13.95°, so we are still within the range in which this is the case. We can therefore safely disregard the slight change in reflectivity from a change in angle of incidence to the surface. From Fig. 5.4, we would expect a linear scaling of the collected signal with an increase in

NA. We will now look at the ratio of the collected signal compared to the signal gathered at

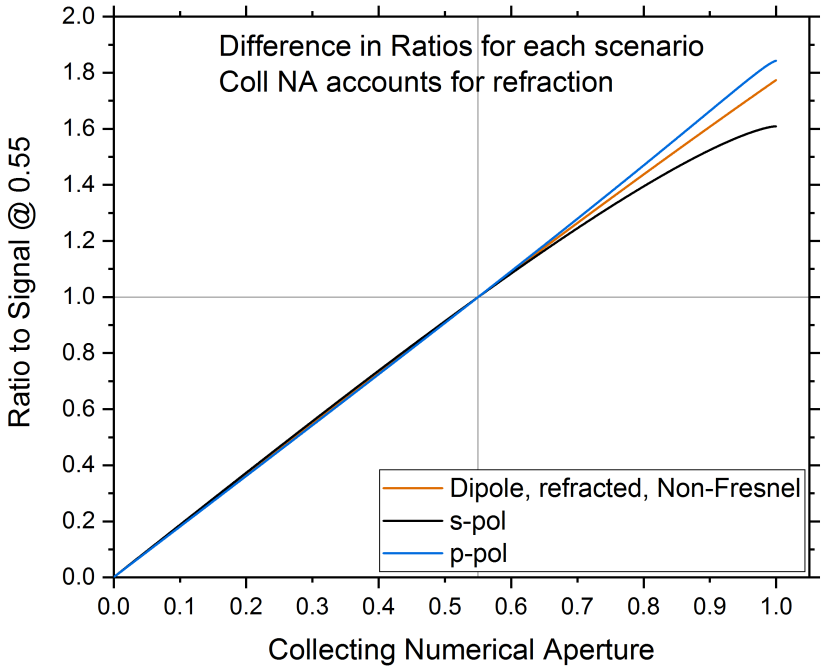

Figure 5.4: Ratio of the signal collected by a given NA to the signal gathered by an objective lens with an NA of 0.55. The dipole is within the lithium niobate crystal and the emitted light is refracted off the crystal-air boundary. The ratio disregarding any influence of the change in reflectance according to the Fresnel equations is shown in brown. The black and blue curves show the corresponding curves for s- and p-polarised light, respectively.

a numerical aperture of 0.55 for three different wavelengths in the congruent lithium niobate crystal. As per section 3.1, the threshold NA below which the CSHG contributions should disappear was calculated and is listed in Table 5.1.

Wavelength	$n_{LN}(2\omega)$	Threshold NA
900 nm	2.2809	0.409
950 nm	2.2631	0.325
1000 nm	2.2486	0.240

Table 5.1: Threshold NAs below which the light emitted via CSHG should not be collected by the objective lens.

The wavelengths investigated are 900 nm, 950 nm and 1000 nm, with the ratios of the collected signal to the 0.55 NA signal presented in Fig. 5.5. The plots also include the theoretically expected behaviour for both a dipole emitter within the LN crystal, as well as a point emitter in vacuum in order to have a direct comparison. Each wavelength was sampled in steps across

the range in broader steps, with a finer graduation of 0.01 being used near the transition points presented in Tab. 5.1.
We can see that the surface signal behaves close to like we would expect for a dipole located within the lithium niobate crystal. That is, we see a more or less linear increase with increasing NA to begin with, although there is a slightly slower rate of change towards our maximum NA. This behaviour also seems unaffected by the wavelength with which we investigate the sample.
For all three wavelengths, however, the domain wall signal shows an obvious deviation both from the surface signal as well as the expected behaviour for the dipole. An initial slow increase is followed by a sharp change in the slope as soon as a certain threshold NA is reached. Based on this we can assume that there is indeed some additional contribution to the signal which we cannot detect with a lower NA, as we would expect for the oblique CSHG light. While we cannot definitively show that this contribution is caused by CSHG, the behaviour of the signal can be best explained by CSHG.

In order to obtain an estimate on where the threshold NA for each wavelength lay, we calculated the discrete derivatives $D[i]$ of the data points, using the counts $S[i]$ as:

$$D[i] = \frac{S[i+1] - S[i]}{NA[i+1] - NA[i]}, \tag{5.5}$$

The switch point was then determined as the NA at which the sudden increase in signal strength begins, as prior to the switch the derivative shows a roughly linear behaviour. An estimate for the relative error of the calculated points was gained from the propagation of uncertainty for the discrete derivative $D[i]$ resulting in Eq. 5.6, where we used a relative error of 1% of the signal level and an NA error of 0.002:

$$\begin{aligned}(\Delta D[i]_{rel} \cdot D[i])^2 =& \left(\frac{1}{NA[i+1] - NA[i]}\right)^2 \cdot (0.01 \cdot S[i+1])^2 \\ &+ \left(\frac{1}{NA[i+1] - NA[i]}\right)^2 \cdot (0.01 \cdot S[i])^2 \\ &+ \left(\frac{S[i+1] - S[i]}{(NA[i+1] - NA[i])^2}\right)^2 \cdot (0.002)^2 \\ &+ \left(\frac{S[i+1] - S[i]}{(NA[i+1] - NA[i])^2}\right)^2 \cdot (0.002)^2.\end{aligned} \tag{5.6}$$

This relative error of the discrete derivative was then taken as the relative error of the measured threshold NA. The results are listed in Tab. 5.2 and plotted in Fig. 5.6 alongside the expected threshold NAs for the accessible wavelength range.
We can see from Fig. 5.6 that the threshold NA does in fact decrease with higher wavelengths as predicted in chapter 3.1. As the errors included in Fig. 5.6 were based on the relative error

Wavelength	Threshold NA
900 nm	$0.41 \pm 30.1\%$
950 nm	$0.34 \pm 30.3\%$
1000 nm	$0.29 \pm 28.7\%$

Table 5.2: Threshold NA values calculated from the discrete derivatives of the signal level dependent on collection NA. Calculated for 900 nm, 950 nm and 1000 nm

of the discrete derivative calculated with a limited step size, the actual error may be slightly lower. However, due to the close match to the theoretical values, even without the error bars, it seems very much likely that the behaviour is due to CSHG emission within the crystal.
To summarise, based on the ratios of the collected signal to the maximum collected signal, we can show that the emission from the sample surface behaves as if it originated from a dipole placed shortly beneath the surface. On the other hand, the domain wall signal shows an additional contribution above a certain threshold NA, which causes a rapid increase in signal. This threshold also decreases for higher wavelengths, which would be expected from the smaller CSHG emission angles calculated in chapter 3.

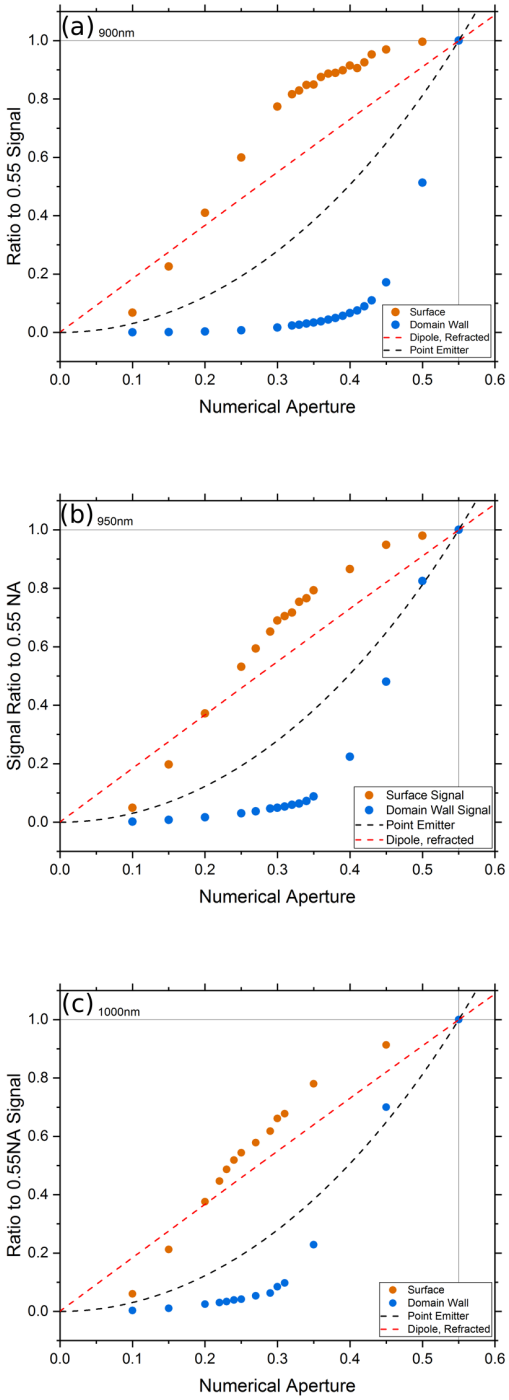

Figure 5.5: Ratio of the collected signal to the signal collected using a numerical aperture of 0.55 for (a) 900 nm, (b) 950 nm, (c) 1000 nm plotted over the corresponding collection NA. The plots include the theoretical behaviour for a point emitter in a vacuum and a dipole emitter within a lithium niobate crystal. The surface signal behaves close to how we would expect a dipole emitter to behave for all three wavelengths. In contrast to this, the domain wall signals behave neither like a dipole nor like a point emitter, as is visible by the sudden sharp increase in signal contribution upon exceeding a certain threshold NA. It is important to note that the threshold NA decreases with an increase in wavelength, as predicted in Ch. 3.1.

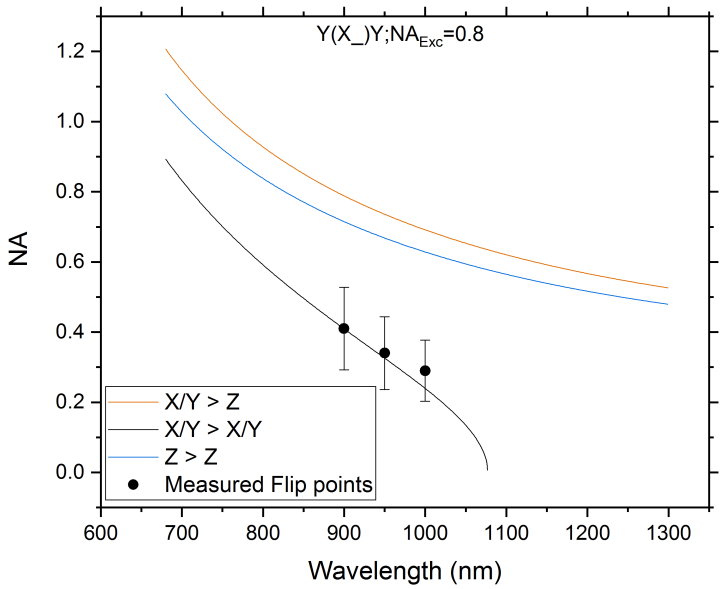

Figure 5.6: Threshold NA values below which the system should no longer collect the signal emitted via CSHG. The curves represent calculated theoretical values using the method described in section 3.1. The data points are the thresholds determined from the discrete derivative of the signal level for the chosen wavelengths.

5.2 Domain walls at the surface

The previous section concerned itself with two obviously different situations in the form of the domain wall in the bulk and the surface of the domain region. It would now be of interest to investigate the region that is essentially the combination of the two, in other words domain walls at the surface of the crystal. As we have seen in Fig. 5.1, we expect the domain wall to show as a bright line on the slightly darker surrounding domain for higher NAs, and eventually switch to appearing as a dark line on the brighter background of the surface. From the previous section we have already obtained an estimate for the threshold NA for our investigated sample, which we can use to focus on the relevant region around the flip point. Additionally, the base behaviour of the system seems to be the same across the wavelengths, such that we can assume it is sufficient to only investigate one of the wavelengths. We will therefore limit the following section to the images recorded at 900 nm with its transition at an NA of ≈ 0.41 for now. Fig. 5.7 shows the XY slices of the sample zoomed in to the surface for numerical apertures ranging from 0.33 to 0.43.

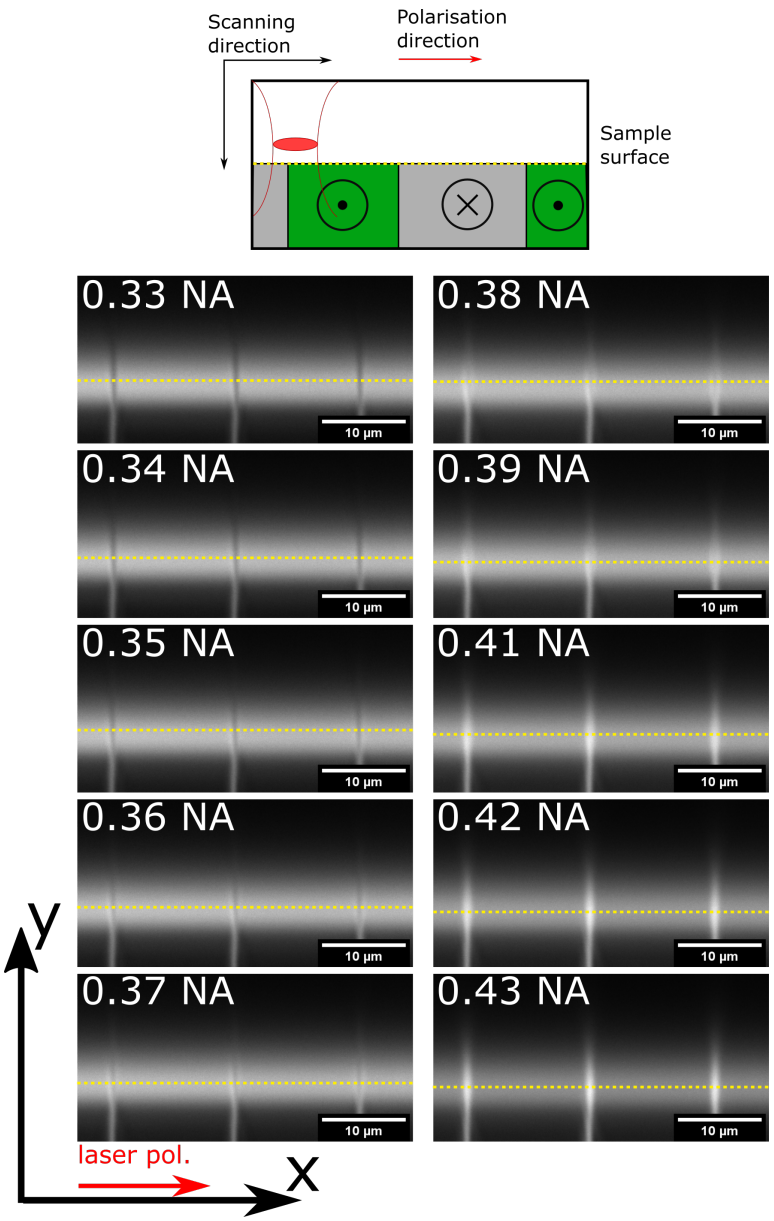

Figure 5.7: XY cross-section of a y-cut cLN crystal polarised by an x-polarised beam incident along the crystal y-axis for a range of wavelengths around the threshold estimated in Fig. 5.6. We do see the transition from a bright line on darker background to a dark line, however, the transition seems to happen later than both expected and calculated in the previous section.

Above the threshold, we clearly see the domain walls as bright lines on the slightly less bright surface domains. However, at the determined treshold NA of 0.41, the walls still show the same behaviour instead of having flipped to the dark contrast. The first signs of a switch do not appear until 0.39 NA, when the domain walls seem to become slightly broader and a dark section appears in the middle. For further lowering of the collection NA, this dark line both lengthens and broadens, while the immediate surrounding area becomes slightly brighter compared to the domain region. At approximately 0.34NA and lower, the domain wall signature at the surface seems to have fully converted to the negative contrast.

While the change in behaviour for the domain walls deep within the material seemed to have been a relatively sudden process, the transition at the surface is instead gradual. Fig. 5.8 presents the line profiles for a select number of numerical apertures shown in Fig. 5.7 in order to gain a closer view.

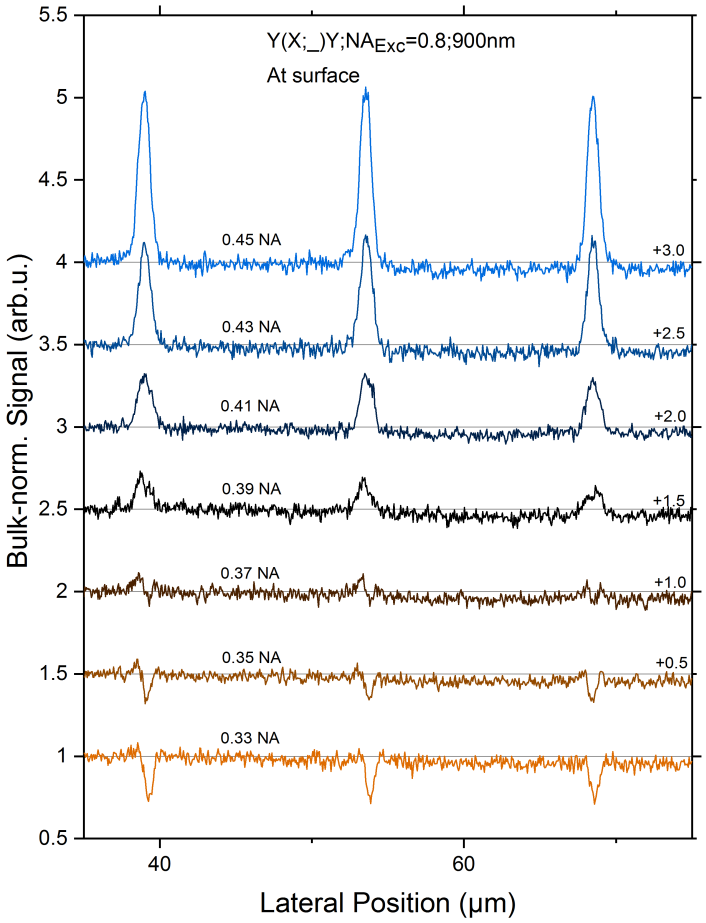

Figure 5.8: Line profiles taken at the surface of a y-cut cLN crystal illuminated by an x-polarised beam incidental along the crystal y-axis. The profiles are normalised and offset to allow comparison. We see that domain walls in profiles above the expected threshold of 0.41 show the behaviour we would expect of bright lines, however this is also true down to 0.39 NA, lower than the threshold. 0.37 NA and lower seem to begin to show the dark line we would have expected, although there is a slight increase in the signal strength in the immediate surroundings. The profile taken using a collection NA of 0.33 NA is the last to show any noticeable signs of this increase that cannot simply be explained by a statistical deviation.

As expected above the threshold NA, the domain walls show as positive peak signatures com-

pared to the domain region. However, this behaviour remains for an NA down to 0.39, lower than the threshold of 0.41. For lower NAs, we see the emergence of the dark line in the centre of the domain wall as well as the slightly brighter strips immediately surrounding it. For numerical apertures below 0.33 we then only see the negative contrast of the domain wall on the domain region.
In order to offer a comparison, the profiles both $5\,\mu$m above the surface as well as $50\,\mu$m within the crystal are plotted in Figs. 5.9 and 5.10. In the former we can observe a similar transition to that in Fig. 5.8, as the obvious positive signatures of the domain wall decrease and subsequently disappear with lower NA. Generally, we observe a noticeable drop in domain wall signal compared to the surrounding domain, as is visible in Fig. 5.10 which is most likely simply owed to the lower collection range (compare Fig. 5.3).

As shown previously, both the surface domain region and the domain walls within the crystal each showed a distinct behaviour. It is possible that the transition in the behaviour of the walls over a larger NA range at the surface is therefore the result of some interplay between the two. At this point we would also have the question of the bright border around the darker domain wall line. An initial thought would be akin to that proposed by Deng et al. [34] in that a certain roughness of the domain wall causes CSHG at a slight angular spread rather than collimated beams as assumed in our calculated model. Due to the difference in acceptance angle between an NA of 0.41 and 0.35 being only $\Delta\alpha_O = \arcsin 0.41 - \arcsin 0.35 \approx 4°$, a sufficiently rough wall could therefore scatter a limited amount of SH light into the objective. However, we would then expect the effect of which to be noticeable in the centre of the domain wall, rather than immediately to either side, which would make a superposition of multiple co-existing mechanisms seem the likeliest explanation.

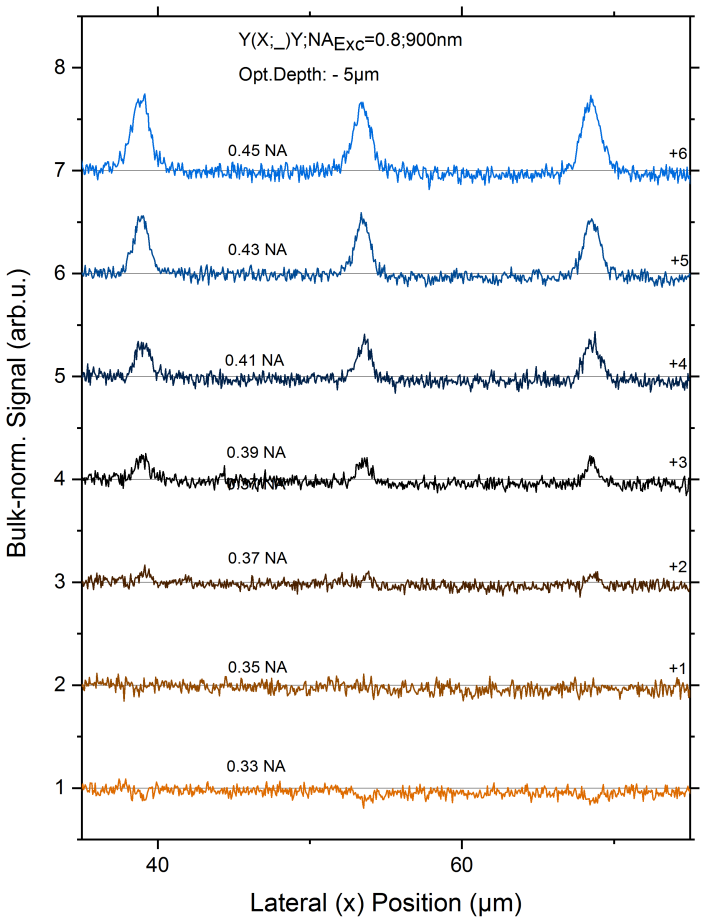

Figure 5.9: Line profiles taken above the surface of a y-cut cLN crystal (sample 1) illuminated by an x-polarised beam incidental along the crystal y-axis. The profiles are normalised and offset to allow comparison. As with the profiles at the surface, higher collection numerical apertures display a more pronounced domain wall signature, which slowly disappears with lower NA.

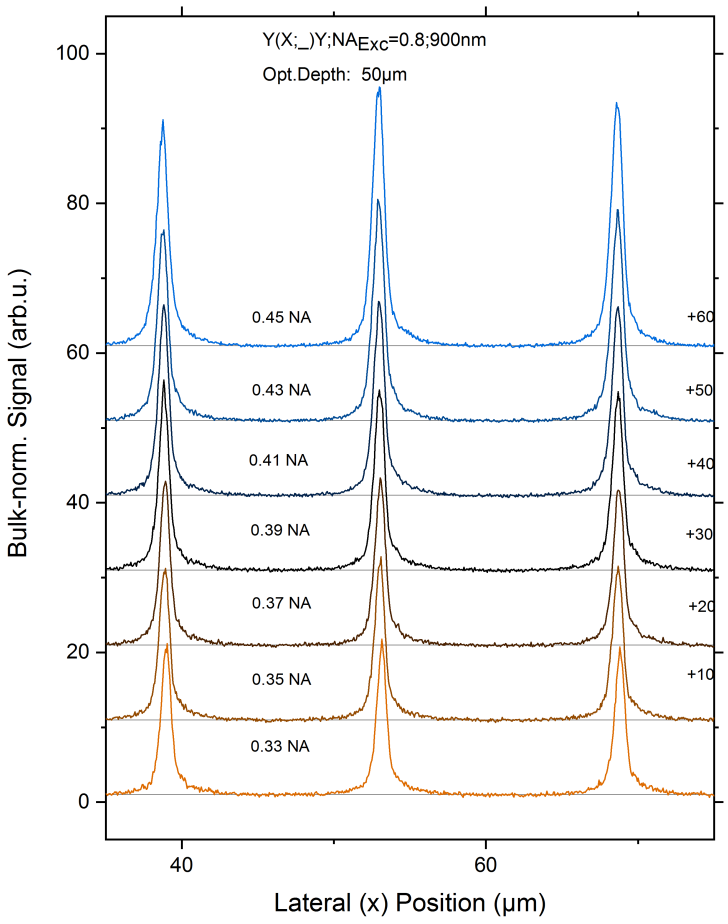

Figure 5.10: Line profiles taken 50 μm below the surface of a y-cut cLN crystal (sample 1) illuminated by an x-polarised beam incidental along the crystal y-axis. The profiles are normalised and offset to allow comparison. There is no significant change in the domain wall signature outside of the decrease in relative strength compared to the surrounding domain signal.

5.3 Blocking via aperture

A secondary method employed as part of this work is the use of an aperture upon the crystal surface to block out certain regions of oblique emission, essentially enacting a filter for a certain range of k-vectors. Any light beam propagating at an angle to the optical axis through the crystal will experience a lateral displacement $dx = \sin\theta * (z - z_r)$, where θ is the angle to the optical axis and $(z - z_r)$ the distance to the rear, or exit, surface of the crystal.
The aperture itself can take the shape of either a bright-field aperture as depicted in Fig. 5.11(a) and (b), or a dark-field aperture as shown in Fig. 5.11(c) and (d). The purpose of each type of aperture is to block SH light that has experienced too large (bright-field) or too small (dark-field) a lateral displacement in order to pass the uncovered section of the crystal. In essence, we can understand the type and dimensions of the aperture as filter criteria for SH emission assisted by k-vectors of the domain wall. Obliquely emitted CSHG emission is assisted by larger k-vectors in order to satisfy non-collinear phase-matching. On the other hand, the SHG characterised by the dipole behaviour as shown in the previous section does not require the assistance of k-vectors, or quasi-momenta, of the domain wall, or will only require relatively small contributions to satisfy its collinear phase-match condition. We can therefore use such an aperture to filter out contributions stemming from certain mechanisms outlined in chapter 2. A bright-field aperture will mainly filter out the CSHG contributions whereas the dark-field aperture will block a large part of the contributions from changes in the nonlinearity and superpositions of phase effects.

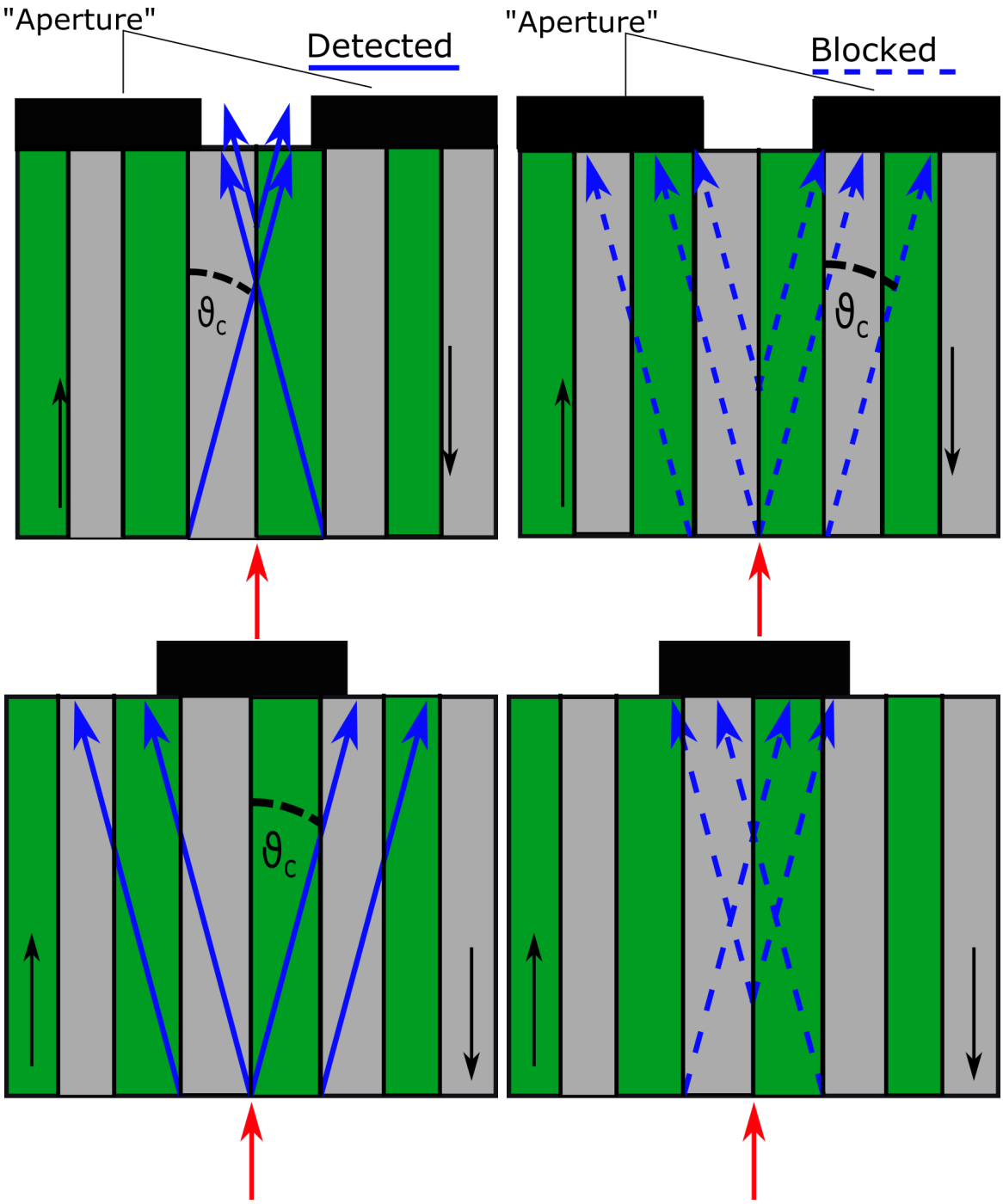

Figure 5.11: Use of an aperture to selectively block CSHG contributions from a given region of the crystal. (a) and (b): Use of a bright-field aperture to block the CSHG emission from directly below the aperture, it will allow the dipole-emitted SH as well as CSHG from regions below the aperture "body" to pass. Solid lines represent the collectable light while dashed lines represent the blocked beams. (c) and (d): Use of dark-field apertures to block the dipole emission directly below the aperture, while CSHG emitted in the central region will pass by the aperture on the rear of the crystal.

This filtering will be most effective directly below the aperture itself, as a lateral displacement can be compensated by a point of generation further away from the centre of the aperture, as can be extrapolated from Fig. 5.11(a). Likewise, the dark-field aperture can block one of the two Cherenkov-emitted beams for domain walls further away from the centre as shown in Fig. 5.11(d). Both types of apertures will therefore have regions in which the obliquely emitted light is fully or partially blocked, or unaffected by the aperture. Fig. 5.12 depicts the crystal segmented into the corresponding regions for both a bright-field and dark-field aperture. Black regions will correspond to a full blocking of the CSHG light, yellow represents a region where one of two emitted beams can pass the aperture and points within the green region can have all their emitted CSHG light collected. For the bright-field image, Fig. 5.12(a), we expect a

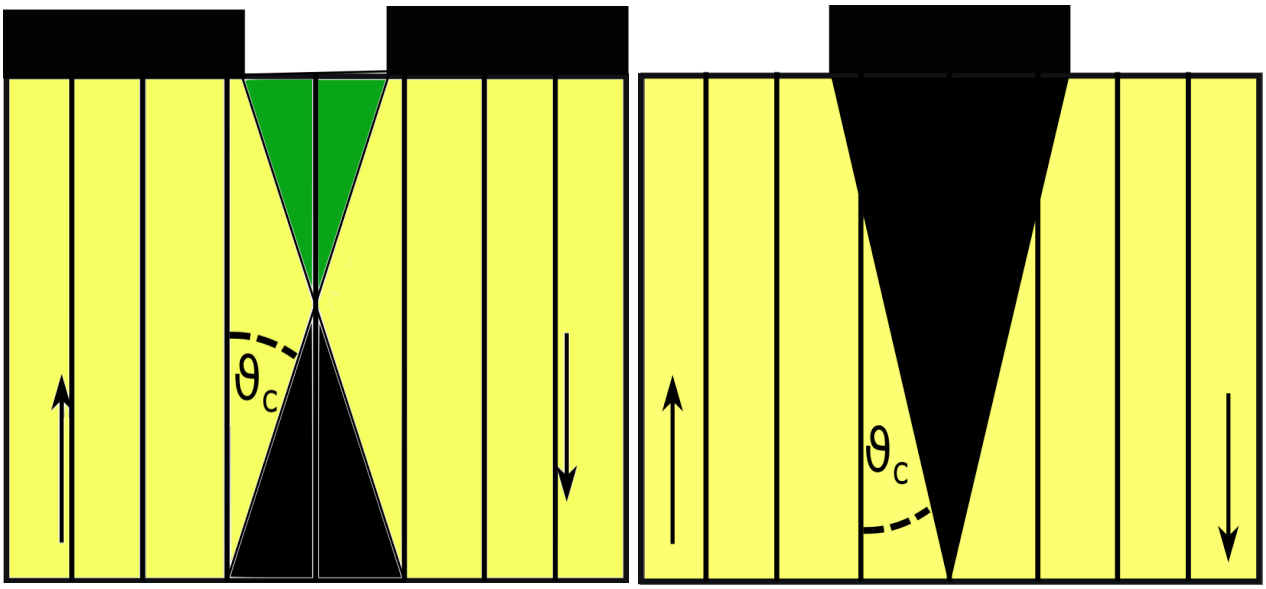

Figure 5.12: Sketch of the pattern of regions expected to form within the crystal for: (a) a bright-field aperture; (b) a dark-field aperture. Black regions emit CSHG that is fully blocked by the body of the aperture, yellow regions are partially blocked (only one of two obliquely emitted beams is collected) and green regions are unaffected. Both types of apertures lead to a triangular pattern of the fully blocked region which will further vary with wavelength. Further away from the centre of the aperture, we expect a partial blocking for both kinds of aperture. However, the bright-field aperture is the only one to have a region from which all signal is expected to be collected.

formation of all three kinds of regions. A isosceles triangular region with its base at the front crystal surface will be fully blocked. The angle of both sides with regards to the optical axis (here the vertical axis) is expected to be equal to the Cherenkov emission angle of the emitted signal. Further away from the centre of the aperture, one of the two generated beams will be able to pass the aperture opening and give a slight contribution from two diagonal strips within the crystal. Close to the aperture itself, the CSHG signal will experience an insufficient lateral displacement and will not be blocked by the aperture body, it will therefore be fully collected. Close to the rear surface, we also expect two more regions from which all signal is

blocked, as for points beneath the body of the aperture the propagation distance to the rear surface is not enough for the lateral displacement to shift the beam into the aperture opening. Using a dark-field aperture, Fig. 5.12 (b), we once again expect an isosceles triangle to form, albeit this time with the tip on the front surface and the base directly "below" the aperture. The majority of the crystal is expected to consist of the yellow region, so only one of the two emitted beams is blocked by the aperture. We expect that the inner angle of the triangle with the vertical axis, in other words half the opening angle, to be equal to the Cherenkov emission angle θ_C.
Based on our knowledge of the dispersion properties of lithium niobate and the confirmation from the previous section that the Cherenkov angle does in fact change with the fundamental wavelength, we can make further assumptions of the behaviour these experiments will show. The change in Cherenkov emission angle was already shown among others in Fig. 5.6. As the emission angle decreases across the board for higher wavelengths, we expect the blocked triangular region to change shape for both apertures. In the case of the bright-field aperture, the smaller emission angle translates into a smaller lateral displacement at the rear surface of the sample, and therefore a smaller region of points from which the CSHG light will be blocked by the aperture. We therefore expect the black triangle in Fig.5.12(a) to decrease in size while the green area grows larger. However, the secondary blocked regions directly beneath the body of the aperture are also expected to become larger. For the dark-field aperture, the lower emission angle and displacement will be insufficient to get past the aperture, causing a larger region of the crystal to show as dark. We therefore expect the triangular area to grow larger with wavelength, and the opening angle of said triangle to decrease.
In addition to the change in behaviour caused by different fundamental wavelengths, we can also predict differences based on the polarisation used, as is visible in the difference of the emission angle based on the fundamental and generated polarisation. For a z-polarised, therefore extraordinary, fundamental beam, we will generate a z-polarised Cherenkov cone with and emission angle larger than both processes caused by an ordinary (x or y-polarised) fundamental. For the bright-field, we do not expect to see much signal, as due to the high angle, the majority of the generated signal will be blocked. On the other hand, we expect the blocked triangle in the dark-field experiment to be comparatively small with a higher opening angle.
For the x-polarised fundamental, we can have one of two processes resulting in either and x-polarised or z-polarised Cherenkov cone, with the latter possessing a noticeably larger opening angle. Based on our observations from the variation of the collection numerical aperture, we would expect the behaviour to be closer to that of the process resulting in the z-polarised SH beam.

Sample images are shown for each kind of aperture in Fig. 5.13 for a fundamental wavelength of 900 nm. As we had expected, each image shows a dark triangular region orientated as shown

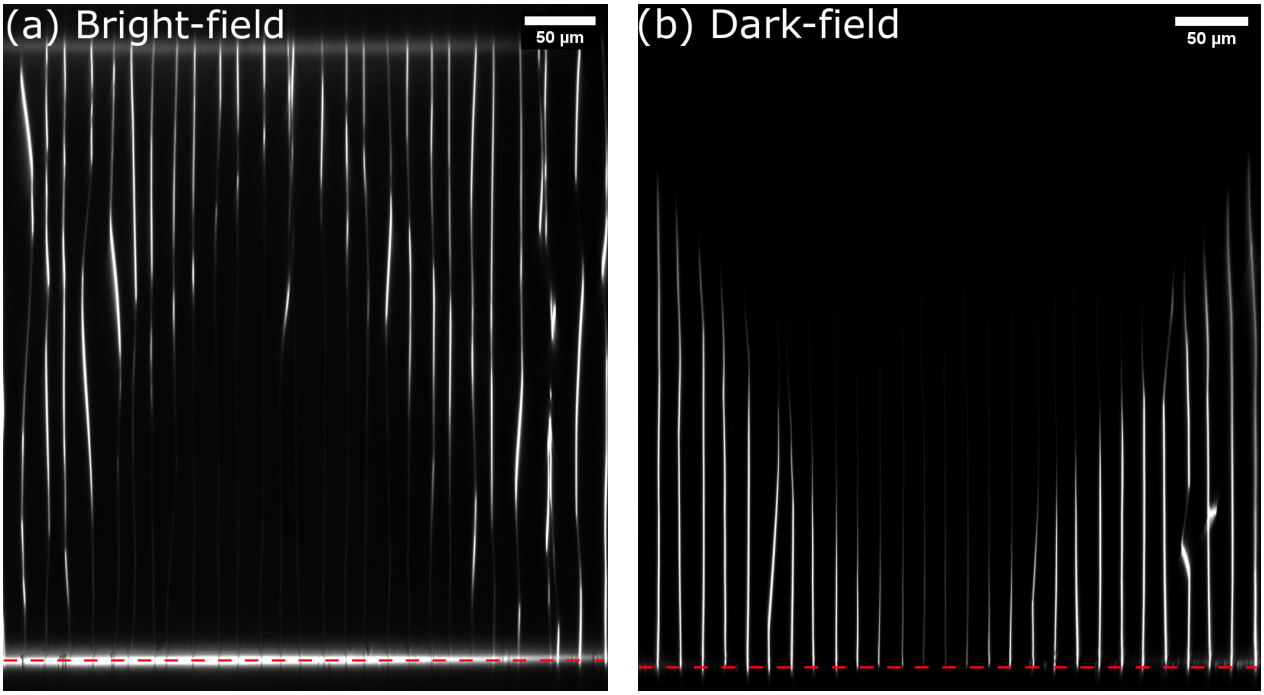

Figure 5.13: XY cross-sections of a y-cut lithium niobate crystal illuminated by an x-polarised fundamental beam. An aperture is placed on the rear surface of the crystal to block out portions of the generated second harmonic light using. (a) bright-field aperture; (b) dark-field aperture. As shown in Fig. 5.12, we see the triangular dark region from which the respective signal is entirely blocked. Although not quite as obvious due to the low density of domain walls, there is also a smaller brighter triangle towards the top of the image.

in Fig. 5.12. We can still identify some domain walls in this dark region however, which could be caused by Rayleigh scattering of previously generated signal. The domain walls become fully visible as very bright lines in both images towards the edges, indicating that a part of the CSHG light is collected. For the bright-field image in Fig. 5.13(a) we can guess at the brighter triangle towards the top of the image, however it is less apparent due to the lower number of domain walls in the region.

The original intent of using an aperture was to filter out specific contributions to the collected second harmonic signal, based on the assisting domain wall k-vectors. This is best verified by focusing on the generated surface signal emitted roughly according to the dipole characteristic, i.e. with no or lower assistance from k-vectors supplied by the domain wall. For the bright-field aperture, we would expect an image similar to that taken with a lower collection numerical aperture, as the CSHG contributions should have been blocked by the foil. Indeed, we see the same surface signal as in f.e. Fig. 5.1, however we now see the domain walls at the surface as dark lines despite using an NA of 0.55. It can therefore be assumed that the domain walls emit mainly according to the CSHG mechanism even at the crystal surface, requiring the k-vectors supplied by the domain wall to appear as bright lines. This is confirmed by Fig. 5.13(b) showing the image recorded using the dark-field aperture, which should block

the signal generated using smaller k-vectors or ignoring them entirely. Here, we see little to no signal generated at the surface and the domain walls are instead visible as very bright lines on a black background. We can therefore already conclude that the use of an aperture, even as basic as the one employed here, constitutes an effective method of blocking select contributions to the signal without sacrificing collection efficiency by lowering the collection numerical aperture. The following sections will then examine the behaviour for the possible polarisations and geometries.

5.3.1 Aperture SHG with a z-polarised fundamental

As outlined in the previous section, the emission angle for a Cherenkov cone generated by a z-polarised beam should be considerably larger than in the case of the 900 nm x-polarised beam used for Fig. 5.13. As such, we expect the triangle to be noticeably larger, possibly even too large to appear for the 1 mm thick sample, as the lateral displacement will increase faster with propagation distance than for lower angles. Additionally, due to the relatively flat slope of the extraordinary-extraordinary curve, a change in wavelength should be far less noticeable than for an x-polarised fundamental. Figs. 5.14 and 5.15 show the XY cross-section recorded while illuminating the sample with a z-polarised beam for a bright-field and dark-field aperture, respectively.

As expected for the bright-field aperture images shown in Fig. 5.14, we struggle to see any signal contribution apart from the surface SHG. Within the depth of the crystal, occasional spots of the domain wall show up slightly brighter which could be due to the kinks in the domain walls causing emission into a slightly different direction which isn't fully blocked by the aperture. As with the x-polarised images in Fig. 5.13, the domain walls show as dark lines at the surface, confirming that the bright lines we usually see are fully caused by CSHG. Comparing the Fig. 5.14(a) and (b), we see little to no difference outside of a few more kinks in the domain wall becoming slightly more visible. This would indicate that the emission angle for a z-polarised fundamental changes as little as predicted for the 100 nm difference in wavelength used here.
The dark-field images are shown in Fig. 5.15. As with the bright-field images, it is difficult to determine whether we see the triangular dark region we would expect from the points blocked by the dark-field aperture. In (b) we can begin to see the hints of a slightly darker region that seems to have an oblique edge, whereas the only change to the signal in (a) is a decrease further into the crystal. However, both images show the same behaviour as Fig. 5.13(b) at the surface as we can observe no obvious surface SHG as expected. Towards the edges of the image, some surface signal is visible but it is heavily distorted, possibly by imperfections at the surface i.e. traces of the saw from the dicing process.

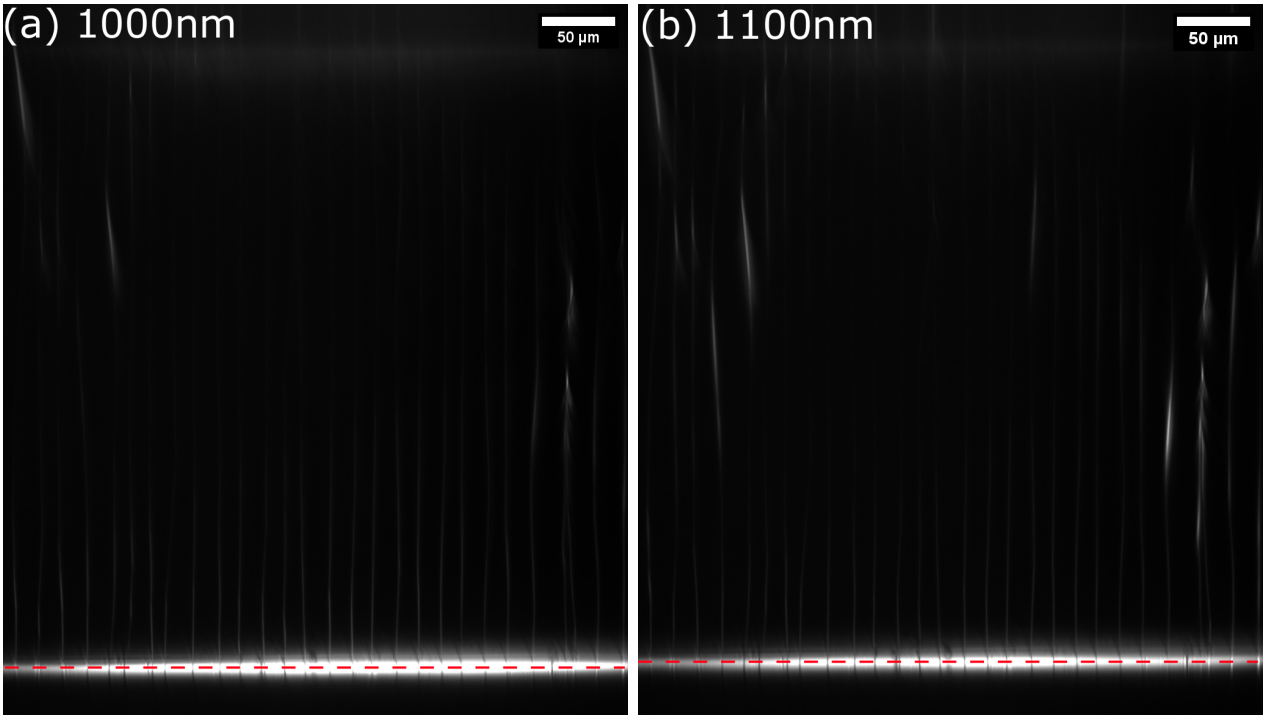

Figure 5.14: XY cross-section of a y-cut lithium niobate crystal recorded using a bright-field aperture and z-polarised fundamental beam at: (a) 1000 nm; (b) 1100 nm. (b) is intended as verification of the lack of visible change when varying the fundamental wavelength. The surface is denoted by the dashed red line. Unlike for the x-polarised images, only the surface SHG is particularly visible, as the only sign of the domain walls are faintly brighter lines which could be the result of Rayleigh scattering. On the surface itself, the domain walls appear as dark lines breaking up the bright level of the surface for both wavelengths.

5.3.2 Aperture SHG with an x-polarised fundamental

We shall now examine the behaviour using each type of aperture for an x-polarised fundamental beam. In this measurement geometry, we expect both to see the regions predicted in Fig. 5.12 as well as an appreciable difference when varying the wavelength. This would be visible as a decrease or increase in the size of the blocked region for a bright-field or dark-field aperture, respectively. Figs. 5.16 and 5.17 will show the images recorded using each aperture type for a number of wavelengths.

The XY cross-section shows the predicted triangular region from which a majority of the signal has been blocked by the aperture. While the blocked region is considerably larger in (a), the size of the region decreases rapidly across the investigated 100 nm range to the point that the region begins to suffer a loss of visibility in (c). As shown in Fig. 5.12(a), we can also see the slightly darker regions along the rear surface of the sample, essentially directly underneath the foil used as an aperture. Below these secondary blocked regions we can begin to see the slightly brighter strips that run parallel to the blocked region's edges. These are the yellow regions in Fig 5.12 from which the beam emitted towards the aperture centre is still capable of leaving

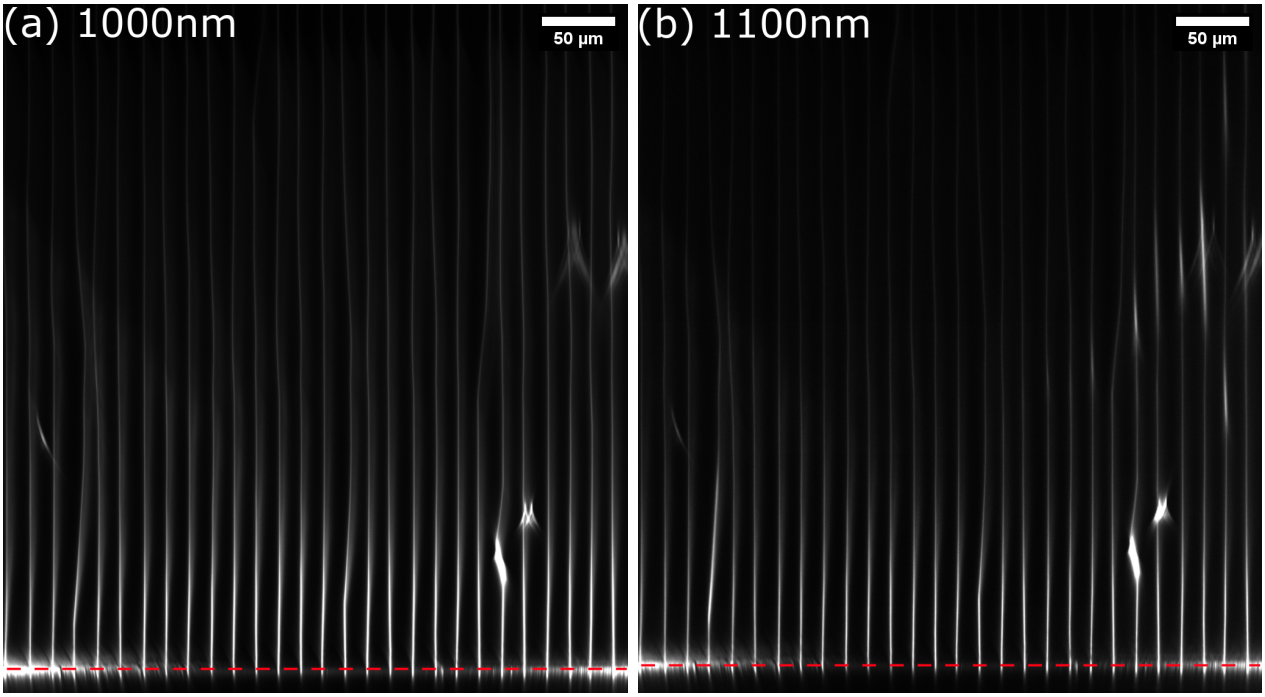

Figure 5.15: XY cross-section of a y-cut lithium niobate crystal recorded using a dark-field aperture and z-polarised fundamental beam at:(a) 1000 nm;(b) 1100 nm. The red dashed line denotes the crystal surface. As with the dark-field image in Fig. 5.13 we can see the lack of surface signal in the centre of the image. Towards the edges of the cross-section we do see some surface signal, but heavily distorted which could be caused by surface abnormalities such as saw tracks from the dicing process. For the lower wavelength in (a) it is hard to discern any sort of change within the crystal in the form of a darker or brighter region outside of the kink in the domain wall in the lower right section. In (b) we can begin to see a region which shows as darker than the rest, however the signal is generally very weak within the bulk.

the crystal without being blocked. Similar to the z-polarised cross-sections, the domain walls appear as dark lines on the bright background of the surface SHG.

Similar to the bright-field images, the dark-field cross-sections show the behaviour as expected in Fig. 5.12. All four wavelengths show an obvious darker region in a triangular shape. However, contrary to the bright-field images, the change in size of this darker region does not seem to be as obvious with the exception of Fig. 5.17(a), as the region does not fully extend to the front surface. Instead of an increase in size, instead it seems as if the triangle shifts downwards with increasing wavelength. As the emission angle in (a) is larger, it would make sense that CSHG emitted close to the front surface propagates far enough through the crystal to experience a sufficiently large lateral shift in order to pass the aperture. A decrease in the Cherenkov angle as we would expect would therefore also result in a broader section of the CSHG generated near the surface being unable to get past the foil aperture.
Qualitatively, the images presented in Figs. 5.16 and 5.17 fulfil our expectations to a large

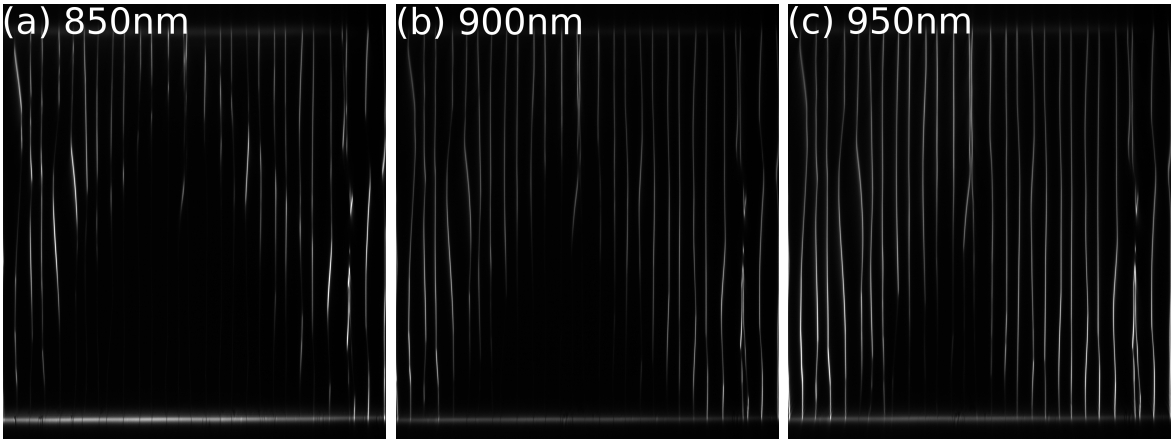

Figure 5.16: XY cross-section of a y-cut lithium niobate crystal recorded using a bright-field aperture and an x-polarised fundamental beam at:(a) 850 nm;(b) 900 nm;(c) 950 nm. As previously shown in Fig. 5.13, the cross-section shows a triangular region which is considerably darker than the surrounding area, with the only domain wall signal assumed to be caused by Rayleigh scattering. Additionally, we see that the blocked region decreases rapidly in size for higher wavelengths which coincides with our expectations, while the brighter triangle towards the rear surface slightly enlarges. Also as expected, the domain walls within the blocked region continue to appear as dark lines at the surface.

extent. The size, in other words width, of the aperture is a deciding factor in the width of the region from which signal is blocked. It is therefore possible that the used aperture size of roughly 400 μm would require a thicker crystal in order to make the differences between fundamental wavelengths more apparent in the size of the triangle. However, the angle of the sides of the triangle should coincide with the predicted Cherenkov emission angle for a given wavelength. The task then is to measure said angle from the images recorded.
It is here that the drawbacks of the simple foil-based aperture become apparent for the bright-field images, limiting the viability thereof to determine the Cherenkov angle. As the bright-field aperture was implemented by attaching theatrical light-shaping foil to the crystal surface using double-sided adhesive tape, it possesses a certain thickness d_a in the range of approximately 200 μm. Our predictions on the formation of darker or brighter regions within the crystal were based on the assumption that any beam that does not directly propagate into the foil would be collected. However, at the rear surface of the crystal, the propagating SH beam experiences refraction away from the optical axis as shown in Fig. 5.18. The aperture in reality is not just an infinitesimally thin surface, we instead have a 3-dimensional structure which can block additional beams which are refracted into the inner edges as shown in the figure.

As a result, the darker region of fully blocked CSHG light will increase in size. This is caused by beams which would exit the crystal from within the aperture opening as presented in Fig. 5.12(a) instead being refracted into the inner edges of the 3-dimensional aperture. Likewise,

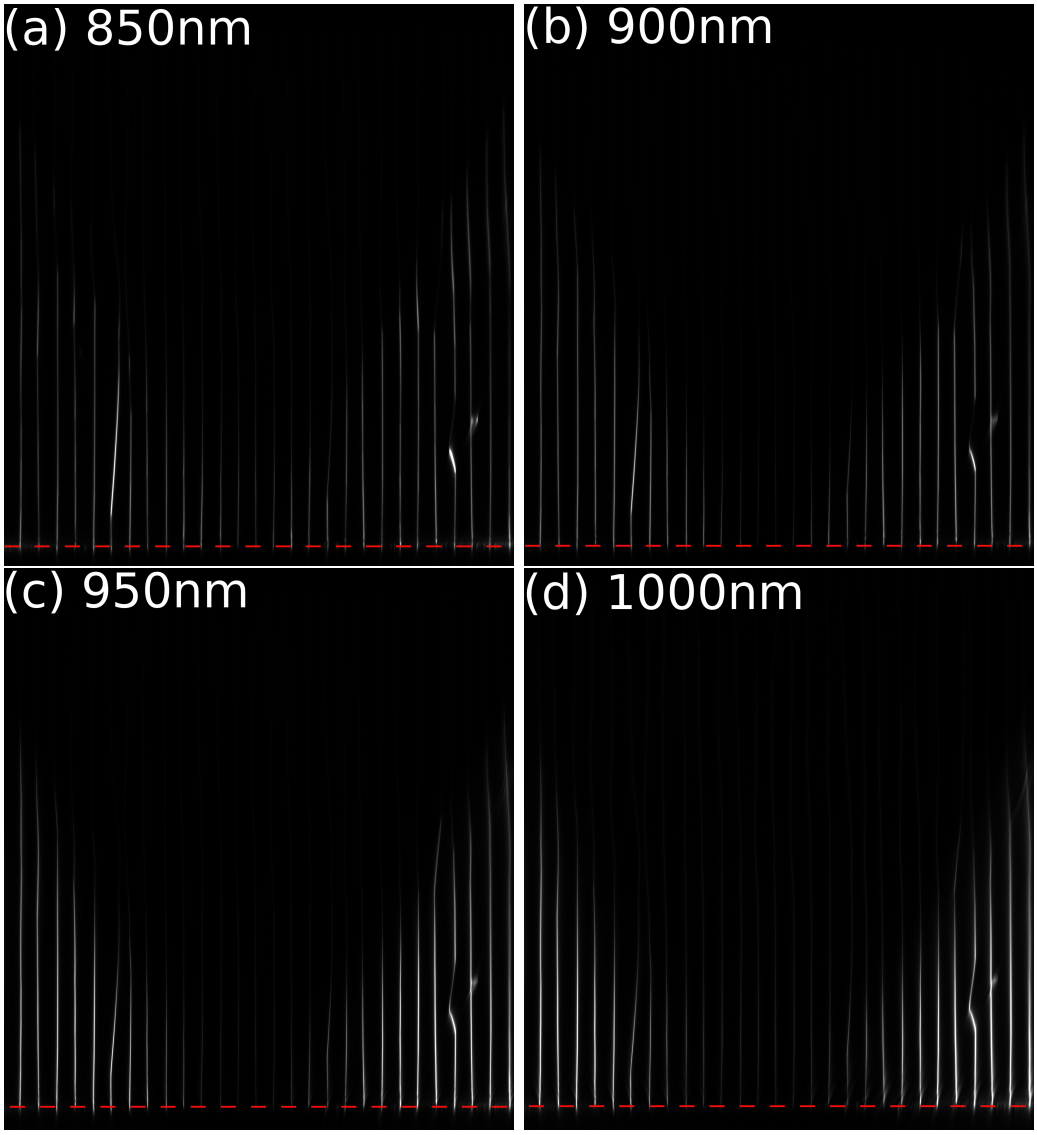

Figure 5.17: XY cross-section of a y-cut lithium niobate crystal recorded using a dark-field aperture and an x-polarised fundamental beam at:(a) 850 nm;(b) 900 nm;(c) 950 nm;(d)1000 nm. All four images show the triangular dark region sketched out in Fig. 5.12(b) while simultaneously showing no noticeable surface SHG contribution. An increase in size of the blocked region is not as obvious as the decrease shown in Fig. 5.16, as while the triangle for the lowest wavelength, 850 nm, is indeed the smallest, there is not as large a difference between the others. Instead, the triangle seems to shift downwards towards the front surface of the crystal, which would also fit with our expectations of a shallower emission angle.

the region which is entirely unaffected by the aperture will become smaller as more beams are refracted into the edges of the aperture. This complicates the process of extracting the cone emission angle from the bright-field images as we have introduced two additional unknown quantities that play an important role in determining which second harmonic beams are filtered out by the aperture. We would now have to compensate both for the thickness of the aperture consisting of the foil and adhesive tape as well as the width of the aperture. Determining

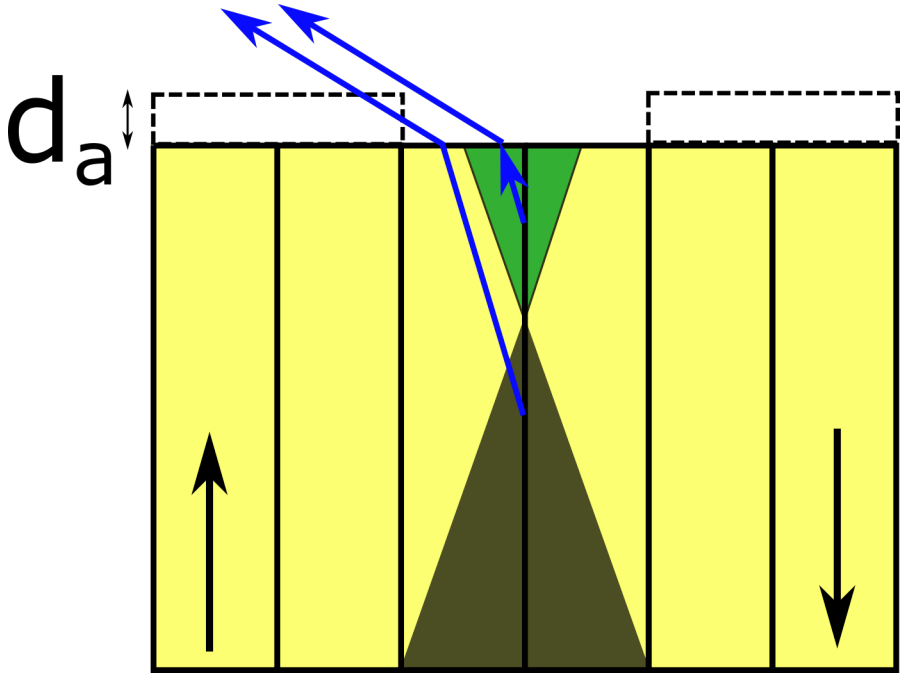

Figure 5.18: Sketch of the real bright-field aperture experiment with the assumption of a certain aperture thickness d_a. As the aperture now extends beyond the rear surface, it can block beams that may have exited the crystal within the aperture opening, but are refracted into the inner edges of said aperture. As a result, the darker region of blocked signal is artificially increased beyond what we would expect from an infenitesimally thin aperture. Likewise, the region which is entirely unblocked will be smaller than expected, as suddenly a portion of the exiting beams are refracted into the sides of the aperture and cannot be collected.

the cone angle using bright-field images could be attempted outside the scope of this work by using a well defined, thin aperture, f.e. metal electrodes evaporated onto the crystal surface. Instead, we will use the dark-field aperture images in the following section to extract the angle of the cone visible in the respective images in Fig. 5.17.

5.3.3 Determining the cone angle

The images recorded using the dark-field aperture are more suitable to determining the cone angle as the effect of refraction at the crystal-air interface will no longer lead to beams being directed into the aperture body. If the beams exit the crystal, they will be collected. As such, we would expect the inclination of the edges of the dark cone in Fig. 5.17 to be equal to the Cherenkov emission angle as depicted in Fig. 5.12.

In order to calculate the inclination angles, we would like to determine the furthest points into the crystal, at which a given domain wall is visible. As the domain wall appears at the point as a bright line, we can assume both emitted CSHG beams have passed the aperture. However, to to kinks or irregularities of the domain walls, not all of the walls seem to possess

a well-defined "end" within the crystal. The method used in this section was to perform a binary binning of the source images by setting a threshold signal level. Points below said level are depicted as black and any pixel above the threshold is shown in white. The result of said thresholding is shown exemplary in Fig. 5.19 for the image recorded at 850 nm with threshold values of 2000, 3000, 5000, and 10000 counts.

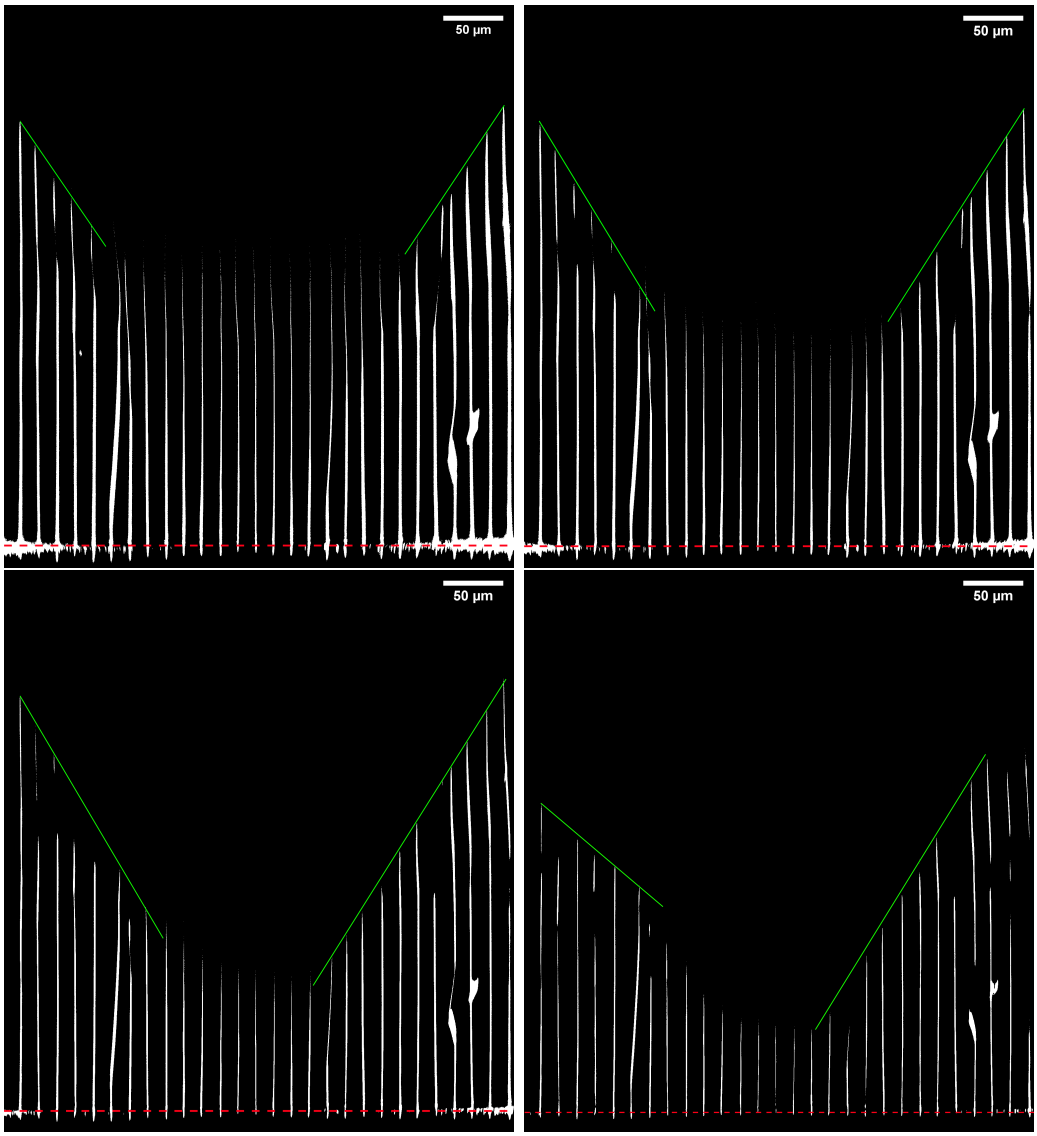

Figure 5.19: XY cross-section shown in Fig. 5.17(a) after applying a binary binning using a threshold number of counts:(a) 2000;(b) 3000;(c) 5000;(d) 10000. By using the thresholding method, we obtain a better defined "end" to the domain wall, i.e. edge of the blocked region. As could be expected, for an increasing threshold the domain walls come to an end earlier within the crystal, especially within the centre of the image. The approximate slope for each side of the blocked region is indicated by the solid green lines, while the crystal surfaces is denoted by the red dashed line.

Using the binary method, the existence of the blocked region becomes even more apparent. For lower threshold values, however, such as those used in (a) and (b) the point of the triangle

appears less visible, as the domain walls are not blocked below the comparatively low threshold levels. Because of this, we have a lower number of points on which to base the slope of the blocked region for low limits such as 2000 and 3000 counts. Compared to this, images (c) and (d) use a threshold of 5000 and 10000 counts, respectively. Here the triangular shape is far more visible and we have a higher number of domain walls along the edge of the region to use as fitting points. Initially, we would have expected the angle to be the same on either side of the image centre, however there seems to be a slightly differing angle on either side. This is not necessarily due to the prediction being false, but instead is most likely caused by irregularities of the domain walls such as kinks or meandering within the crystal along the vertical axis. This is also suggested by the "disappearance" of sections of the domain wall within the region from which we assume all signal is collected. Additionally, the average distance between two neighbouring walls is approximately 15 μm, which we can assume to be a rough estimate in the error of locating the actual edge of the blocked region. As the two sides show differing angles, we will keep the two values separate when compiling the results at the end of this section.
The image coordinates gathered from the images presented in Fig. 5.19 were then used to perform a linear fit independently for every threshold level and side as shown in Fig. 5.20.
The slope m_{lin} of each linear fit was then used to calculate the angle of the region's edge with regards to the vertical axis as:

$$\alpha_O = \arctan \frac{1}{m_{lin}}. \tag{5.7}$$

After calculation, the angles were averaged for each side and are presented in Tab. 5.3 and plotted in Fig. 5.21 alongside the theoretical values dependent on fundamental wavelength. Based on theory and comparison with f.e. Fig. 5.6 we would expect the calculated angles to be close to the behaviour shown by the (O - E)-curve representing an x-polarised fundamental beam and z-polarised SHG signal.

Wavelength [nm]	Left flank angle [◦]	Right flank angle [◦]
850	17.9 ± 1.0	16.01 ± 0.32
900	16.46 ± 0.33	17.27 ± 0.47
950	17.0 ± 0.6	17.88 ± 0.49
1000	15.4 ± 0.6	16.03 ± 1.09

Table 5.3: Inclination angles of the darker blocked region in the dark-field aperture images shown in Fig. 5.17.

As we can see from Fig. 5.21, while the angle of the cone does seem to decrease with higher wavelengths, the actual values do not actually coincide with the curve predicted for an x-polarised fundamental beam and z-polarised SHG signal. We would assume the actual error range to be slightly higher than depicted in the plot, as the irregularities of the domain walls

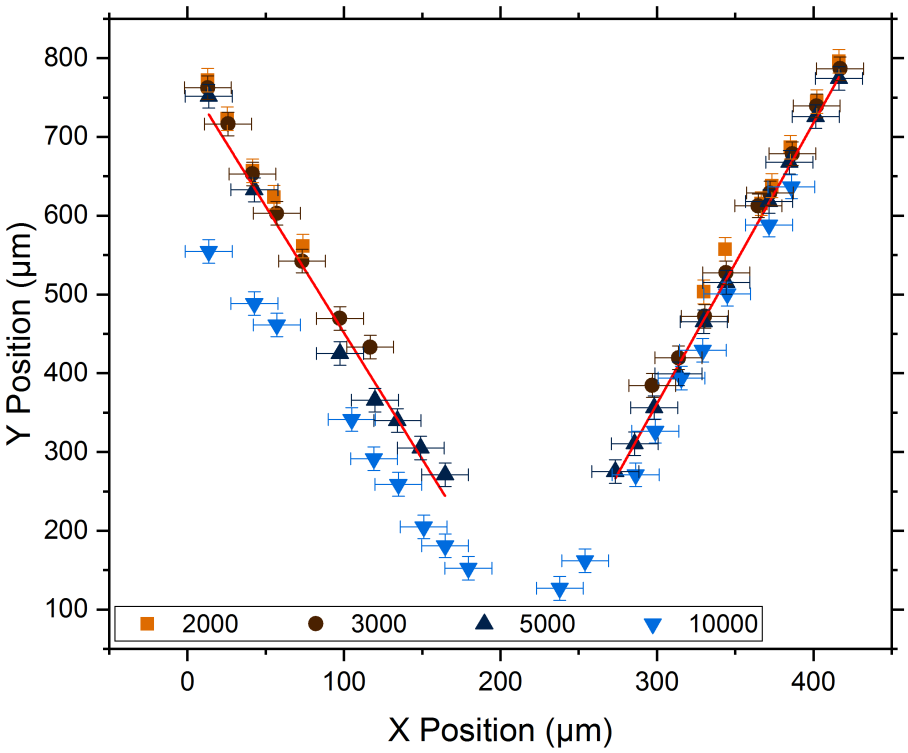

Figure 5.20: Fitting plot based on the coordinates taken from the ends of the domain walls shown in Fig. 5.19 (a) through (b). Each side of the triangular blocked region was fitted separately for each threshold using a linear function. The resulting slope was then further used to calculate the inclination angle of the region and therefore the Cherenkov angle of the emission and subsequently averaged across threshold values for either side. In this figure, the red lines are the linear fits performed for the image with a threshold of 2000 counts.

as well as the comparatively large distance between walls will cause a slightly higher inaccuracy. However, within the present error margins, the trend seems to be towards the dangle decreasing with wavelength. Due to the unpolarised detection used in the LSM980, we can not deny the existence of x-polarised SHG resulting from the CSHG process with certainty. Based on other works, f.e. Amber et al. [23], we would estimate the likelihood as relatively low.

A second possible explanation can be found in our assumptions with regards to the properties of the domain wall and it's role in CSHG. To the extent of our current knowledge, the majority, if not all, work performed on lithium niobate using CSHG ([34], [6]) was performed on a z-cut crystal. As such, we assume that we are the first to show the existence of CSHG for the y-cut geometry and have based our expectations on the findings made by our predecessors. The most important of said assumptions is that the k-vectors supplied by the domain wall in the CSHG process are not polarization or phase sensitive and cover a wide range of values.

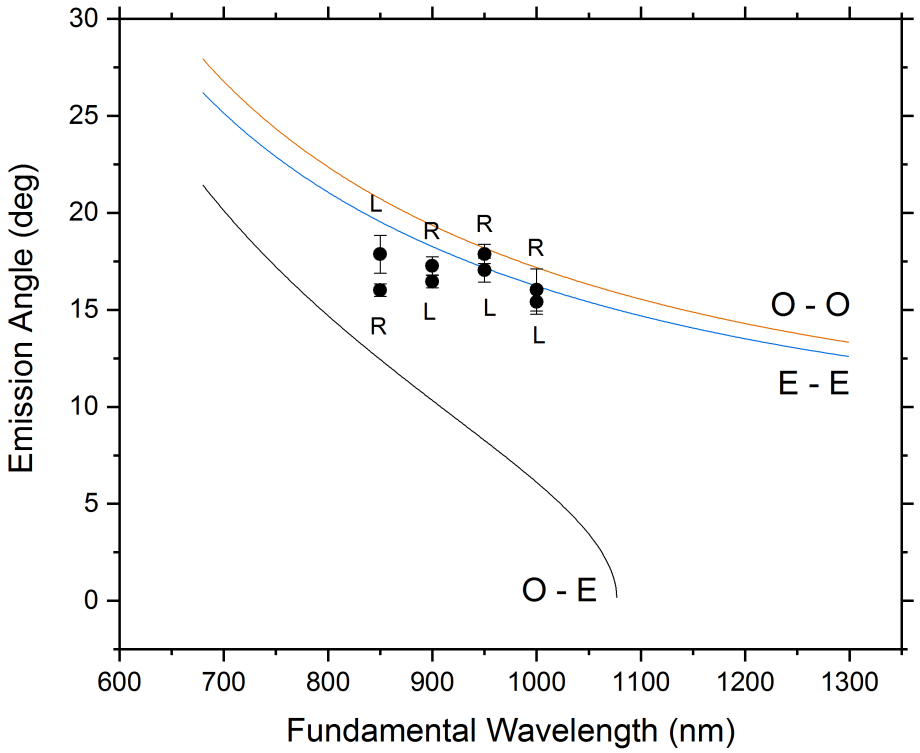

Figure 5.21: Cone angles extracted from the dark-field aperture images recorded using an x-polarised beam for different wavelengths. Due to the at times large difference between the angle of each flank of the blocked region, each side is plotted separately against the theoretical expected behaviour. While the angles do seem to decrease with wavelength as we had expected, the exact values seem closer to the (O - O) curve rather than the angles we would have expected from the (O - E) process.

Instead, it is possible that the domain wall supplies only a well-defined quasi-impulse akin to the effect postulated in Raman spectroscopy as shown by Rüsing et al. [35]. Additionally, the domain wall may have a polarisation "preference", i.e. it increases the effective interaction cross-section of a process which we had assumed to be unlikely, here the generation of an x-polarised SHG signal from an x-polarised fundamental beam.

As mentioned previously, we would have expected the extracted angles to conform to the lowest curve in Fig. 5.21 and a more detailed examination of the behaviour would require a number of additional experiments exceeding the current scope of this Master's thesis.

6 Dispersion switching

6.0.1 Processes involved in anormal dispersion

Before presenting the results of the experiments concerning dispersion switching, we will quickly recap the processes we will be looking at. As the measurement set-up employed for these experiments does not possess a polarisation analyzer, it is important to verify whether this will hinder efforts to detect the switch in dispersion. To do this, we shall examine all possible contributions to the non-linear polarisation in lithium niobate:

$$\begin{aligned}\begin{pmatrix} P_x \\ P_y \\ P_z \end{pmatrix} &= \begin{bmatrix} 0 & 0 & 0 & 0 & d_{15} & d_{16} \\ d_{21} & d_{22} & 0 & d_{24} & 0 & 0 \\ d_{31} & d_{32} & d_{33} & 0 & 0 & 0 \end{bmatrix} \begin{pmatrix} E_x^2(\omega_f) \\ E_y^2(\omega_f) \\ E_z^2(\omega_f) \\ 2E_y(\omega_f)E_z(\omega_f) \\ 2E_x(\omega_f)E_z(\omega_f) \\ 2E_x(\omega_f)E_y(\omega_f) \end{pmatrix} \\ &= \begin{pmatrix} 2d_{15}E_xE_z + 2d_{16}E_xE_y \\ d_{21}E_x^2 + d_{22}E_y^2 + 2d_{24}E_yE_z \\ d_{31}E_x^2 + d_{32}E_y^2 + d_{33}E_z^2 \end{pmatrix}\end{aligned} \tag{6.1}$$

Firstly, as we will be investigating y-cut cLN in a transmissive geometry with a numerical aperture below 0.7, we will be incapable of detecting any y-polarised signal generated. We therefore may assume the second row of the polarisation vector to be 0, i.e. $d_{21} = d_{22} = d_{24} = 0$. Considering our incoming x-polarisation we can then limit the possible polarisation components to the following:

$$\begin{pmatrix} P_x \\ P_y \\ P_z \end{pmatrix} = \begin{pmatrix} 2d_{15}E_xE_z + 2d_{16}E_xE_y \\ 0 \\ d_{31}E_x^2 + d_{32}E_y^2 + d_{33}E_z^2 \end{pmatrix} \tag{6.2}$$

We see that the only term we expect to directly couple to the x-polarised field is the generation of z-polarised light via the $d_{31}E_x^2$-interaction. As Spychala et al. have shown, a strong focusing of an incoming beam is expected to induce other polarisation components [24] (compare Fig. 2.12). However, they estimated that when using a focusing NA of 0.95, only a few percent

of the incident field is converted into an axially-polarised component, y-polarised in this case, with the contribution to the polarisation perpendicular to the incident, z-polarised here, being orders of magnitude lower. As we are using a lower NA of 0.8, those fractions of the incident beam will be even smaller. We can therefore expect the $d_{31}E_x^2$ interaction to be the dominant contribution to the collected signal when using an x-polarised beam.
In theory, this experiment should also be reproducible with an x-cut crystal and a y-polarised beam, generating z-polarised light via $d_{32}E_y^2$. As with the y-cut crystal, there are some contributions that are a result of a mixing of field components due to stronger focusing, such as $d_{21}E_x^2$, which can be neglected. However, at the same time, the E_y^2 field can couple to the d_{22} tensor element. Amber et al. [23] have shown that for an x-cut LN crystal, SHG via $d_{32}E_y^2$ interaction is the dominant process due to the difference in coherent interaction lengths allowing for a more efficient signal generation. We have therefore calculated the interaction lengths l_c using: $l_c = \lambda/[4(n_{2\omega} - n_\omega)]$ and presented them in table 6.1 for 1050 nm and 1110 nm. It is immediately obvious, that with its far longer interaction length for both wavelengths, the generation of z-polarised second harmonic light will be the dominating contribution to any collected signal. It is therefore a valid assumption, that both for an x- and y-cut LN crystal, the measurements will not require a polarisation analyzer to allow us to distinguish the signal components we are interested in.
As a final note, in this chapter we are only interested in the effect a variation of wavelength has on the results of the scans, therefore all profiles are recorded using the 0.55 NA condenser lens unless otherwise specified.

Process	1050 nm	1110 nm
(X/Y → Z)	72.92 μm	57.81 μm
(X/Y → X/Y)	2.80 μm	3.33 μm

Table 6.1: Coherent interaction lengths l_c for possible SHG processes in an x-cut crystal. Calculation was performed for the possible SHG processes assuming an incoming x- or y-polarised beam. In general, the process that switches the polarisation axis from the ordinary y-axis to the extraordinary z-axis will have a longer interaction length.

6.1 Congruent lithium niobate analyzed in the Y(X;_)Y-geometry

As mentioned in the previous paragraphs, we will be limiting our attention to a piece of y-cut cLN with a fundamental beam polarised parallel to the crystal's x-axis. Due to not requiring a polarisation analyzer, and therefore the lack of one, the detected signal will be termed as unpolarised, although as presented in the previous section, we can confidently assume that it will predominantly be z-polarised stemming from the $E_x^2 d_{31}$ process.

So as to avoid gathering redundant data, the investigated wavelengths were limited to a smaller range around the expected switch wavelength of 1078 nm. As any pulsed laser such as the one used in the LSM980 has a certain spectral width when in pulsed operation, it was important to verify that the range was sufficiently large to allow us to be certain that the fringes of the laser pulse were not near the transition.
In order to gain an estimate of the required range, a 100 fs pulse was assumed to have a gaussian spectral profile while being centred at 1080 nm. This delivers a spectral bandwidth of $\Delta\lambda = 17.17$ nm FWHM, which we assume as symmetrical around the centre wavelength. We could therefore assume that the pulse extends roughly 8.58 nm to a side from the centre. Using a sample gaussian peak centred around 0 and with a width of $w = 1$ and maximum amplitude of 1, expressed then by $e^{-x^2/2w}$, the area under the gaussian curve was calculated for a region of varying width around the centre. The resulting area is then expressed as a percentage of the total area beneath the curve.
As the fraction of the curve area outside twice the FWHM is less than 2% we decided that a distance of slightly below twice the FWHM should offer a compromise between sufficient distance from the Switch wavelength as well as a limited but sufficient number of data points. The final limits for the investigation range were therefore established as 1050 nm and 1110 nm as the lower and upper bounds, respectively.

The cLN crystal was scanned at each of these fringe wavelengths initially. As the two wavelengths represent a definitive situation showing normal (1050 nm) and anormal dispersion (1110 nm), we would expect a clear difference in the collected signal due to the Dispersion Switch. The XY-cross-sections of the crystal are presented in Fig. 6.1.
As we can easily see from comparing both images, for 1050 nm the domain walls appear as bright lines on the dark background of the surrounding domain region. However, for the higher wavelength, we the walls are suddenly darker sections on the bright background of the domain. We can therefore already confirm that above the threshold, the dispersion has switched and the bulk domain contributes positively to the signal due to the wave vector mismatch.
The point of interest should now be the transition range, for which we shall show the XZ-cross-section for 1070 nm to 1090 nm. It is important to note that the DW signature is massively increased for the 1070 nm and 1080 nm images. This is due to the coherent interaction length for the SHG process going to infinity for this wavelength range, as it scales inversely with

Region width	% of total Area
FWHM	76.00%
2FWHM	98.12%
3FWHM	99.96%

Table 6.2: The fraction of the total area beneath a gaussian peak described by $e^{-x^2/2w}$ within an interval of a given multiple of the peak FWHM around the centre.

the difference between refractive indices, which are equal at 1078 nm.[17][23] This behaviour is also used for effective non-linear optical frequency converters for the wavelength region around 1080 nm. [25]

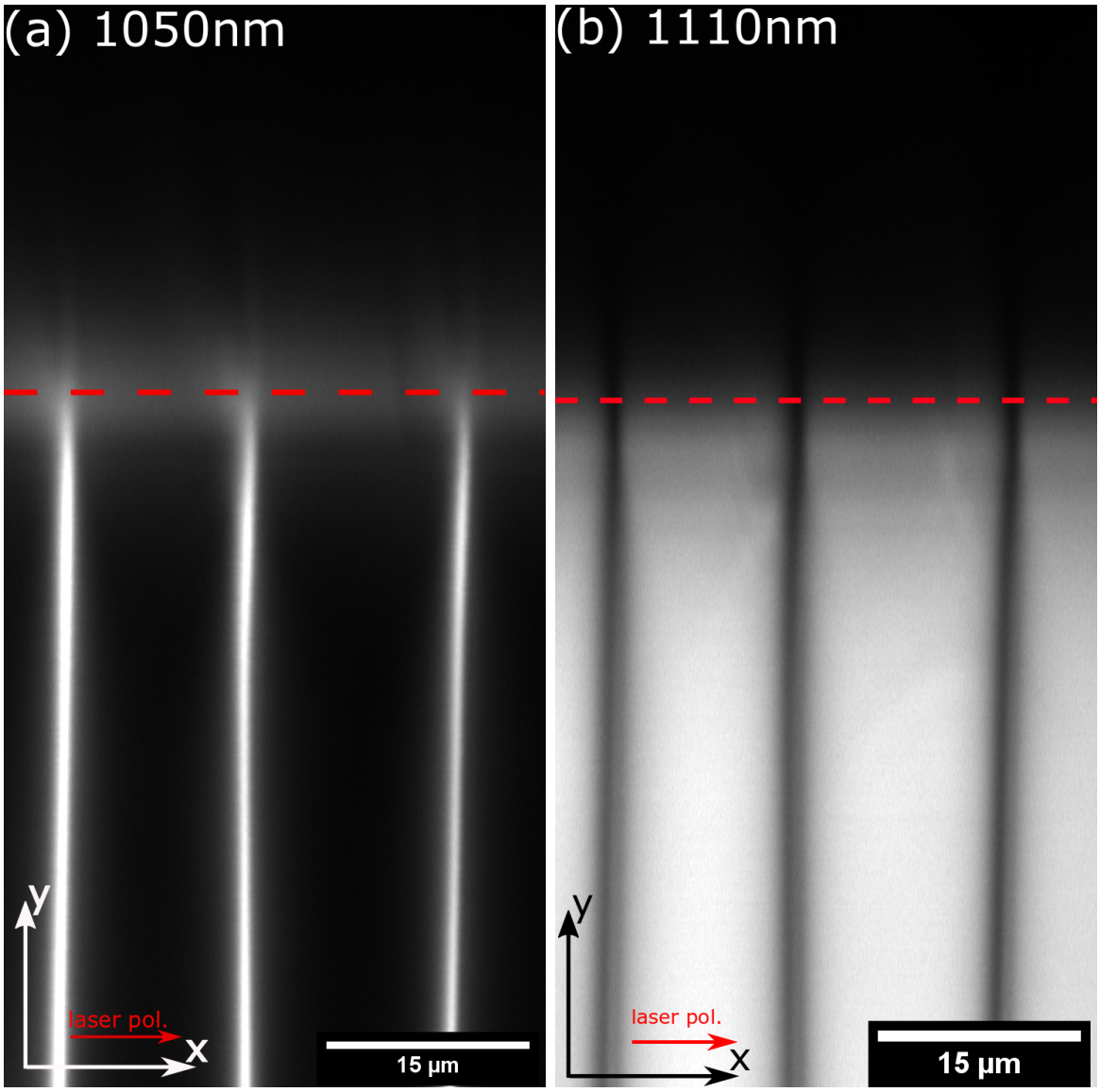

Figure 6.1: YX cross-sections of Y-cut cLN taken at 1050 nm (a) and 1110 nm (b) fundamental wavelength. The wavelengths were chosen as the lower and upper ranges of investigation due to the difference to the transition wavelength estimated at 1078 nm being roughly twice the spectral bandwidth of the fundamental pulse, therefore avoiding an overlap into the transition.

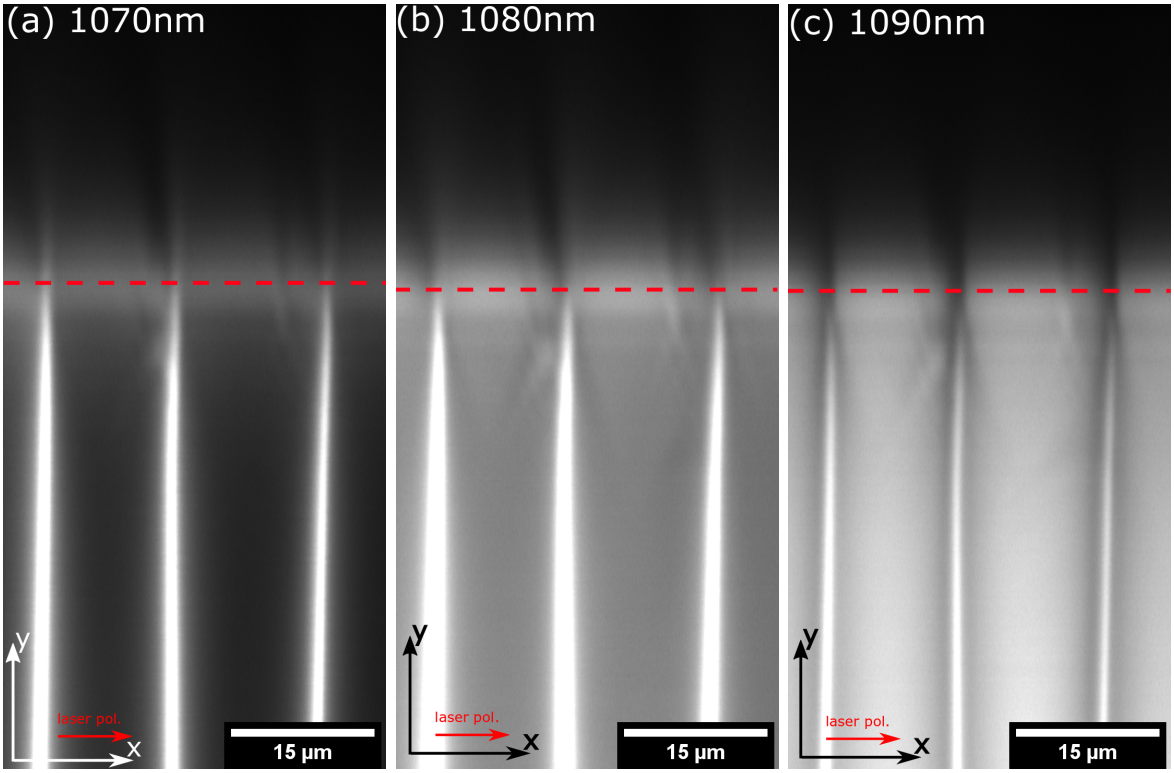

Figure 6.2: XY cross-sections for the cLN sample taken at (from (ab) to (c)) 1070 nm, 1080 nm and 1090 nm. The domain walls for the two lower wavelengths show a massive increase in signal strength due to the highly efficient birefringence phase-matching for LN at 1078 nm, demonstrable via the coherent interaction length which scales with the inverse of the difference in refractive indices for the fundamental and second harmonic, which are calculated as identical for 1078 nm. Instead, the XY-image for 1090 nm is interesting, as this shows the first signs of the dispersion flip, however despite being further away from the switch point, a remainder of the bright DW signature is still visible.

The impact of the considerably larger coherent interaction length for both 1070 nm and 1080 nm causes a spike in the intensity of the detected second harmonic light, causing the domain wall signatures to be fully dominated by this efficient generation. The result of this is that, while we would have expected to see the effect of the Dispersion Switch at least for 1080 nm, we were unable to identify a decrease in the signal near the domain wall. Fig. 6.3 includes the profiles for the Y(X_)Y geometry for the full range of wavelengths investigated. We can clearly see that positive contrast from 1050 nm to 1080 nm, with the overexposures due to higher interaction lengths at 1070 nm and 1080 nm visible in their cut-off peaks.

As the interaction length decreases for an increase in wavelength, we would expect the measurements starting at 1090 nm to show a lower intensity at the peaks, as well as a reduced domain wall signature compared to the surrounding domain. This is indeed visible for 1090 nm in Fig. 6.3, as we notice small drops in the signal level on either side of the domain wall signature. However, there is still a noticeable positive signature present for the same profile, it is assumed that the transition from the normal dispersion image to the anormal dispersion

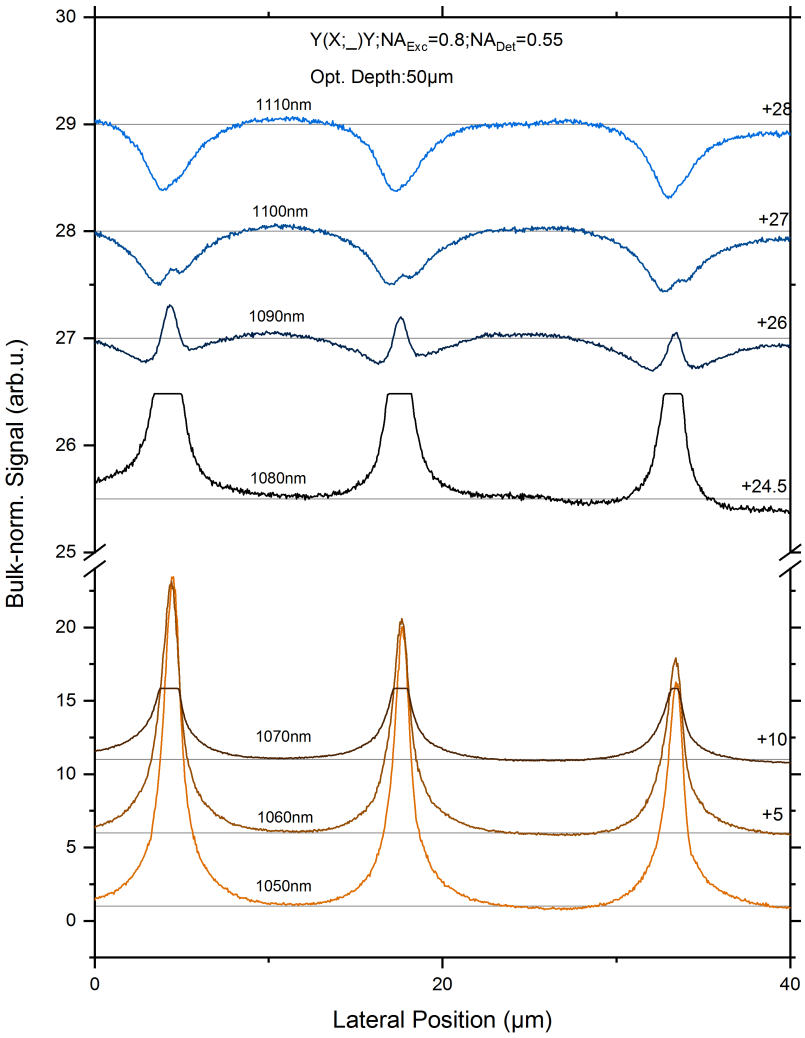

Figure 6.3: Horizontal profiles taken at a reference depth of 50 μm in the Y(X_)Y geometry of cLN at different wavelengths. The profiles were normalised to their bulk domain signal and are offset in order to better compare their shape. The transition from positive to negative contrast appears to happen gradually rather than instantaneous, as the first noticeable signs of a negative contrast are not visible until the profile taken at 1090 nm.

happens gradually. This assumption is given slightly more credit by small positive peaks in the profile for 1100 nm in the middle of the forming negative contrast until we arrive at the fully negative contrast at 1110 nm.

It is interesting to note that, while the domain wall signatures for 1070 nm or 1080 nm cause an overexposure of the detector, the relative difference between the "peaks" and the neighbour-

ing domains decreases with wavelength. As the maximum signal is then essentially constant between the two wavelengths, the difference must be the result of a higher SHG in the bulk domain as was assumed would happen in section 3.2.
As the overexposure distorts the signal around the domain wall signatures and covers a possible drop in intensity due to the Dispersion Switch, we cannot use the 1070 nm or 1080 nm profiles to estimate the effect of CSHG. Instead, we turn to 1090 nm as the candidate on which to base further analysis, as it is the first wavelength to show a noticeable change in the profile shape compared to the previous "tall peaks on low background" of the lower wavelengths.

In order to further investigate this effect, the horizontal profiles were taken in varying depths in increments of 10 μm and presented in Fig. 6.4. As we are beyond the Switch wavelength of 1078 nm, we would expect to see the domain walls appear as a region of lower signal due to the destructive interference between light generated at either side of the wall.

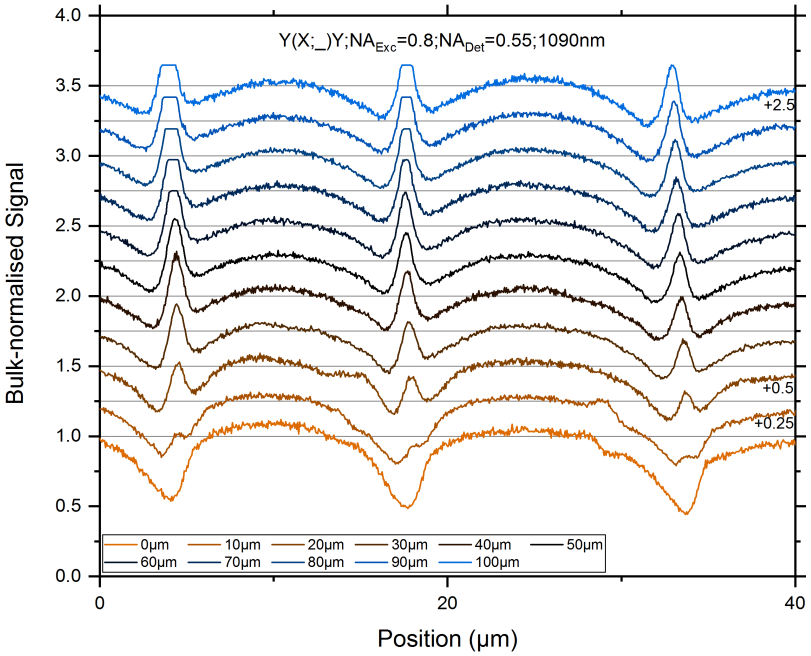

Figure 6.4: Horizontal profiles across the XY cross-section shown in Fig. 6.2 for 1090 nm.[1] The profiles were normalised as explained in section 4.3.1 and plotted with an increasing offset in order to be better able to differentiate each profile. The profile depths range from 0 μm (surface level) to 100 μm below the surface, with a transition from a purely negative contrast of the domain wall shifting into what seems to be a superposition of a positive and negative contribution to the signal.

In the depth-resolved profiles, we see that close to the surface we can observe the domain wall signatures as drops in the surrounding profile. This is as we had initially expected and

indicates that the dispersion has been switched to anormal, causing the negative contrast. However, this becomes far less obvious with increasing depth, as from a depth of approximately 20 μm onward, we once again see a positive signature surrounded by dips in the profile. This positive signature only becomes clearer the deeper into the crystal we look, until it ends in an overexposure for the far depths.

As the positive contribution is closely limited to the domain wall, a first assumption would be that the dispersion itself is anormal in the bulk region as expected, but there may be some portion of the fundamental pulse still below the threshold that is causing CSHG along the domain walls. As shown in the previous chapter, the numerical aperture of the collection objective lens can be used to block the oblique emission of the Cherenkov Second Harmonic signal. Fig. 6.5 therefore shows the profiles taken at 1090 nm but recorded with the condenser lens set to 0.1 NA.

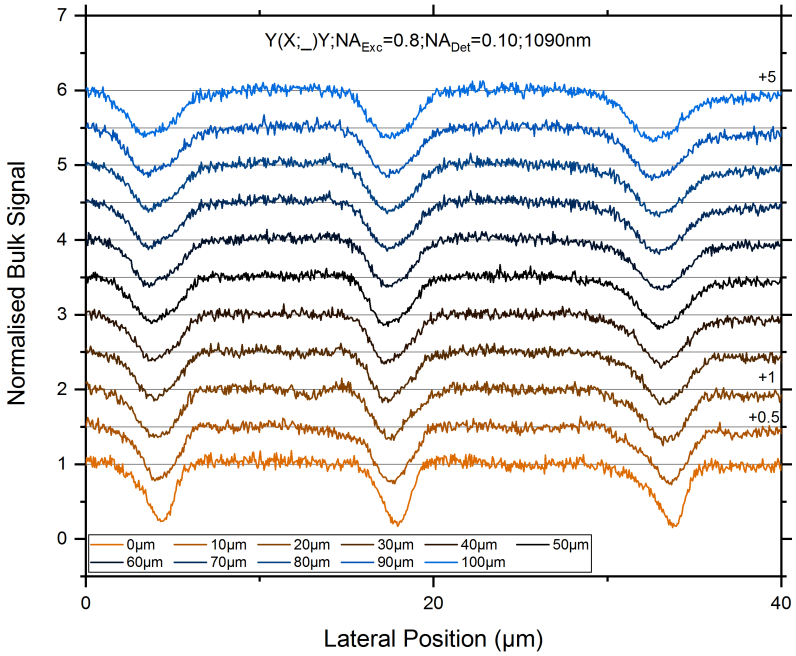

Figure 6.5: Horizontal profiles across the XY cross-section for the Y(X_)Y geometry in cLN, taken at 1090 nm. The superimposed domain wall signatures previously visible for the 0.55 NA measurements are absent for this lower NA recording, suggesting that the cause of the positive signal is indeed CSHG.

Unlike the 0.55 NA measurements, the profiles taken using the smaller NA all lack the superimposed signal present for the same wavelength in the previous figure. This would suggest, that the positive contribution to the domain wall signature does indeed originate from CSHG. The question therefore becomes whether the lower NA will block the positive peak for any

wavelength past the transition range. The results of the scans are plotted in Fig. 6.6.

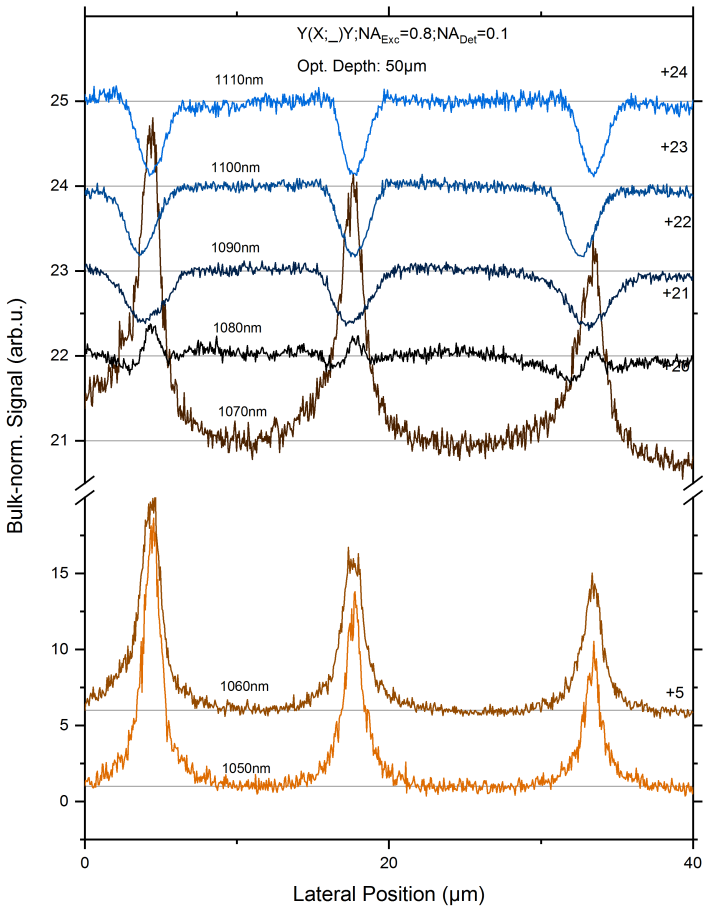

Figure 6.6: Profiles recorded at a reference depth of 50 μm for the Y(X;_)Y geometry in cLN using a collection NA of 0.1. The same features remain as for the 0.55NA profiles, however, as previously shown, the 1090 nm profile possesses an obvious negative contrast to the domain signal. Instead, the superimposed domain wall signature can be seen for 1080 nm.

Fig. 6.6 repeats the behaviour of Fig. 6.3 for the wavelengths at either fringe of the range, as below the transition we have an obvious positive contrast while there is a clearly visible negative contrast for wavelengths far above the switching point. It is interesting to note now, however, that the profile for 1090 nm lacks any sign of the superimposed signature, and instead we see it for 1080 nm, closer to the switch. As the feature repeats, it may make sense to directly compare the profiles for both configurations. This is done in Fig. 6.7.

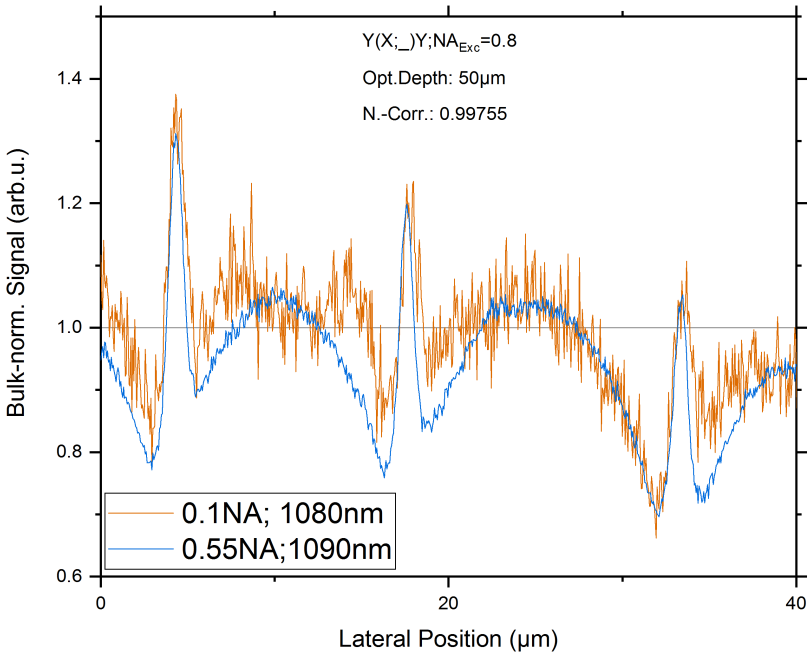

Figure 6.7: Comparison of the superimposed domain wall signature visible at 1090 nm for a collection NA of 0.55 and for 1080 nm for a collection NA of 0.1. Additionally, the normalised correlation value for the two profiles was calculated, showing a very strong similarity at a value of 0.998.

The overlap is surprisingly close, as the 0.1 NA profile only seems to be a slightly noisier version of the profile so the 0.55 NA measurement, both in peak intensity relative to the bulk signal, as well as location of said peaks. We utilised the a signal-procesing method termed normalised correlation which correlates two separate signals and returns values between 0 and 1, where a value of 1 is fully correlated and in our case identical. The correlation value between the two profiles was calculated as 0.998, therefore a very high similarity and it stands to reason that the positive contribution that disturbs the expected negative contrast is more or less independent of wavelength while we still remain within the transition region.

6.2 Y(Z;_)Y - a false geometry

As we have seen in the previous section, it is possible to change the dispersion character of congruent lithium niobate above a threshold wavelength of around 1080nm, with inaccuracies thought to be caused by the broad spectrum of the exciting laser pulses. The important question to then answer, is whether the switch from a positive to a negative contrast as well as the strong signal contribution from the bulk is actually caused by the anormal dispersion of the material when exciting a y-cut sample with a linearly x-polarised beam?

The aforementioned process makes use of the d_{31} tensor element through the process of $d_{31}E_x^2$, inducing a polarisation parallel to the crystal z-axis upon excitation with an x-polarised fundamental. We will now examine the same crystal, only rotating the crystal around the y-axis by 90 degrees, effectively changing our incident polarisation from x to z-polarised. This process now adresses a different tensor element, namely d_{33} in a $d_{33} \times E_z^2$, which will generate a polarisation parallel to z. As we can see from fig. 3.3, this process will never show anormal dispersion, as the refractive index for the z-axis of congruent lithium niobate will always be an increasing function of frequency in the observed wavelength range. As such, an absence of the contrast switch would serve as proof that the change is caused by the transition to anormal dispersion, rather than a general trait of cLN around 1080nm.

Figs. 6.8 (a) and (b) show the XY-cross section of the crystal that was evaluated for 1050 nm and 1110 nm, respectively. We can already see that there is no immediately noticeable change in the cross-section, as such we can readily conclude that there is no contrast switch or therefore a transition to anormal dispersion which would disallow CSHG. However, the images are insufficiently unambiguous to exclude the possibility of any change at all being caused by the difference in fundamental wavelength.
Fig. 6.9 shows the measured profiles for 1050 nm, 1080 nm and 1110 nm. As expected from the images in fig. 6.8, there is no discernible difference in the profiles outside of slight differences in the relative amplitude of the domain wall signatures compared to the neighbouring domain regions, which can be simply caused by a slightly different sensitivity of the detector to the specific detection wavelength. We can therefore confidently claim that the contrast switching observed in the previous section is in fact caused by the change from normal to anormal dispersion and the elimination of CSHG from the interaction.

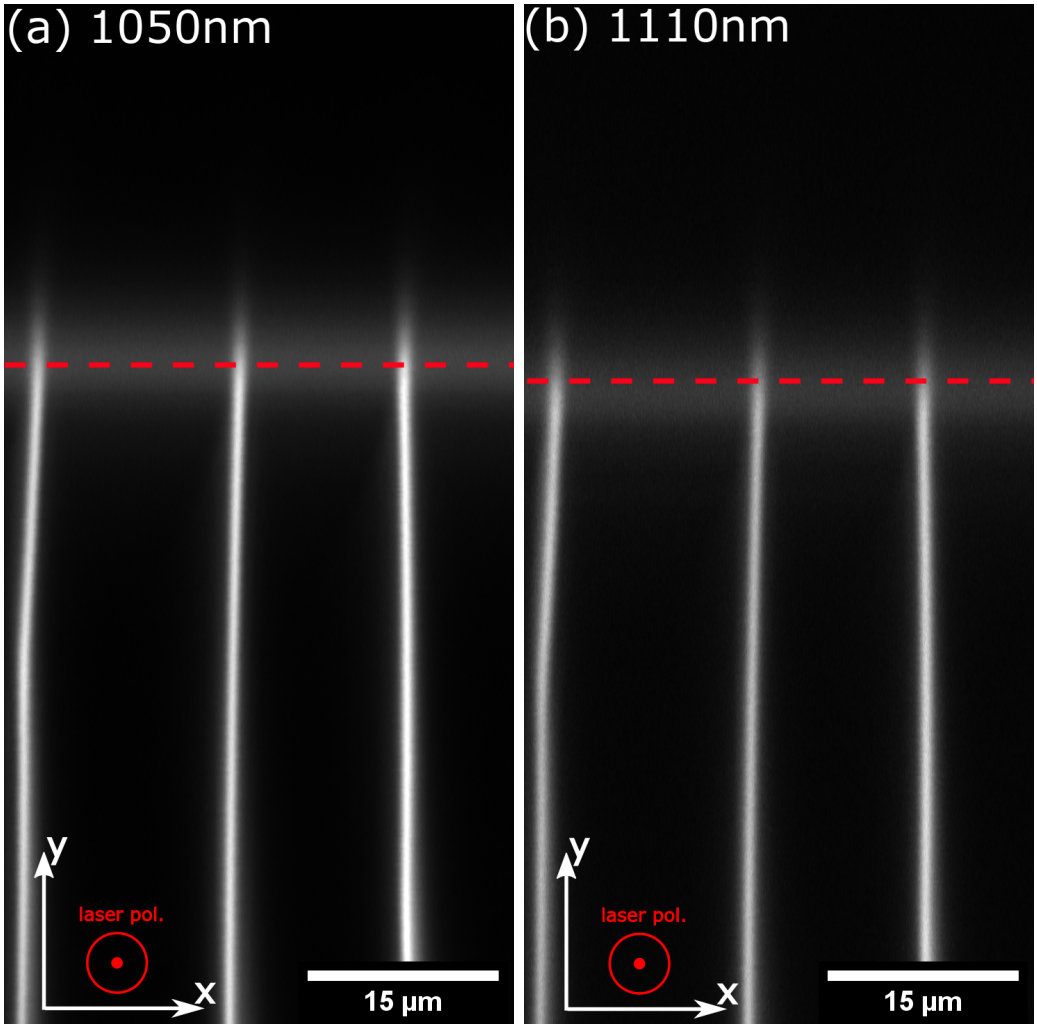

Figure 6.8: XY-cross-section of the evaluated spot in the crystal for the Y(Z;_)Y geometry using a fundamental wavelength of (left) 1050 nm and (right) 1110 nm. The determined surface location is marked by a thin white line. It is immediately visible that, unlike for the case of Y(X;_)Y, there is no discernible contrast flip, the domain wall signatures remain as bright lines regardless of wavelength. As such, we can rule out the effect as being a general property of congruent lithium niobate.

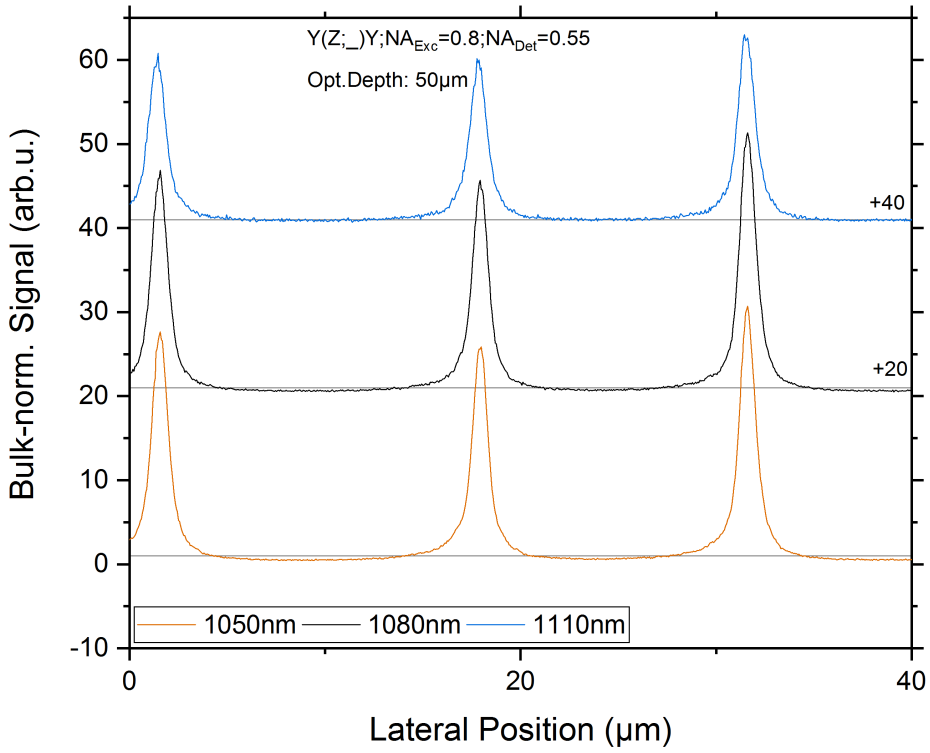

Figure 6.9: Line profiles across domain walls in a Y(Z_)Y geometry at an optical depth of 50 μm. As expected from fig. 6.8, we see no discernible change for a shift in fundamental wavelength outside of possible amplitude changes due to a possibly different detector sensitivity.

6.3 Congruent lithium niobate - the magic crystal

In the previous sections, we have shown that congruent lithium niobate both allows us to geometrically block the detection of second harmonic light emitted via CSHG, as well as prohibit the process in the first place. As shown in the last section, the switch in dispersion is not a general effect of the material, but is in fact limited to the Y(X;_)Y geometry. A further point of interest would be to investigate, whether this behaviour is due to the congruent composition of the crystal, or if other stochiometric variants of the material exhibit the same traits.

6.3.1 Theoretical calculations

The calculations performed for congruent LNO in chapter 3 were repeated using the Sellmeyer equations for both stochiometric LNO (sLN) and 5%-MgO-doped LNO (Mg:LN), as taken from the same book by Wong et al. [36]. The results for both the geometric blocking threshold as well as the dispersion switch wavelength are presented below in figs. 6.10 and 6.11 for each material.

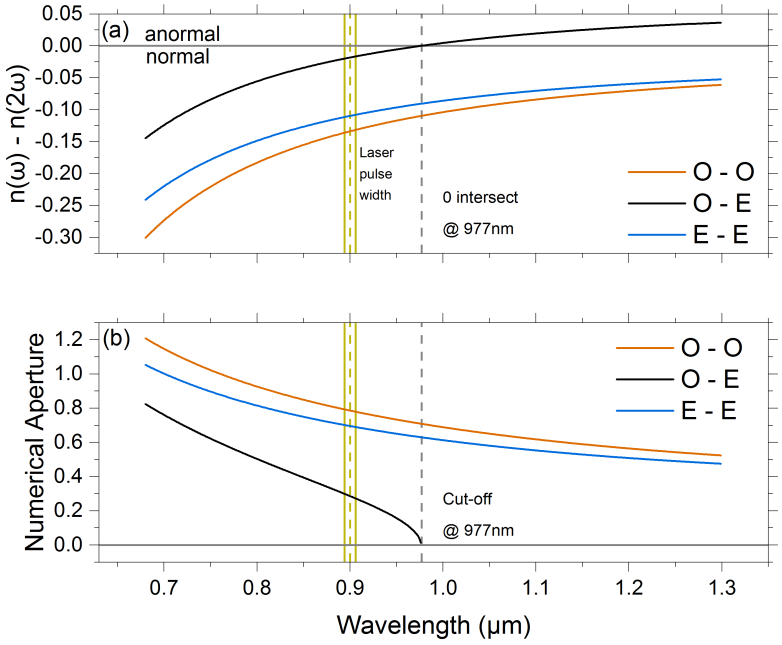

Figure 6.10: Theoretical predictions for stochiometric lithium niobate (sLN). Basis for the calculations were the Sellmeyer equations listed in [36]. (a): Difference between the refractive indices at the fundamental and second harmonic wavelength. (b): Threshold collection NA to be able to detect CSHG signal contributions.

As can be seen from both fig. 6.10 and fig. 6.11, we expect the same behaviour to occur for

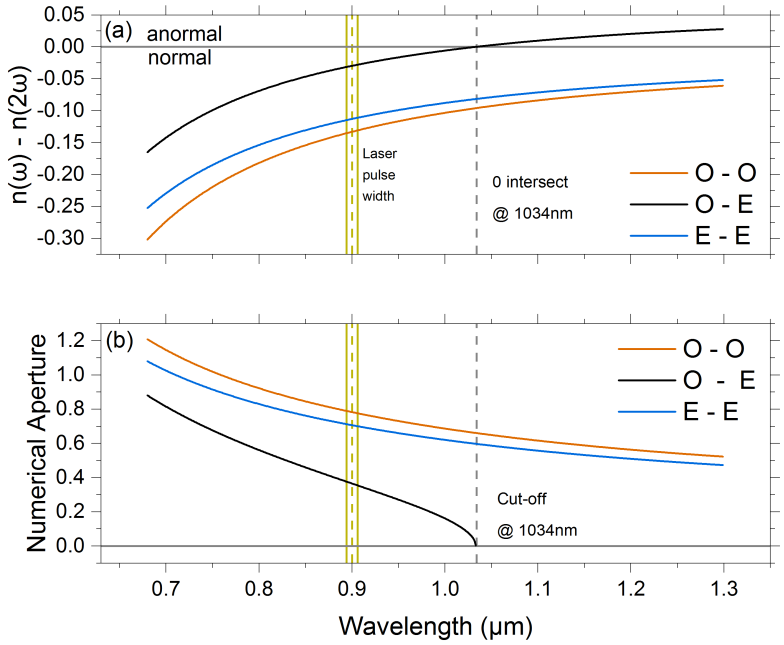

Figure 6.11: Theoretical predictions for magnesium-oxide-doped lithium niobate (MgO:LN). Basis for the calculations were the Sellmeyer equations listed in [36]. (a): Difference between the refractive indices at the fundamental and second harmonic wavelength. (b): Threshold collection NA to be able to detect CSHG signal contributions.

both SLN and Mg:LN, albeit with the cut-off, or flip, wavelengths differing from that of CLN. Whereas the threshold wavelength for CLN was 1078 nm, both alternative variants see the change in behaviour, occurring at 977 nm for SLN and 1034 nm for Mg:LN.

6.3.2 Images for MgO:LN

Due to sample availability, we will use MgO-doped lithium niobate to confirm that the dispersion switch is an inherent property of lithium niobate in general and not specific to congruent LN. We would also like to confirm that the wavelength at which the dispersion switches to anormal is at the predicted 1034 nm. As the wavelength at which we begin to see the effect of the dispersion switch is slightly above the theoretical threshold wavelength for cLN, we would also expect the threshold to lay slightly above 1034 nm. As we wish only to use the MgO:LN as an additional verification of the behaviour, we will limit the examination to the Y(X;_)Y geometry and skip straight to comparing the line profiles at a depth of 50 μm within the crystal in Fig. 6.12.

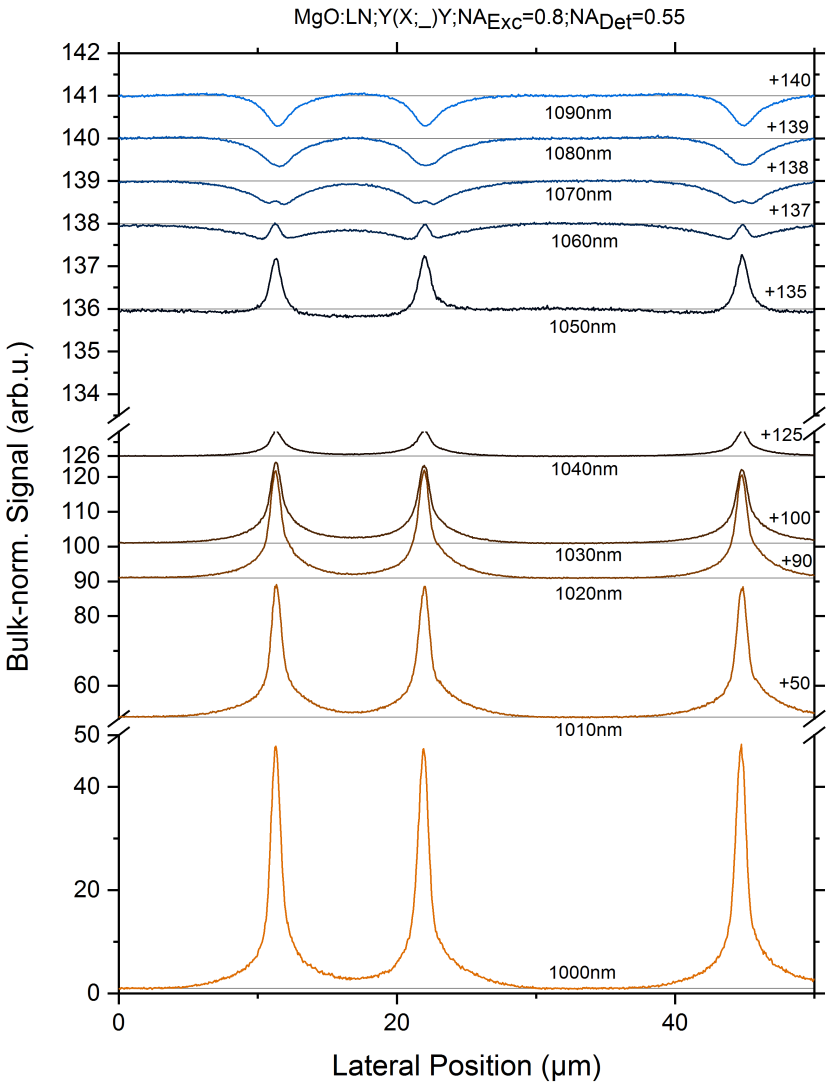

Figure 6.12: Line profiles recorded from a y-cut crystal of MgO-doped lithium niobate illuminated by an x-polarised fundamental beam of different wavelengths. The profiles were extracted from a depth of 50 μm within the crystal. As with the congruent lithium niobate crystal, we see the domain wall signatures as positive peaks on the background of the surrounding domain signal for wavelengths below the predicted flip-point of 1034 nm. Likewise, the profiles of the two wavelengths bracketing the expected threshold wavelengths show a massively increased signal generated at the domain wall, enough to overexpose the detector. However, the first signs of the dispersion switch are not apparent until the 1060 nm profile which displays the stacked signature we saw at 1090 nm in the cLN measurements. The domain wall signature then continues to transition to the expected negative contrast for higher wavelengths, confirming that the dispersion switch is not limited to only congruent lithium niobate.

For lower wavelengths removed from the switch-point, the line profiles appear as we are used to with the domain wall signatures as positive peaks on the lower domain signal background. The comparative strength of the domain wall signature compared to the surrounding domain then decreases for higher wavelengths. As with the congruent lithium niobate sample, the profiles recorded at the wavelengths which bracket the threshold wavelength, namely 1030 nm and 1040 nm, both show an overexposure at the domain walls due to the highly efficient SHG caused by the far larger coherent interaction length near 1034 nm. However, unlike the cLN profiles, the first wavelength at which we see the same dips in signal around the domain wall signatures is not until 1060 nm, later than expected. Both 1060 nm and 1070 nm show the stacked domain wall signature we observed at 1090 nm for congruent lithium niobate, which then disappears for the higher wavelengths and transitions into the fully negative contrast we would have expected. We can conclude that the switch of the dispersion from normal to anormal behaviour is an intrinsic property of lithium niobate, regardless of stochiometry or doping. The variation of fundamental wavelength can therefore be used as a tool to selectively disallow the generation of second harmonic signal according to the CSHG process in lithium niobate, allowing one to examine the sample's behaviour based on both phase arguments and changes to the local nonlinearity.

6.3.3 Dispersion effects in back reflection

As a majority of SHG-based investigations into lithium niobate in literature is performed in a reflective geometry, the question could arise whether a variation of the fundamental wavelength could also be applied to said experiments in order to change the collected signal. Recalling the phase-matching arguments that formed the basis for the hypothesis in the transmission, or forward, geometry, the switch of the dispersion would require a wave-vector mismatch that is larger than 0. However, in a back-scattered experiment, the mismatch will always be smaller than 0, anormal dispersion should therefore not be possible. We would therefore also expect to observe the domain walls as bright lines on a darker background, as CSHG should in theory be possible for any wavelength when detecting the reflected signal.
As shown by f.e. Amber et al. [23], the coherent interaction length during SHG is considerably larger in the forward direction than in the backwards direction. For this reason, the forward-emitted signal in the transmissive geometry is expected to be considerably stronger than the backward-emitted second harmonic light. The signal detected could then possibly simply be the forward signal reflected at the rear surface of the crystal. Fig. 6.13 depicts the profiles recorded in the Y(X;_)-Y reflected geometry for various wavelengths, extracted from a depth of 50 μm within the crystal.

As with the profiles generated in the Y(X;_)Y geometry, the domain wall signatures are positive peaks on the surrounding domain signal below the threshold wavelength of 1078 nm. The comparative height decreases with wavelength until they are overtaken by signal originating from the domain regions. However, we are still capable of observing signs of the positive peaks well past the threshold at 1110 nm, despite the evident emission of signal from the domain. This signal within the crystal disagrees with the assumption that the reverse direction should always have a negative wave-vector mismatch Δk, and therefore not emit SHG light. As stated previously, it is very likely that the source of SHG in the position of the domains is in fact caused by the forward-emitted light reflected at the rear surface of the crystal.
In order to verify the validity of this explanation, the experiment was repeated on the same sample under differing circumstances. Initially the XY cross-section was recorded as was done for Fig. 6.13 to obtain a reference profile. A second measurement was taken placing an aluminium mirror behind the sample to increase the amount of forward-emitted signal reflected back into the excitation and collection objective lens. Finally, a third measurement was performed with the sample submerged in a few drops of water. Due to the lower difference in refractive index between lithium niobate and water (compared to the difference between LN and air), the reflectance at the rear surface should be noticeably lower and the backward-emitted signal should become more evident in the profiles. To summarise, we would expect the profile recorded with the mirror placed behind the sample to be essentially identical to the forward-emitted profiles in Fig. 6.3 for higher wavelengths. On the other hand, we ex-

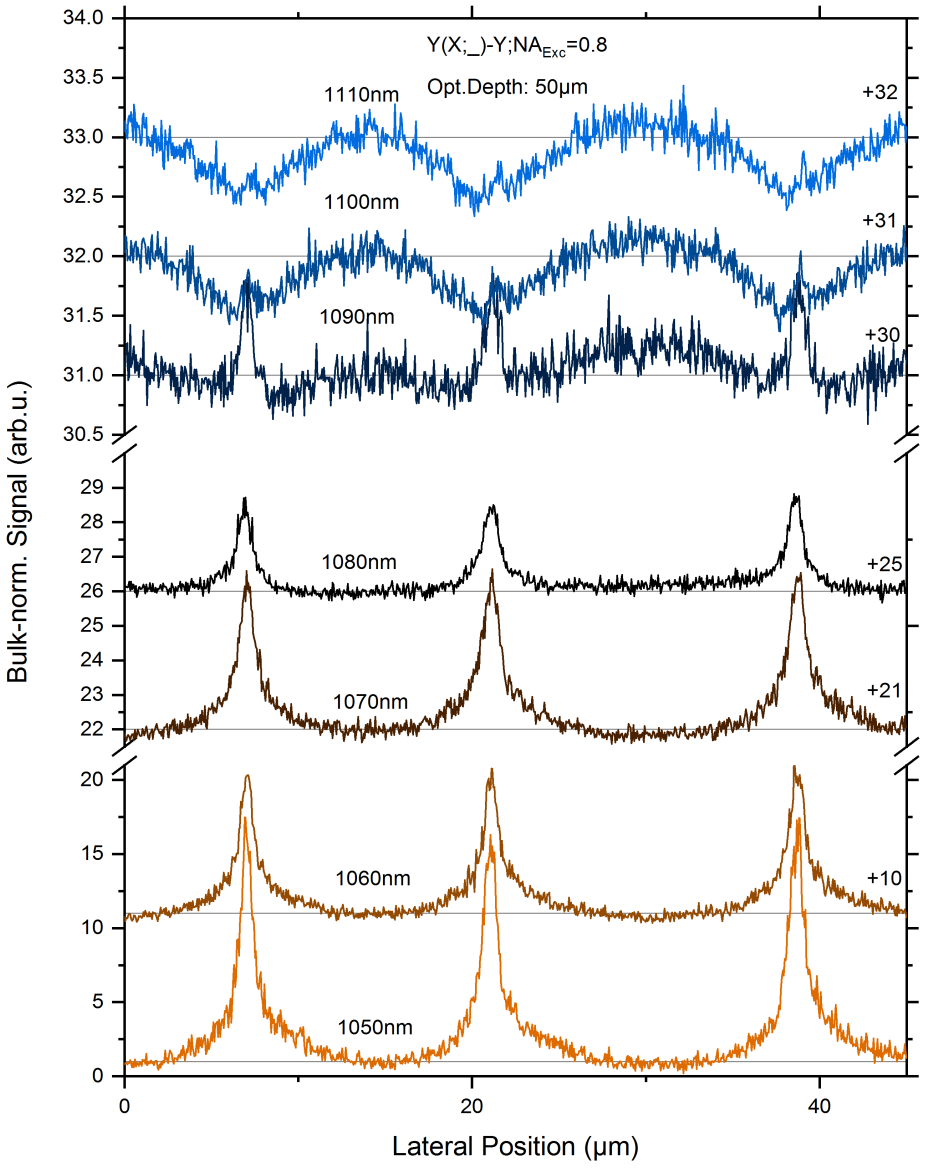

Figure 6.13: Line profiles recorded in a reflective geometry of a congruent lithium niobate crystal illuminated by an x-polarised fundamental beam. As with the forward-emitted signal, the domain wall signatures are positive peaks on the domain signal which is comparatively lower. For an increase in wavelength, the peaks become less pronounced and are eventually overtaken by the domain signal above 1100 nm. However, unlike in the transmission profiles shown in Fig. 6.3, the positive peak of the domain signature does not disappear, remaining as essentially a stacked signature such as 1090 nm in Fig. 6.3.

pect the positive peak of the domain wall signature visible in the backward signal to be more visible when submerging the crystal in water. Exemplary profiles are shown in Fig. 6.14 for an x-polarised fundamental beam at (a)1050 nm and (b)1110 nm, as well as (c)1050 nm for a z-polarised fundamental beam.

Fig. 6.14 (a) and (c) show that for both an x-polarised fundamental below the threshold wavelength and for a z-polarised beam, the addition of either the mirror or water environment does not seem to cause a noticeable change in the generated signal. The sole difference seems to be an increase or decrease of the positive peak of the domain wall signature compared to the surrounding area. Instead we shall focus on the profiles plotted in Fig. 6.14(b) for ax x-polarised fundamental at 1110 nm. For the profile recorded with a mirror behind the crystal, we observe that any sign of the positive peak has disappeared which would be explained by the massively increased forward-emitted signal being reflected towards the detector. This would support the idea that the increase in domain signal visible in Fig. 6.13 is indeed simply reflected forward-emitted SHG light. Unlike in the profile recorded with the added mirror, the positive peaks we currently attribute to CSHG emission appear to be slightly more visible in an aqueous environment compared to the surrounding domain. However, the apparent change is not as visible as we would have expected, which makes it difficult to confidently associate the parts of the signal to our assumed generation mechanism. The differentiation of forward-emitted and subsequently reflected signal from directly backward-emitted will require further investigative effort outside of the scope of this work and can form part of a future experiment proposal.

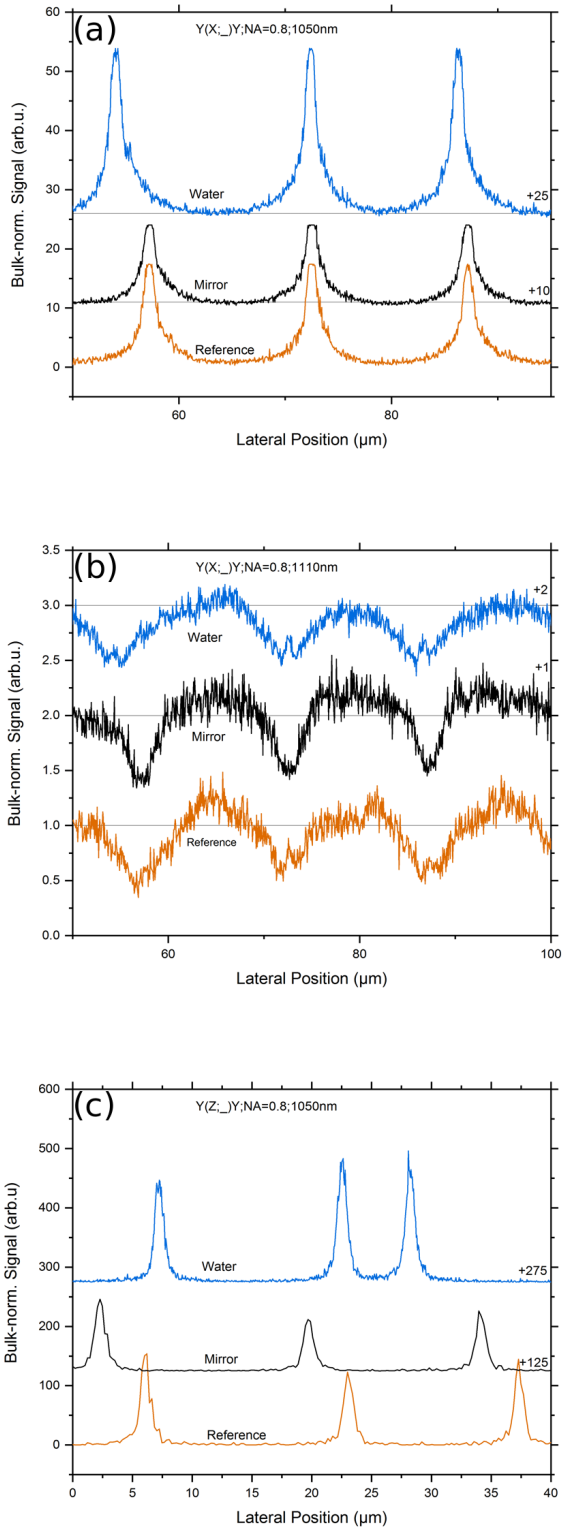

Figure 6.14: Profiles extracted from 50 μm within a y-cut lithium niobate crystal in a reference set-up as well as using both a mirror and aqueous environment. The polarisation of the fundamental beam is either x-polarised ((a) and (b)) or z-polarised (c). In both sets of profiles recorded with a 1050 nm fundamental ((a) and (c)), we see no change caused by the altered experimental conditions. As expected, the addition of a mirror to the rear of the sample causes the disappearance of the positive peak in the middle profile of (b) due to the increased amount of forward-emitted signal detected. When subjecting the crystal to the water environment, we can observe that the positive peaks become slightly more identifiable.

7 Contrast analysis and impact of CSHG

The previous chapters have presented the results from a number of SHG experiments performed on primarily y-cut congruent lithium niobate. Through varying a number of experimental parameters, it was possible to either isolate certain behaviours or induce phenomena which to our knowledge have been sparsely investigated in literature. However, while the result of a change in experimental parameter has been shown, we have yet to attempt to quantify a relationship between the varied parameter and the resulting images. The following chapter represents a first attempt at such a relationship.

7.1 Contrast Analysis

The first step in establishing a relation capable of being evaluated lies in defining a system property with which to express the changes caused, an order parameter, so to speak.
A suitable candidate can be found in the contrast of the domain walls to the bulk material, that is the ratio of the signal generated at a given domain wall compared to the average domain signal, calculated as

$$C = \frac{I_{DW} - I_D}{I_D} = \frac{I_{DW}}{I_D} - 1, \tag{7.1}$$

with I_{DW} the signal level at the domain wall and I_D the mean domain signal. We can quickly identify a dark line on a bright background as a negative contrast value, while any bright line on a dark background would present as a positive value.
In order to obtain contrast values for each parameter configuration consisting of the set [geometry, wavelength and depth with respect to the surface], the values were calculated for a number of peaks per profile, which were then averaged.
As presented in the previous chapter, some configurations resulted in an overexposure of the detector, which lead to a plateau region with the peak tip cut off. For profiles in which this was visible, the overexposed peaks were both compared to other peaks of the profile, as well as an overlay of an unexposed profile with as close a parameter configuration as possible. This

overlaid profile is most often the profile taken for the same geometry and wavelength, yet for a slightly shallower depth within the crystal. As stated at the end of Chapter 4, in the majority of cases, the domain wall signature peak was still visible up to roughly 80% of the peak height, such that the fitted amplitude was roughly 20% lower than the expected value. This difference was used to slightly correct the contrast values, while introducing a relative error of up to 25%, which will be included in the affected plots.
From the results of Chapter 6, we already know to expect a change in contrast for the Y(X;_)Y geometry of cLN above a wavelength of 1090 nm. The contrast plots for Y(X;_)Y will be presented at a later point. In order to have a basis for comparison, the contrast for a geometry unaffected by wavelength will be presented, which once again will be the Y(Z;_)Y geometry, so a z-polarised fundamental beam propagating along the y-axis. The following plots will show both the contrast for varying depths within the crystal for chosen wavelengths, as well as the contrast dependent on wavelength for a reference depth of 50 μm.

As expected, Fig. 7.1(a) shows that the contrast for the Y(Z;_)Y geometry remains positive, both within the crystal as well as close to the surface. If we mentally extend the trend towards distances further away from the surface, we can feel reasonably confident in assuming that the contrast will go to 0, as no signal at all will be measured.
Entrance into the crystal shows a noticeable increase across all three wavelengths, which, however, flattens out into what seems to be a plateau after a sufficient depth into the sample. The values each plateau approximately sits at are presented in table 7.1.
It is interesting to note that at the surface as well as shortly below it, there seems to be

1050 nm	$C = 51.6$
1080 nm	$C = 47$
1110 nm	$C = 28.5$

Table 7.1: Calculated contrast values at which the curves seem to plateau at for each wavelength when progressing into the crystal depth.

no obvious difference in the measured contrast up until a depth of approximately 20 μm. In general, we see a decrease in contrast with wavelength, as is visible from Fig. 7.1(b), where the contrast at a reference depth of 50 μm is plotted for wavelengths from 1050 nm to 1110 nm. It is important to note that the sample was exposed to 1% of the maximum laser output for each wavelength and that said maximum power decreased for increasing wavelengths. The contrast values were therefore corrected based on the assumption that the generated signal should scale quadratically with the input laser power. The incident power at 1050 nm was taken as the reference value and the other wavelengths were scaled with the factor $F_{PCo} = (P(1050nm)/P(\lambda))^2$. For comparison, both the uncorrected and corrected values are shown in Fig. 7.1(b).
Despite the correction, the trend is unaffected. A possible explanation could possibly be found

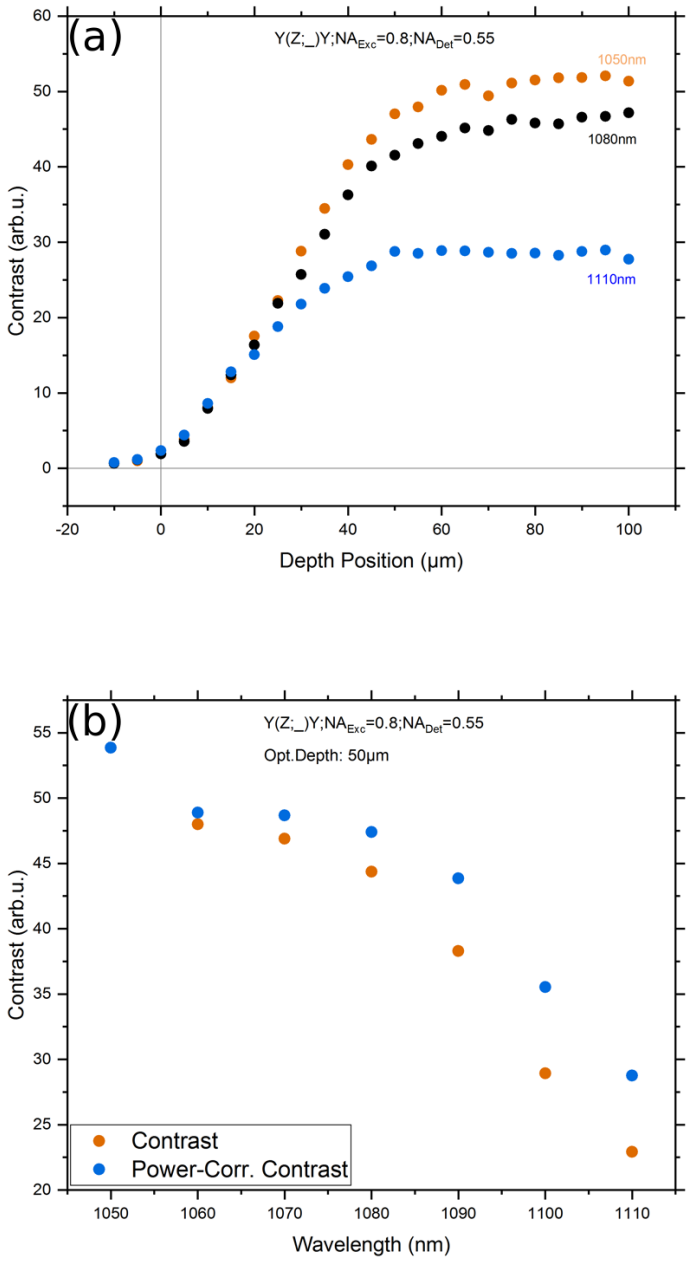

Figure 7.1: Contrast Plots for a y-cut congruent lithium niobate sample for (a) varying depths for three chosen wavelengths, (b) different wavelengths in a reference depth of 50 μm. Plot (a) is intended to compare the trends for each wavelength, as well as give an initial comparison of the magnitude for each wavelength. As the laser power would fluctuate depending on wavelength, the calculated contrast, which predominantly depends on the domain wall signature and therefore the fundamental excitation, the contrast values here were corrected for the difference in laser power.

in an absolute comparison of the respective signals with the addition of a power correction to the higher wavelength. As the detector settings remained untouched, it should have no

further effect on the signal. The domain contributions used to normalise the signals are in a similar order of magnitude at roughly 709 counts for 1050 nm and 360 counts for 1110 nm. This however would suggest that the contrast would be higher for higher wavelengths. A comparison of the signature peak amplitudes also shows a decrease in the detected signal for higher wavelengths even after the correction to account for the power difference. With the absolute amplitudes of the three investigated peaks listed in table 7.2, along with the ratio $Counts(1050\,\text{nm})/Counts(1110\,\text{nm})$. As the detector sensitivity as stated by Zeiss is close to

Peak Nr.	1050 nm	1110 nm	Ratio
1	33514	9744.29	3.44
2	31369	9445.85	3.32
3	37426	10772.51	3.46

Table 7.2: Absolute counts for selected peaks at 1050 nm and the power-corrected counts for 1110 nm along with the corresponding ratios.

unchanged over the wavelength range of the collected signal (525 nm to 555 nm), the difference in contrast could therefore lie in a decreased SHG for higher wavelengths. The same plots as shown in Fig. 7.1 were compiled for the Y(X;_)Y geometry and presented in Fig. 7.2.

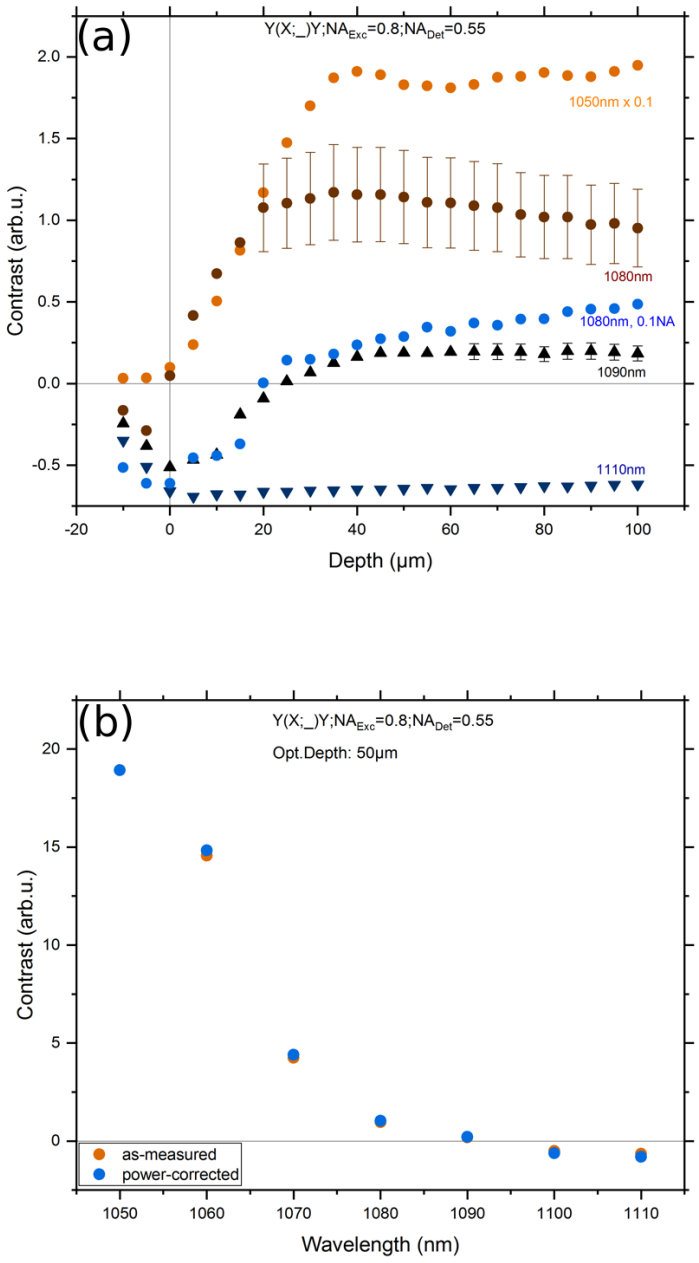

Figure 7.2: Contrast Plots for a y-cut congruent lithium niobate sample in the Y(X;_)Y geometry for (a) varying depths for five chosen wavelengths, (b) different wavelengths in a reference depth of 50 μm. Plot (a) is intended to compare the trends for each wavelength, as well as give an initial comparison of the magnitude for each wavelength. It is important to note that the contrast plot for 1050 nm is scaled down to a tenth of its amplitude to be able to include it in the same plot. The contrast for the profile recorded at 1080 nm using a collection NA of 0.1 was included due to its similarity to the profile for 1090 nm. As the laser power would fluctuate depending on wavelength,the contrast values here were corrected for the difference in laser power using the laser power at 1050 nm as a reference. Due to overexposure when scanning directly over the domain wall signatures, the neighbouring peaks were used to assess that roughly the top 15% of the overexposed peaks were missing and the calculated fit amplitudes were corrected according to the short study presented in section 4.3.2. The relative error calculated therein was included in the affected data points.

From the profiles shown in the previous chapter, we would expect our fringe cases of 1050 nm and 1110 nm to show a positive and negative contrast, respectively, disregarding the depth at which it was measured. As we can see in Fig. 7.2(a), this expectation holds, with the contrast values for 1050 nm having been scaled down by a factor of 10 to be plotted in the same range. For the positive contrast, we see a similar behaviour to the Y(Z;_)Y geometry, in that an initial sharp increase leads into a plateau towards lower depths with the contrast only varying little. Likewise, we can see the contrast goes to 0 for larger depths above the surface of the crystal, as the system will eventually become unable to detect any signal, this holds for all measured wavelengths.

Proceeding to higher wavelengths above the Switch point we see that the same plateau-ing behaviour repeats, although at different contrast values for each. The important common factor is a negative contrast of the domain walls to the surrounding domains, as this is evident for all presented wavelengths. Starting from the surface, however, the profile recorded at 1080 nm follows the same trend as for a process obeying normal dispersion. Due to the overexposure at the domain walls, the peak values had to be estimated by fitting the peaks as presented in section 4.3.2 and including the determined necessary correction and relative error of 25%. The signatures were estimated to be missing roughly the top 20% of the peak, leading to an amplitude that would be 15% lower than the actual value.

We included the profile recorded at 1080 nm using the smaller collection NA of 0.1. Based on the results of the previous chapter, specifically Figs. 6.5 and 6.6, we would have expected the configuration to show a negative contrast for higher depths into the crystal. This is indeed the case, as a positive contrast ist not visible until a depth of 20 μm. As the lower NA will always gather less light, it is not much of a surprise, that the contrast values are not as high as compared to the 0.55 NA measurement. However, the important difference is the fact that the change in sign of the contrast occurs later, which could indicate that the conical emission from CSHG is to blame for the positive contrast.

As with the similarities in their profile at a depth of 50 μm, the contrast curve for 1090 nm follows almost the exact same path as that of the 0.1NA 1080 nm profile, with the change in sign occuring roughly at 25 μm.

The last contrast plot to inspect is that for 1110 nm. Recalling Fig. 6.1, we expect to see a negative contrast value throughout the crystal, which is indeed the case. Starting from the surface, the contrast seems to stabilise immediately at approximately -0.64. [1] Comparison with Fig. 7.2(b) would show that the contrast value at a depth of 50 μm for 1000 nm is at a similar value of -0.51. This could indicate that the contrast for 1110 nm is close to or already at the minimum level it can achieve due to the shallower slope between data points as compared to lower wavelengths.

Likewise, Figs. 7.1(b) and 7.2(b) both give the impression, that the change in contrast value

[1] Simulations by Rüsing et al. have predicted a similar value of -0.4 in general for the expected negative contrast in a Y(X;_)Y based on phase interference.[17]

for lower wavelengths lessens for shorter wavelengths. It could therefore be possible that there is a maximum positive contrast for cLN, although it would have to be assumed at a lower wavelength than the range investigated here.

7.1.1 Attempting to quantify the strength of CSHG

In addition to analysing the behaviour of the domain wall contrast depending on the fundamental wavelength, it can also help us gain a rough estimate for the "strength" of CSHG when compared to f.e. phase superposition at the crystal surface. The apertures introduced in section 5.3 essentially function as filters for SHG light generated with more or less assistance of a quasi-momentum or k-vector of the domain wall. They can then be used to selectively block either the signal behaving according to phase superposition (low k-vector assistance, dark-field aperture) or the CSHG signal (large k-vector assistance/quasi-momentum, bright-field aperture) generated at the front surface of the crystal. Fig. 7.3 shows the cross-sections of a lithium niobate sample using a (a) bright-field and (b) dark-field aperture for a 900 nm fundamental beam.

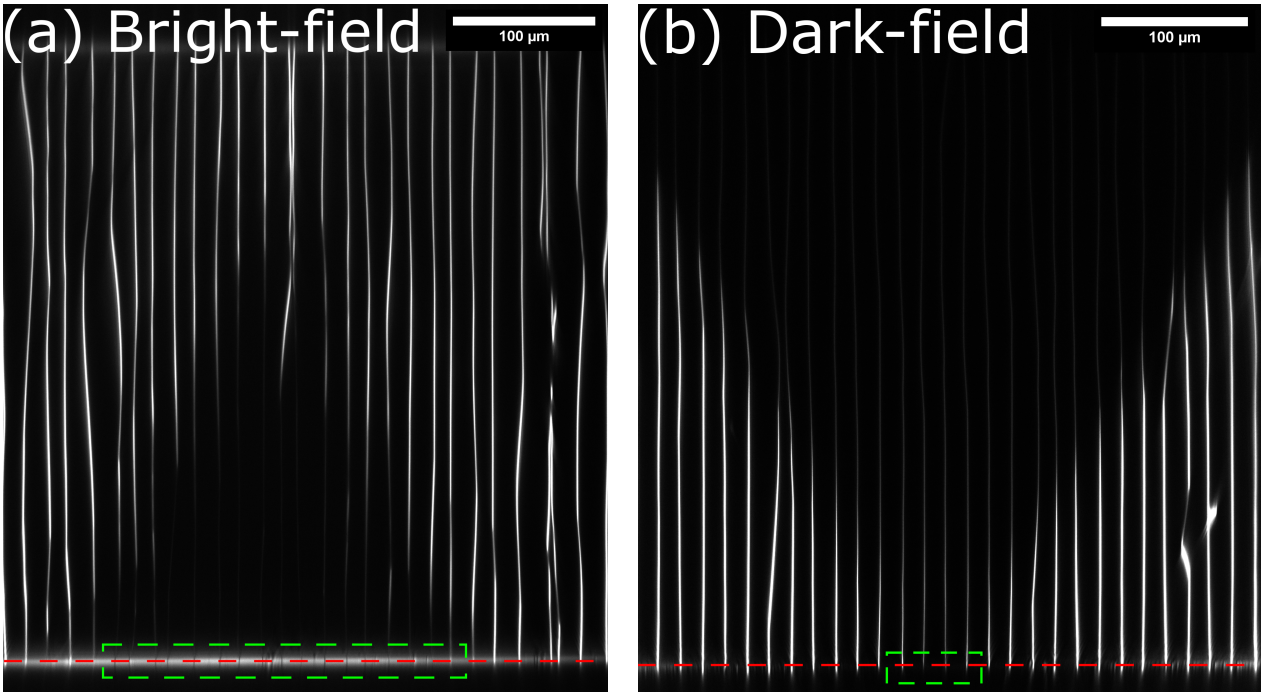

Figure 7.3: XY cross-sections of a lithium niobate crystal illuminated with an x-polarised fundamental beam at 900 nm using: (a) a bright-field aperture; (b) a dark-field aperture. Focusing on the surface within the blocked region, we observe that each image displays a distinctly different signal contribution which are simultaneously observed in experiments without an aperture. Towards the edges of both images, we begin to see more of the other signal contribution as it is less effectively blocked by the respective aperture. The crystal surface is marked with a red dashed line, and the region of interest is marked with the green-dashed box.

As both images as a whole have previously been explained in section 5.3, we will focus here on the surface as our region of interest. Depending on the type of aperture, we see that one of the two contributions to the signal is absent due to being blocked by the aperture body in the centre of the image. This is visible as the bright surface signal but dark domain wall lines in (a) and as the bright domain walls with no apparent surface level in (b). However, both images also show signs of the respectively other signal towards the edge as generated light is less inhibited by the aperture's blocking. In order to calculate the contrast for each signal type, smaller regions of the surface profile were evaluated for their average contrast values as indicated by the red selection boxes in Fig. 7.4 for: (a) the bright-field profile and (b) the dark-field profile.

Due to the strong variance in surface signal level within the bright-field profile, the examined region was split into two sub-regions and normalised individually. The contrast is then calculated by extracting the average peak level of the negative peaks for the bright-field aperture and the positive peaks in the region of interest for the dark-field aperture and lowering the value by 1 as per the equation at the start of this chapter. In addition to the central, blocked, region of each profile, the contrast value was calculated for each edge of the surface profile along with that of a reference profile without any kind of aperture. The results are summarised in table 7.3.

Aperture type	Left edge	Blocked region	Right edge
Reference	–	3.17 ± 0.18	–
Bright-field	1.26 ± 0.39	-0.41 ± 0.06	2.67 ± 0.33
Dark-field	32.76 ± 6.10	28.5 ± 13.9	20.4 ± 2.6

Table 7.3: Contrast values in [arb.u.] calculated for the blocked regions presented in Fig. 7.5 as well as both edges of the respective surface profiles shown in Fig. 7.4. A reference value was calculated from a profile without any kind of aperture to gain a rough comparison with other measurements performed in the present work.It is important to note that the contrast value of the right edge of the image is noticeably lower likely due to the increased surface signal visible in the relevant region of Fig. 7.4(b).

As the domain walls were visible as bright lines even on the surface in images without an aperture, it is of little surprise that we observe a positive contrast for the reference profile. The contrast value of -0.41 observed for the bright-field aperture removing the CSHG contributions agrees well with predictions made by Rüsing et al. [17]. The predictions were made based on phase-superposition arguments, supporting the previous findings that a bright-field aperture of appropriate size will effectively eliminate the detection of CSHG light. Outside of the central region without CSHG contributions, the contrast is again positive indicating that even gathering only half of the generated CSHG signal is enough to override the contrast stemming from phase interference.

The contrast values for the dark-field aperture are considerably higher than for the bright-field

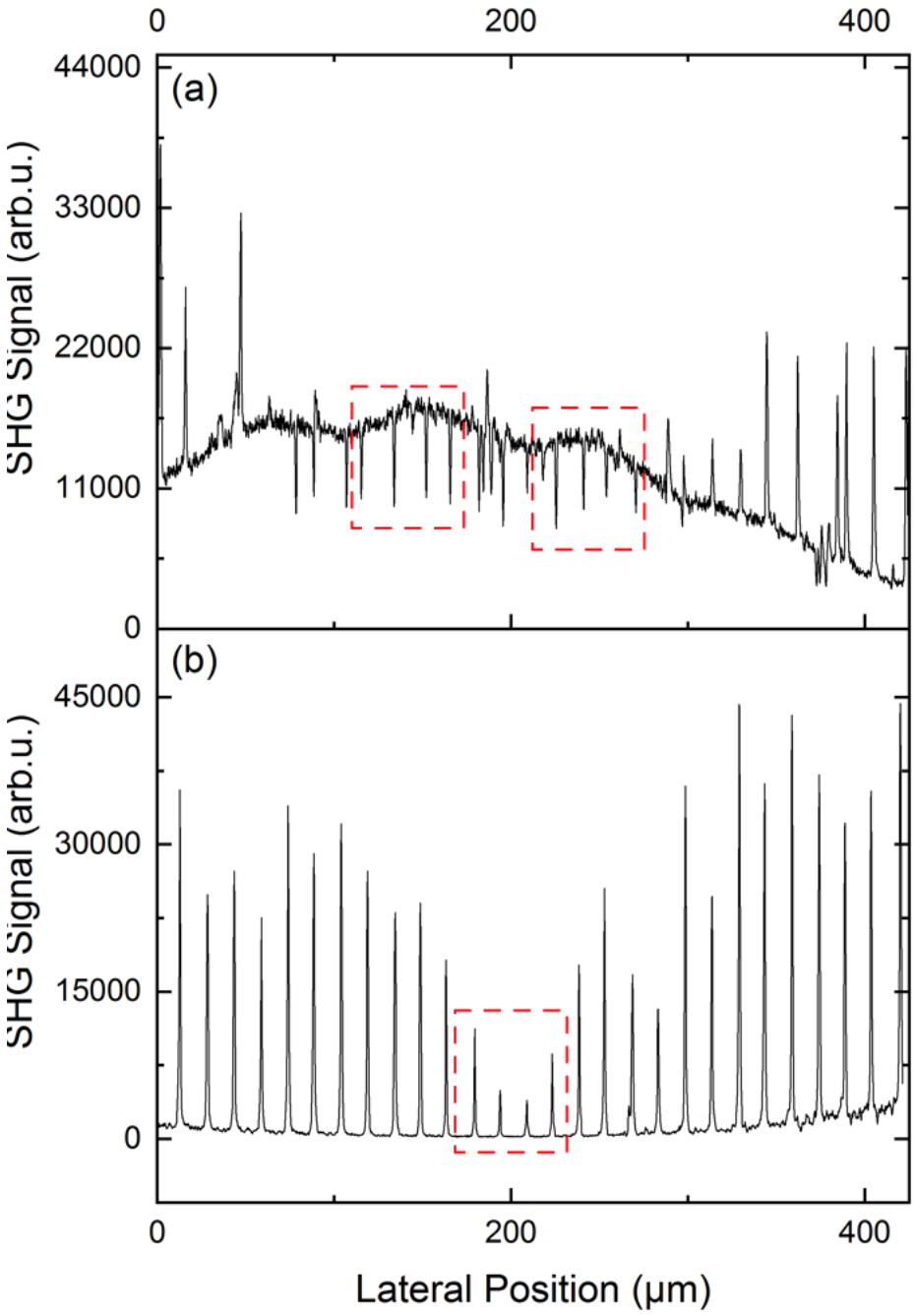

Figure 7.4: Line profiles across the surface for: (a) a bright-field aperture; (b) a dark-field aperture, recorded with an x-polarised fundamental beam at 900 nm in a y-cut lithium niobate crystal. Some regions from which one of the two signal contributions are blocked are outlined in red selection boxes. Due to the uneven surface signal level in the bright-field image, the examined range of the profile was split into sub-regions for normalisation.

aperture or in fact even the reference surface profile. This was to be expected, as the reason we used the dark-field aperture was to eliminate as much of the SHG without domain wall

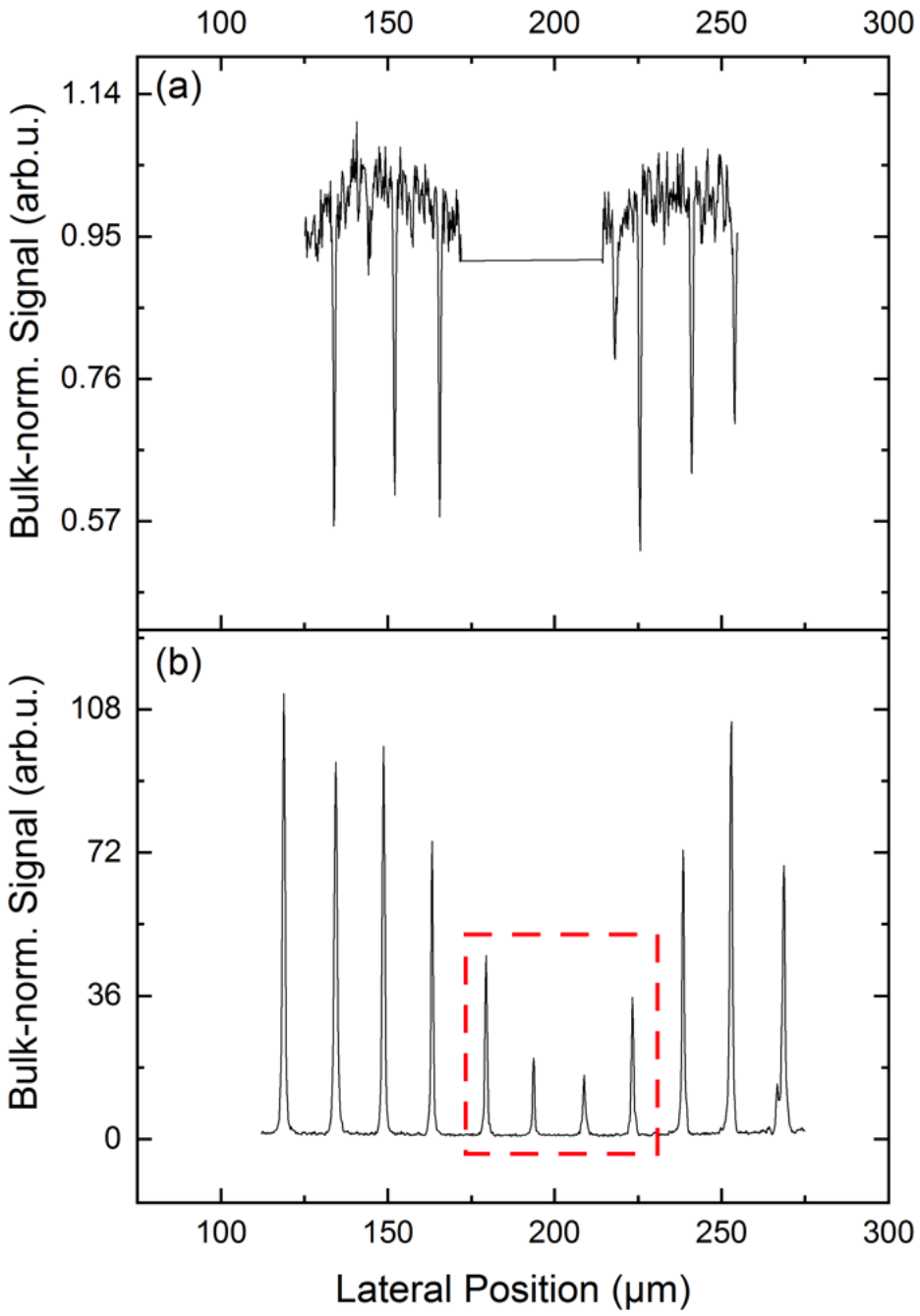

Figure 7.5: Bulk-normalised profiles of the regions within the red-dashed selection boxes in Fig. 7.4 for the bright-field aperture in (a) and the dark-field aperture in (b). The fully blocked region in the dark-field profile is once again indicated by the red-dashed selection box in (b).

k-vector contributions as possible, thereby removing the basis on which we performed our normalisation. However, even so we can see that the signal generated by CSHG will far exceed the other contributions, indicating that the k-vectors supplied by the domain wall strongly

improve the efficiency of the SHG process along the walls themselves.
Due to the relatively crude nature of the utilised apertures, a more accurate calculation of the contrast is definitely possible, f.e. by using an aperture consisting of a thin layer of metal evaporated onto the crystal surface. This would offer a better defined edge to the blocking behaviour as well as a known aperture width with which one could make more accurate predictions of the measured behaviour. However even with our current foil apertures, it is possible to visualize and measure the difference in the imaging processes using phase-interfering or Cherenkov-emitted second harmonic light. Doing so it is possible to estimate the comparative strength by comparing the central contrast of the bright-field image to the reference value which would lead us to believe that the CSHG contributions are roughly a factor 8 stronger than the phase interference.

8 Conclusion and outlook

The goal of the present master thesis was to investigate the possibility of isolating the signal generated at domain walls via CSHG while performing SHGM on a periodically-poled LNO crystal. The aim was then to undertake first steps towards an understanding of the behaviour of CSHG and how it can be influenced as part of the SHGM process. To this end, two methods of differentiation were developed in chapter 3 and subsequently experimentally tested in subsequent chapters. To the extent of our knowledge, we may have also been the first to both detect and investigate CSHG from a y-cut LNO crystal, as a majority of published works focus on z-cut crystals.

The first method consisted of using a geometric construction outside the investigated sample in order to selectively block the Cherenkov-emitted second harmonic. The results were presented in chapter 5 in the form of two different geometric blocking constructions to isolate certain parts of the signal. Initially, the collection numerical aperture was lowered to decrease the collected angular spread which led to the obliquely emitted CSHG light being unable to be detected. Furthermore, it was shown that the angle at which the sample emits CSHG signal will vary with a change in wavelength, as evidenced by the change in threshold NA below which the CSHG signal contribution at the domain walls disappeard which agreed with prior predictions.

A second approach was also tested by leaving the collection numerical aperture unchanged and applying an improvised aperture to the rear surface of the crystal. We have shown that depending on the kind of aperture applied, we can selectively block different contributions to the total detected signal that are emitted either collinearly or at an oblique angle to the optical axis based on the geometric relation between the aperture size and the position of the focus. Based on the images recorded with a dark-field aperture, an attempt was made to calculate the actual Cherenkov angle for a number of wavelengths. It was found that the extracted emission angle showed the expected behaviour with an increase in fundamental wavelength, however, the actual values lay between the two curves describing the two possible CSHG process branches. A possible explanation could be found in a polarisation preference of the domain wall itself, which would require a better-constructed aperture-based experiment along with polarimetry to investigate. Both continuations of the presented experiments currently exceeded the scope of this work and are a goal for future studies.

In addition to the differentiation based on geometrically blocking the generated CSHG sig-

nal, a further method was investigated by varying the fundamental wavelength and inducing a dispersion switch from normal to anormal behaviour. It was shown that CSHG is no longer detectable above a threshold wavelength of approximately 1080 nm and that instead the domain regions of the crystal show an increased signal generation. The results have been presented in chapter 6, along with images showing that the observed behaviour is limited to the Y(X;_)Y measurement geometry, as this is the only measurement set-up capable of experiencing the anormal dispersion. Additionally, we have shown that the dispersion flip is not only observable in congruent lithium-niobate but also in MgO-doped crystals for a different threshold wavelength as expected from the measured dispersion relations of the materials. A number of scans were presented in order to show that the observed dispersion flip is only visible in the forward direction by measuring the backward signal. However, these results were not as unambiguous as expected and the topic will require further investigations to ascertain that CSHG is an intrinsic part of the backward-emitted signal.
Finally, in chapter 7 we attempted an initial quantitative analysis in order to evaluate the trend in the domain wall contrast with a variation of the fundamental wavelength as well as evaluate the behaviour of the domain wall at increasing depths within the crystal. It was found that while the contrast values differ in value, all investigated geometries seemed to fluctuate before stabilizing at a final value at a depth of 20 μm into the crystal. This was observed both for geometries capable of exhibiting CSHG as well as those were unable to emit oblique radiation. Additionally, based on the comparison of the surface signal of a reference image with the surface signal using a bright-field aperture which blocked the CSHG light, it was found that the signal strength of CSHG seemed to be roughly 8 times larger than the signal generated without the influence of Cherenkov-type phase-matching.
The present thesis has touched on a number of approaches to isolating signal contributions for Second Harmonic Generation Microscopy, giving an initial insight into the properties of CSHG as well as prospects for further work. In the following, a short list of possible experimental proposals shall be given:

- **Aperture experiments with metal electrodes** - The apertures used to filter out signals generated either with or without domain wall k-vector assistance proved an effective tool despite their relatively crude nature. In the future, we intend to repeat the measurements with well-defined and microscopically thin apertures created by depositing chromium or gold onto the sample using a lithographic mask. This should allow for a more accurate evaluation of both bright-field and dark-field behaviour. Additionally, a more detailed understanding of the use of such apertures can be equally used to filter measurements using other methods such as Coherent Anti-Stokes Raman Spectroscopy (CARS) or Third Harmonic Generation (THG).

- **Polarised detection** - As mentioned previously, the utilised light scanning microscope was limited to unpolarised detection paths, which results in the detected signal being

a possible superposition of signals generated with two different polarisation directions. Due to the current lack of published work on CSHG on y-cut LN, our predictions were based on findings for z-cut crystals. As shown in chapter 6, our actual results indicate that there may be a possible preferential polarisation at the domain wall in y-cut crystals which we would like to study. Efforts have been initiated to improve the measurement set-up in acquiring a polarised detection method.

- **Application to other materials** - In the present work, we utilised congruent lithium-niobate as the test bed for our measurements. However, the assumptions used to derive our differentiation methods were based on general properties of non-linear interactions and observations made using SHGM on a number of materials. It would be interesting to confirm the existence of the same observed behaviour in other ferroelectric crystals which fulfil the requirements outlined in chapter 3.

SHGM remains a potent and valuable tool in the investigation of lower-dimensional systems, with a current influx of work made to more fully understand the method itself when applied to ferroelectric domain walls. It is our hope that the present master thesis can serve as a motivation to further the investigations into understanding the behaviour of domain walls during SHGM in order to better utilise the method to analyse novel systems and devices.

Bibliography

[1]Y. Liu et al., "van der Waals Integrated Devices Based on Nanomembranes of 3D Materials", Nano Lett. **20**, 1410 (2020).

[2]J. Shim et al., "Light-Triggered Ternary Device and Inverter Based on Heterojunction of van der Waals Materials", ACS Nano **11**, 6319 (2017).

[3]S.-J. Liang et al., "Van der Waals Heterostructures for High-Performance Device Applications: Challenges and Opportunities", Adv. Mat. **32**, 1903800 (2020).

[4]T. Kämpfe et al., "Real-time three-dimensional profiling of ferroelectric domain walls", Appl. Phys. Lett. **107**, 152905 (2015).

[5]B. Kirbus et al., "Real-Time 3D Imaging of Nanoscale Ferroelectric Domain Wall Dynamics in Lithium Niobate Single Crystals under Electric Stimuli: Implications for Domain-Wall-Based Nanoelectronic Devices", ACS Appl. Nano Mater. **2**, 5787 (2019).

[6]T. Kämpfe et al., "Optical three-dimensional profiling of charged domain walls in ferroelectrics by Cherenkov second-harmonic generation", Phys. Rev. B **89**, 035314 (2014).

[7]L. Wehmeier, "Second Harmonic Generation For Real-Time Tracking Of Ferroelectric Domain Walls Under External Stimuli", Master thesis (Institut für Angewandte Physik, TU Dresden, 2016).

[8]S. Denev et al., "Probing ferroelectrics using optical second harmonic generation", J. Amer. Ceram. Soc. **94**, 2699 (2011).

[9]S. Cherifi-Hertel et al., "Non-Ising and chiral ferroelectric domain walls revealed by nonlinear optical microscopy", Nat. Comm. **8**, 15768 (2017).

[10]K. Brekhov et al., "Optical Diagnostics of WSe_2 Monolayers", Techn. Phys. Lett. **43**, 1112 (2017).

[11]H. Chen et al., "Enhanced second-harmonic generation from two-dimensional $MoSe_2$ by waveguide integration", in Conference on lasers and electro-optics (2017), FM2F.4.

[12]S. Cherifi-Hertel et al., "Shedding light on non-Ising polar domain walls: Insight from second harmonic generation microscopy and polarimetry analysis", J. Appl. Phys. **129**, 081101 (2021).

[13]K. Spychala et al., " Nonlinear focal mapping of ferroelectric domain walls in $LiNbO_3$: Analysis of the SHG microscopy contrast mechanism ", J. Appl. Phys. **128**, 234102 (2020).

[14]M. Flörsheimer et al., "Second-harmonic imaging of ferroelectric domains in $LiNbO_3$ with micron resolution in lateral and axial directions", Appl. Phys. B **67**, 593 (1998).

[15]A. Zembrod, H. Puell, and J. Giordmaine, "Surface radiation from non-linear optical polarisation", Opt. Quant. Electr. **1**, 396 (1969).

[16]Y. Uesu, S. Kurimura, and Y. Yamamoto, "Optical second harmonic images of 90° domain structure in $BaTiO_3$ and periodically inverted antiparallel domains in $LiTaO_3$", Appl. Phys. Lett. **66**, 2165 (1995).

[17]M. Ruesing, J. Zhao, and S. Mookherjea, "Second harmonic microscopy of poled x-cut thin film lithium niobate: Understanding the contrast mechanism", J. Appl.Phys. **126**, 777 (2019).

[18]P. Mackwitz et al., "Periodic domain inversion in x-cut single-crystal lithium niobate thin film", Appl. Phys. Lett. **108**, 152902 (2016).

[19]F. Brown, R. Parks, and A. Sleeper, "Nonlinear optical reflection from a metallic boundary", Phys. Rev. Lett. **14**, 1029 (1965).

[20]R. W. Terhune, P. D. Maker, and C. Savage, "Optical harmonic generation in calcite", Phys. Rev. Lett. **8**, 404 (1962).

[21]R. Boyd, *Nonlinear optics* (Academic press, 2020).

[22]J. Armstrong et al., "Interactions between Light Waves in a Nonlinear Dielectric", Phys. Rev. **127**, 1918 (1962).

[23]Z. Amber et al., "Quantifying the coherent interaction length of second-harmonic microscopy in lithium niobate confined nanostructures", J. Appl. Phys. **130**, 133102 (2021).

[24]K. Spychala et al., "Spatially resolved light field analysis of the second-harmonic signal of $\chi^{(2)}$-materials in the tight focusing regime", J. Appl. Phys. **127**, 023103 (2020).

[25]J. Kaneshiro et al., "Three-dimensional observations of polar domain structures using a confocal second-harmonic generation interference microscope", J. Appl. Phys. **104**, 054112 (2008).

[26]S. Bozhevolnyi et al., "Second-harmonic imaging of ferroelectric domain walls", Appl. Phys. Lett. **73**, 1814 (1998).

[27]S. Bozhevolnyi et al., "Far- and near-field second-harmonic imaging of ferroelectric domain walls", Opt. Comm. **152**, 221 (1998).

[28]Y. Zhang and S. Cherifi-Hertel, "Focusing characteristics of polarized second-harmonic emission at non-Ising polar domain walls", Opt. Mater. Express **11**, 3736 (2021).

[29]Y. Gu et al., "Flexoelectricity and ferroelectric domain wall structures: Phase-field modeling and DFT calculations", Phys. Rev. B **89**, 174111 (2014).

[30]S. Saltiel et al., "Multiorder nonlinear diffraction in frequency doubling processes", Opt. Lett. **34**, 848 (2009).

[31]J. Gonnissen et al., "Direct Observation of Ferroelectric Domain Walls in $LiNbO_3$: Wall-Meanders, Kinks, and Local Electric Charges", Adv. Funct. Mater. **26**, 7599 (2016).

[32]L. Eng and H.-J. Güntherodt, "Scanning force microscopy and near-field scanning optical microscopy of ferroelectric and ferroelastic domain walls", Ferroelectrics **236**, 35 (2000).

[33]V. Gopalan, V. Dierolf, and D. Scrymgeour, "Defect-domain wall interactions in trigonal ferroelectrics", Ann. Rev. Mater. Research **37**, 449 (2007).

[34]X. Deng and X. Chen, "Domain wall characterization in ferroelectrics by using localized nonlinearities", Opt. Express **18**, 15597 (2010).

[35]M. Rüsing et al., "Imaging of 180° ferroelectric domain walls in uniaxial ferroelectrics by confocal Raman spectroscopy: Unraveling the contrast mechanism", Phys. Rev. Materials **2**, 103801 (2018).

[36]K. Wong, *Properties of lithium niobate*, 28 (INSPEC, The Institution of Electrical Engineers, 2002).

[37]R. S. Weis and T. K. Gaylord, "Lithium niobate: Summary of physical properties and crystal structure", Appl. Phys. A **37**, 191 (1985).

[38]A. Grigas and S. Kaskel, "Synthesis of $LiNbO_3$ nanoparticles in a mesoporous matrix", Beilstein J. of Nanotechnol. **2**, 28 (2011).

[39]S. Hell et al., "Aberrations in confocal fluorescence microscopy induced by mismatches in refractive index", J. Microscopy **169**, 391 (1993).

[40]L. Novotny and B. Hecht, *Principles of nano-optics* (Cambridge university press, 2012).

[41]S. Reitzig et al., ""Seeing Is Believing"—In-Depth Analysis by Co-Imaging of Periodically-Poled X-Cut Lithium Niobate Thin Films", Crystals **11**, 288 (2021).

[42]X. Gu et al., "Backward second-harmonic generation in periodically poled lithium niobate", J.Opt. Soc. Amer. B **15**, 1561 (1998).

[43]Y. Sheng et al., "Cerenkov-type second-harmonic generation in two-dimensional nonlinear photonic structures", IEEE J. Quantum Electr. **45**, 1465 (2009).

[44]M. Ayoub, P. Roedig, and K. Koynov, "Čerenkov-Type Second-Harmonic Spectroscopy in Random Nonlinear Photonic Structures", Opt. Express **21**, 8220 (2013).

[45]A. Tunyagi, M. Ulex, and K. Betzler, "Noncollinear Optical Frequency Doubling in Strontium Barium Niobate", Phys. Rev. Lett. **90**, 243901 (2003).

[46]A. Kaminskii et al., "Second-harmonic generation with Cherenkov-type phase matching in a bulk nonlinear $LaBGeO_5$", Quantum Electr. **26**, 381 (1996).

[47]H. Yokota et al., "Domain wall generated polarity in ferroelastics: Results from resonance piezoelectric spectroscopy, piezoelectric force microscopy, and optical second harmonic generation measurements in $LaAlO_3$ with twin and tweed microstructures", Phys. Rev. B **102**, 104117 (2020).

[48]K. Kalinowski et al., "Enhanced čerenkov second-harmonic emission in nonlinear photonic structures", Opt. Lett. **37**, 1832 (2012).

[49]C. Godau et al., "Enhancing the Domain Wall Conductivity in Lithium Niobate Single Crystals", ACS Nano **11**, 4816 (2017).

[50]M. Maglione et al., "Intrinsic ionic screening of the ferroelectric polarization of KTP revealed by second-harmonic generation microscopy", Opt. Mater. Express **6**, 137 (2016).

[51]H. Ren et al., "Nonlinear Cherenkov radiation in an anomalous dispersive medium", Phys. Rev. Lett. **108**, 223901 (2012).

[52]D. Sandkuijl et al., "Numerical second- and third-harmonic generation microscopy", J. Opt. Soc. Amer. B **30**, 382 (2013).

[53]J. Butet, P. Brevet, and O. J. Martin, "Optical Second Harmonic Generation in Plasmonic Nanostructures: From Fundamental Principles to Advanced Applications", ACS Nano **9**, 10545 (2015).

[54]N. Mazumder et al., "Polarization resolved second harmonic microscopy", Methods **128**, 14090 (2017).

[55]B. Liu et al., "Probe of symmetry reduction at domain walls by nonlinear Cherenkov measurement", Opt. Express **24**, 29459 (2016).

[56]K. Kuznetsov et al., "Second harmonic generation in a strontium barium niobate crystal with a random domain structure", JETP Lett. **87**, 98 (2008).

[57]X. Huang et al., "Second-harmonic interference imaging of ferroelectric domains through a scanning microscope", J. Phys. D **50**, 485105 (2017).

[58]A. Fragemann, V. Pasiskevicius, and F. Laurell, "Second-order nonlinearities in the domain walls of periodically poled KTiOPO4", Appl. Phys. Lett. **85**, 375 (2004).

[59]M. Ayoub et al., "Simultaneous type I and type II Čerenkov-phase matched second-harmonic generation in disordered nonlinear photonic structures", Opt. Express **23**, 28369 (2015).

[60]Y. Uesu et al., "Three-dimensional observations of periodically poled domains in a $LiTaO_3$ quasiphase matching crystal by second harmonic generation tomography", Appl. Phys. Lett. **91**, 184902 (2007).

[61]J. Kaneshiro, Y. Uesu, and T. Fukui, "Visibility of inverted domain structures using the second harmonic generation microscope: Comparison of interference and non-interference cases", J. Opt. Soc. Amer. B **27**, 888 (2010).

Acknowledgements

Finally, I would like to acknowledge a number of people who made this work possible:

Prof. Dr. Eng, for the initial introduction to lower-dimensional systems and the fascinating topics involved therein. Similarly for his input, ideas and feedback while writing this thesis.
Prof. Dr. Imlau, for taking the role of secondary reviewer without hesitation.
Michael, for the numerous discussions, ideas and critiques during my time at the institute as well as for his patience in being a mentor.
The iSpex and SPM2 groups aswell as everyone in our office for making the time here as enjoyable as could be.
And not to forget, my family and friends who've put up with me all these years, thank you. Special thanks go out to both of you guys, Mum and Dad, for all the support you guys have given me, not just limited to this project but in setting me up for the future, helping me with struggles I've had and sharing the wee bits of wisdom.

I would also like to acknowledge the great support by the Light Microscopy Facility, a core facility of the CMCB Platform at Technische Universität Dresden, where I recorded the measurements used for this work.

Erklärung

Hiermit erkläre ich, dass ich diese Arbeit im Rahmen der Betreuung am Institut für Angewandte Physik ohne unzulässige Hilfe Dritter verfasst und alle Quellen als solche gekennzeichnet habe.

Peter Andrew Hegarty
Dresden,